Control and Data Analysis of Complex Networks

by

Lezhi Wang

A Dissertation Presented in Partial Fulfillment
of the Requirements for the Degree
Doctor of Philosophy

Approved October 2017 by the
Graduate Supervisory Committee:

Ying-Cheng Lai, Co-Chair
Xiao Wang, Co-Chair
Antonia Papandreou-Suppappola
David Brafman

ARIZONA STATE UNIVERSITY

December 2017

ABSTRACT

This dissertation treats a number of related problems in control and data analysis of complex networks.

First, in existing linear controllability frameworks, the ability to steer a network from any initiate state toward any desired state is measured by the minimum number of driver nodes. However, the associated optimal control energy can become unbearably large, preventing actual control from being realized. Here I develop a physical controllability framework and propose strategies to turn physically uncontrollable networks into physically controllable ones. I also discover that although full control can be guaranteed by the prevailing structural controllability theory, it is necessary to balance the number of driver nodes and control energy to achieve actual control, and my work provides a framework to address this issue.

Second, in spite of recent progresses in linear controllability, controlling nonlinear dynamical networks remains an outstanding problem. Here I develop an experimentally feasible control framework for nonlinear dynamical networks that exhibit multistability. The control objective is to apply parameter perturbation to drive the system from one attractor to another. I introduce the concept of attractor network and formulate a quantifiable framework: a network is more controllable if the attractor network is more strongly connected. I test the control framework using examples from various models and demonstrate the beneficial role of noise in facilitating control.

Third, I analyze large data sets from a diverse online social networking (OSN) systems and find that the growth dynamics of meme popularity exhibit characteristically different behaviors: linear, "S"-shape and exponential growths. Inspired by cell population growth model in microbial ecology, I construct a base growth model for meme popularity in OSNs. Then I incorporate human interest dynamics into the base model and propose a hybrid model which contains a small number of free parameters. The model successfully predicts the various distinct meme growth dynamics.

At last, I propose a nonlinear dynamics model to characterize the controlling of WNT signaling pathway in the differentiation of neural progenitor cells. The model is able to predict experiment results and shed light on the understanding of WNT regulation mechanisms.

To my parents

ACKNOWLEDGMENTS

I would like to express my most sincere gratitude towards my advisors, Dr. Ying-Cheng Lai and Dr. Xiao Wang for their guidance, mentoring, and continuous support over the past few years, which I couldn't have achieved so much without. I have been extremely lucky to have two supervisors who cared so much about my work, life and who respected my ideas and decisions. their deep insights and enthusiasm for science have inspired and helped me throughout my Ph.D. studies.

I want to take this opportunity to thank Dr. Zhihai Rong, Dr. Zigang Huang, Dr. Wenxu Wang and Dr. Hao Liu who have helped in so many aspects. Dr. Zhihai Rong, my undergraduate thesis advisor, gave me lots of suggestions in my first few years of graduate study. Dr. Zigang Huang and Dr. Wenxu Wang, the former research scientists of Chaos group, provided me inspiration and constructive critiques on many projects. Dr. Hao Liu, a sincere friend from math department, helped me a lot in my PhD research works.

I always value the excellent research atmosphere built by the Chaos group members, Dr. Yuzhong Chen, Dr. Riqi Su, Zhidan Zhao, Junjie Jiang, Dr. Hongya Xu, Dr. Lei Ying and Dr. Guanglei Wang, as well as Xiao Wang Lab members, Dr. Christophe Faucon, Dr. Fuqing Wu, Parithi Balachandran, Xingwen Chen, David Menn, Kylie Standage-Beier and Qi Zhang. The fruitful discussions and collaborations with them made me feel so supportive and encouraged all these years, and the friendship will take a lifetime to cherish.

I also want to thank Dr. David Brafman for his insightful knowledge and helpful discussions on many interesting research problems. I am grateful to Josh Cutts and Nick Brookhouser for their helpful suggestions and collaboration which made many great topics possible.

My special thanks to my committee member Dr. Antonia Papandreou-Suppappola for her time invested on me as well as invaluable comments and advices.

Finally, I would like to express the deepest thankfulness to my family for all their love and support, especially for my parents who raised me and supported me in all my pursuits. Thanks for the support to all my friends, my colleagues and my cat "Funding", who always sleep beside my laptop.

TABLE OF CONTENTS

APPENDIX

LIST OF TABLES

LIST OF FIGURES

Figure Page

Figure Page

Figure Page

1 . PHYSICAL CONTROLLABILITY OF COMPLEX NETWORKS

A challenging problem in network science is to control complex networks. In existing frameworks of structural or exact controllability, the ability to steer a complex network toward any desired state is measured by the minimum number of required driver nodes. However, if we implement actual control by imposing input signals on the minimum set of driver nodes, an unexpected phenomenon arises: due to computational or experimental error there is a great probability that convergence to the final state cannot be achieved. In fact, the associated control cost can become unbearably large, effectively preventing actual control from being realized physically. The difficulty is particularly severe when the network is deemed controllable with a small number of drivers. Here we develop a physical controllability framework based on the probability of achieving actual control. Using a recently identified fundamental chain structure underlying the control energy, we offer strategies to turn physically uncontrollable networks into physically controllable ones by imposing slightly augmented set of input signals on properly chosen nodes. Our findings indicate that, although full control can be theoretically guaranteed by the prevailing structural controllability theory, it is necessary to balance the number of driver nodes and control cost to achieve physical control.

1.1. Introduction

The past few years have witnessed great progress toward understanding the linear controllability of complex networks [1–28]. Given a linear and time-invariant dynamical system, the traditional approach to assessing its controllability is through the Kalman rank condition [29]. However, for a complex network, it is difficult to test, both mathematically and computationally, the Kalman rank condition directly to determine the optimal configuration for control input signals [1] due to the typically large network size and the complex spectrum of network topology. To overcome this difficulty, Liu et al. proposed in their pioneering work [4] to exploit Lin's classic theory of structural controllability [30]. In this framework, the fundamental issue is to determine the minimum number of controllers required to steer the whole networked system from an arbitrarily initial state to an arbitrarily final state in finite time. It was proved and demonstrated [4] that, for directed complex networks, their structural controllability can be established via the maximum matching algorithm [31–33]. In particular, based on Lin's theory, one can determine the maximally matched set of nodes, where each and every unmatched node requires an external control signal. An equivalent optimization procedure was developed for undirected networks to determine the minimum dominating set of nodes [6]. The structural controllability framework also served the base to address an array of issues such as edge dynamics [8], lower and upper bounds of energy required for control [7], control centrality [34], optimization [5], effects of the density of in/out degree nodes [14], and scaling of energy cost [27]. In addition, based on the classic Popov-Belevitch-Hautus (PBH) rank condition [35] from traditional control engineering, a variant of the structural-controllability theory, an exact controllability framework was developed [10] which is universally applicable to all kinds of complex networks: directed or undirected, weighted or unweighted. In terms of applications, the structural controllability framework has been used to characterize protein interaction networks to determine the key proteins responsible for certain biological functions [16].

In both structural and exact controllability frameworks, the focus is to determine the minimum number of control signals, denoted by N_D, for complex networks of various topologies. However, we have encountered an unexpected difficulty when using the minimal set given by either structural or exact controllability theory to carry out *actual* control of the network: convergence to the final state. In particular, given a network, once N_D is determined, we can determine the specific control signals to be applied at various unmatched nodes by using the standard linear systems theory [36].

The surprising phenomenon is that, quite often, actual control of the system cannot be achieved computationally in the sense that, in any finite time, the system cannot be driven from an arbitrarily initial state to an arbitrarily final state. We believe that this difficulty is fundamental, as we were not able to remove or even mitigate the problem of divergence despite extensive and systematic computational efforts in implementing various ways to optimize the numerical algorithm. This difficulty in realizing actual control persists for a large number of model and real world networks. While somewhat unsettling, the issue prompts us to hypothesize that the existing controllability frameworks are merely *mathematical*, as the implementation of actual control would often require infinite precision computations and, more seriously, an infinite amount of energy. To make the notion of controllability of complex networks meaningful, the issue of *physical* controllability must be addressed.

In this paper, we develop a physical controllability framework for complex networks to address whether actual control can be achieved in an experimentally or computationally feasible way. Given a complex network, we first use the structural controllability theory [4] to determine N_D and a set of unmatched nodes to which control signals are to be applied. Then, with a given pair of arbitrarily initial and final states as well as a finite control time, we calculate the optimal control signals [36] and evolve the whole networked system, which is essentially a linear dynamical system under external driving, to determine whether the system can be driven from the initial state to the final state in the given amount of time. During this process, the energy required for control can be calculated through the standard formula in linear systems theory [36, 37], which expresses the energy as the integral of the product of a number of matrices, including the inverse of the positive-definite, symmetric Gramian matrix. Freedom in choosing the initial and final states and independent network realizations render feasible a statistical analysis of the control process. We find that, typically, there are two cases, depending on whether the network can be physically controlled. For the physically controllable case, the whole system, starting from the chosen initial condition, can actually converge to the final state in the prespecified time *within a predefined precision*. In this case, the Gramian matrix is well-behaved, meaning that both its condition number and the energy are not unrealistically large. For the physically uncontrollable case, the system cannot reach the final state within the predefined precision in the given time. In such a case, the Gramian matrix is singular in the sense that its condition number can be arbitrarily large, so is the corresponding energy. Increasing the precision of the computation, e.g., by using special simulation packages with round-off error orders of magnitude smaller than that associated with the conventional double-precision computation, would convert a few uncontrollable cases into controllable ones, but vast majority of the uncontrollable cases remain unchanged.

The main result of this paper is a proposal of a general, probabilistic measure to characterize the physical controllability for complex networks of arbitrary topology. For physically uncontrollable networks, it is important to develop effective strategies to make them physically controllable. To accomplish this goal, we gain insights by calculating the control energy for a bidirectional 1D chain and obtaining an analytical relation between energy E and chain length L. We then apply the result to general networked systems based on the idea of longest control chain (LCC) [27]. Optimization strategies can be derived to decrease the control energy drastically. In fact, if the system is physically uncontrollable, a viable way to make it controllable is to increase the number of control signals beyond N_D. Our framework of physical controllability thus contains the following essential ingredients: (1) N_D, the minimum number of control signals determined by the existing mathematical controllability frameworks, (2) a measure of physical controllability, (3) control energy E determined by the Gramian matrix, and (4) augmentation of N_D for physically uncontrollable networks.

The existing mathematical controllability theories [4, 10] thus provide a base for our physical controllability framework. The quantity N_D, on which the mathematical controllability theories focus, can effectively be regarded as the *lower bound* of the actual number of control signals required. To realize physical control, depending on the specific system and control settings, either N_D control signals suffice or substantially more signals are needed.

1.2. Results

1.2.1. Definition of Physical Controllability.

We consider the standard setting of a linear dynamical system subject to control input [1,4,10]:

$$\dot{\mathbf{x}} = A \cdot \mathbf{x} + B \cdot \mathbf{u}, \tag{1.1}$$

where $\mathbf{x} = [x_1(t), \ldots, x_N(t)]^T$ is a vector of dynamical variables of the entire network, $\mathbf{u} = [u_1(t), \ldots, u_M(t)]^T$ is a vector defining the set of control input signals, $A = \{a_{ij}\}_{N \times N}$ is the adjacency matrix with N being the number of nodes in the network, and $B = \{b_{ik}\}_{N \times N_D}$ is control input matrix specifying the set of N_D “driver” nodes [4], each receiving a control signal that corresponds to one component of the control vector $\mathbf{u}$. From the linear systems theory, optimal control of a linear dynamical network in the sense of minimized energy cost can be achieved when the input control signals $\mathbf{u}_t$ are chosen as [36, 37]: $\mathbf{u}_t = B^T \cdot e^{A^T(t_{\mathrm{f}}-t)} \cdot W^{-1} \cdot (\mathbf{x}_{t_{\mathrm{f}}} - e^{At_{\mathrm{f}}} \cdot \mathbf{x}_0)$, where

$$W \equiv \int_{t_0}^{t_{\mathrm{f}}} e^{A\tau} \cdot B \cdot B^T \cdot e^{A^T\tau} d\tau \tag{1.2}$$

is the Gramian matrix, a positive-definite and symmetric matrix [36], which serves as the base to determine quantitatively if a system is actually controllable. In particular, the system is controllable only when W is nonsingular (invertible) for given control precision [36, 37]. With the control input signal $\mathbf{u}$, the energy cost is [36]

$$E(t_{\mathrm{f}}) = \int_{0}^{t_{\mathrm{f}}} \mathbf{u}_t^T \cdot \mathbf{u}_t dt, \tag{1.3}$$

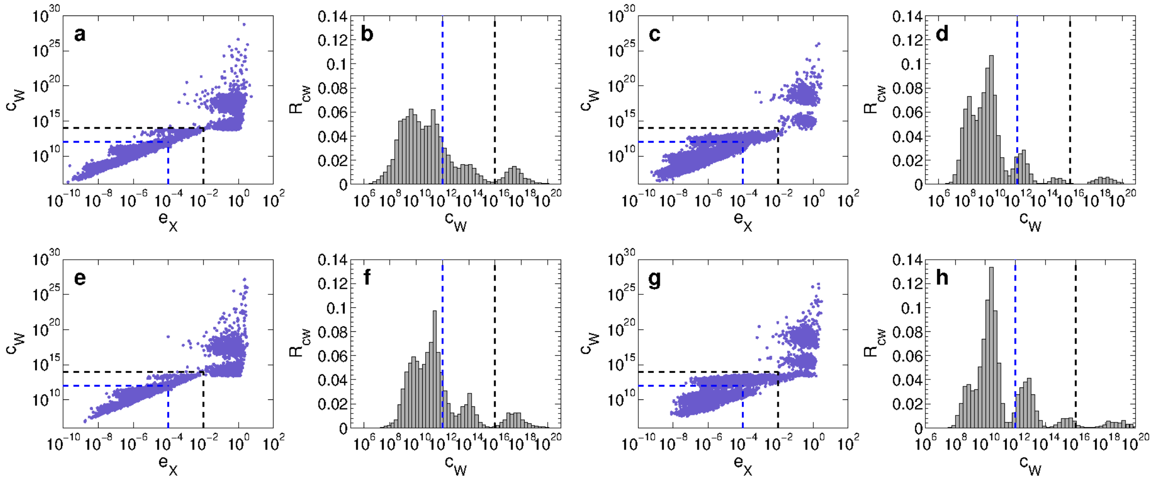

Fig. 1. Condition number C_W versus control precision e_X for random and scale-free networks. Network size is $N = 100$ for (**a**)-(**d**) and 200 for (**e**-**h**), average degree is $\langle k \rangle = 6$ for ER random networks [(**a**),(**b**),(**e**), and (**f**)] and 8 for BA scale-free networks [(**c**), (**d**), (**g**), and (**h**)]. Directional link probability between any pair of nodes is $P_b = 0.1$. Panels (**a**),(**c**),(**e**), and (**g**) show the scaling relation between the condition number C_W and the control precision e_X. Panels (**b**), (**d**), (**f**), and (**h**) show the fraction R_{CW} of the networks with a certain C_W number. The scaling relation holds within some C_W-e_X region with boundaries specified as the black dashed lines. The e_X values are not physically meaningful outside the boundaries that are defined according to the precision limit of computation. The thresholds of C_W and e_X used in the computations are 10^{12} and 10^{-4}, respectively, which are indicated as the blue dashed lines. The threshold values are chosen to lie within the physical boundaries so that the calculations for all C_W values are meaningful.

where control is initiated at $t = 0$ and ended at $t = t_{\rm f}$.

To present concrete evidence for the existence of physically uncontrollable networks, we use the Erdos-Renyi (ER) type of directed random networks [38] and the Barabási-Albert (BA) type of directed scale-free networks [39] with a single parameter $P_{\rm b}$. The meaning of $P_{\rm b}$ is the following. Given a pair of linked nodes, i and j, the probability that the link points from the smaller-degree node to the larger-degree one is $P_{\rm b}$, and the probability in the opposite direction is $1 - P_{\rm b}$. The link direction is chosen randomly if i and j have the same degree. To determine the set of driver nodes, we use the maximum-matching algorithm [30], which gives the control matrix B. For each combination of A and B, we first randomly choose the initial and final states. We then calculate the corresponding Gramian matrix W, its condition number, the input signal $\mathbf{u}_t$, the actual final states $\mathbf{x}^{\star}_{t_{\rm f}}$, and finally the control energy $E(t_{\rm f})$. Repeating this process for each and every independent network realization in the ensemble enables an extensive statistical analysis of the control process.

Mathematically, if the Gramian matrix W is singular, the energy diverges. Through extensive and systematic numerical computations, we find that, even when W is non-singular in the mathematical sense, for typical complex networks its condition number can be enormously large, making it effectively singular as any physical measurement or actual computation must be associated with a finite precision. Say in an experiment the precision of measurement is ε. In a computational implementation of control, ε is effectively the computer round-off error. Consider the solution vector $\mathbf{X}$ of the linear equation: $W \cdot \mathbf{X} = \mathbf{Y}$, where $\mathbf{Y}$ is a known vector. Let C_W be the condition number of W. The accuracy of the numerical solution of $\mathbf{X}$, denoted by $e_X = 10^{-k}$ (k is a positive integer), is bounded by the product between C_W and ε [40]. We see that, if C_W is larger than $10^{-k}/\varepsilon \equiv \bar{C}_W$, it is not possible to bring the system to within 10^{-k} of the final state at finite control cost, so physically control cannot be achieved in finite time.

For a large number of networks drawn from an ensemble of networks with a pre-defined topology, the condition numbers of their Gramian matrices are often orders of magnitude larger than $\bar{C}_W$. Figure 1 shows the correlation between the condition number C_W and the control error e_X. We observe that, within a certain range of C_W, an approximate scaling relation exists between C_W and e_X, as shown in panels (a, c, e, g). However, the scaling disappears outside the range where the Gramian matrix W is ill conditioned, leading to considerable errors when computing the matrix inverse. In principle, the scaling regime can be extended with improved computational precision, but not indefinitely. For the networks with an ill conditioned Gramian matrix, not only is the control vector unable to drive the system to the target state, but the associated energy can be extremely large. These observations suggest the following criterion to define physical controllability in terms of the control energy cost: a network is controllable with respect to a specific control setting if and only if the condition number of its Gramian matrix is less than $\bar{C}_W$, a critical number determined by both the measurement or computational error and the required precision of control. For a given set of network parameters (hence a given network ensemble) and control setting, the probability that the condition number of the Gramian matrix is less than $\bar{C}_W$, $P(\bar{C}_W)$, can effectively serve as a quantitative measure of *physical controllability*. Increasing the precision of the computation, e.g., by using special simulation packages with round-off error orders of magnitude smaller than that associated with the conventional double-precision computation, would convert a few uncontrollable cases into controllable ones, but vast majority of the uncontrollable cases remain unchanged.

1.2.2. Structural Controllability Does Not Imply Physical Controllability.

We present evidence that structural and physical controllabilities are not necessarily compatible with each other. Figures 2(a,b) show the percentage of driver nodes, $n_{\mathrm{D}} \equiv N_{\mathrm{D}}/N$, versus the directional link probability P_{b}. We see that n_{D} is minimized for $P_{\mathrm{b}} = 0.5$, indicating a maximal

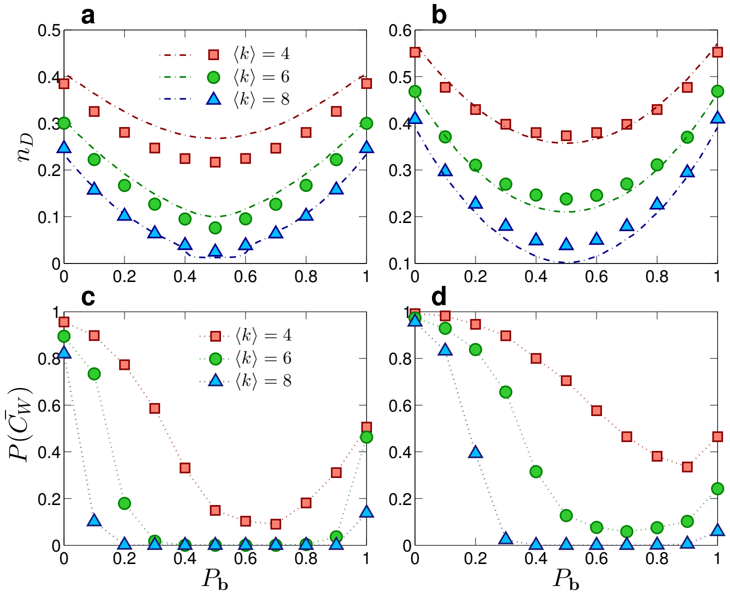

Fig. 2. Structural and physical controllability measures in directed networks. Structural controllability measure n_D versus directional edge probability P_b for (**a**) ER random networks and (**b**) BA scale-free networks of size $N = 1000$ and three values of the average degree ($\langle k\rangle = 4$, 6, and 8). The dash-dotted lines represent the results obtained from the cavity method [4, 5], and the squares, triangles, and circles are simulation results from the maximum matching algorithm [4]. (**c**,**d**) Measure of physical controllability $P(\bar{C}_W)$ for ER random and BA scale-free networks of size $N = 100$, respectively, where $P(\bar{C}_W)$ is the probability that the condition number of the Gramian matrix is less than some physically reasonable threshold value. Comparing (**a**) with (**c**), or (**b**) with (**d**), we observe the striking phenomenon that, in the parameter regime where the number of driver nodes is minimized so that the corresponding networks are deemed to be most structurally controllable, they are physically uncontrollable. The phenomenon persists regardless of the network size and type. All nodes are self-loop free. The qualitative behavior is robust against variations in the value of $\bar{C}_W$.

(optimal) level of structural controllability because only a few control signals are needed to control the whole network [4]. But can physical controllability be achieved in the same parameter regime where structural controllability is optimized? Figures 2(c,d) show the corresponding physical controllability $P(\bar{C}_W)$ versus the network parameter P_b. We see that, in both regimes of small and large P_b values where structural controllability is weak [corresponding to relatively high values of n_D in Figs. 2(a,b)], the physical controllability is relatively strong. In the regime of small P_b values, most directed links in the network point from small to large degree nodes. In this case, the network is more physically controllable, in agreement with intuition. The striking result is that, in the regime of intermediate P_b values (e.g., P_b around 0.5) where the number of driver nodes to control the whole network is minimized so that structural controllability is regarded the strongest, the physical controllability is in fact the weakest, as the probability of the condition number $P(\bar{C}_W)$ being small is close to zero. For example, for the random networks in Fig. 2(c), for $\langle k\rangle = 4$, the minimum value of $P(\bar{C}_W)$ is only about 0.1 for $P_\mathrm{b} \approx 0.6$, while for $\langle k\rangle = 6$ and $\langle k\rangle = 8$, the minimum values are essentially zero. Surprisingly, near zero values of $P(\bar{C}_W)$ occur in a wide range of the parameter P_b, e.g., $[0.3, 0.8]$ and $[0.2, 0.9]$ for $\langle k\rangle = 6$ and $\langle k\rangle = 8$, respectively, as shown in Fig. 2(c). This indicates that the network is physically uncontrollable for most cases where structural controllability is deemed to be strong. BA scale-free networks behave similarly, as illustrated in Fig. 2(d). Another finding from Fig. 2 is that N_D is symmetric about $P_\mathrm{b} = 0.5$, but the symmetry is broken for $P(\bar{C}_\mathrm{W})$, indicating that there is no simple linear correlation between N_D and $P(\bar{C}_\mathrm{W})$. It is thus necessary to find the fundamental structural properties responsible for the smallness of $P(\bar{C}_\mathrm{W})$. Through a detailed analysis of the energy cost associated with controlling a simple one-dimensional chain and a double chain network (**Methods**) and of the energy scaling [27], we identify the longest control chains (LCCs), the shortest paths through which the control energy is “flowed” to all nodes in the network, as the fundamental structural component responsible for the control energy. The longer the LCCs, the more singular the Gramian matrix, and the smaller the probability $P(\bar{C}_{\mathrm{W}})$. The maximal LCC is effectively the *control diameter* of the network [27].

1.2.3. Physical Controllability of An Electrical Circuit Network and a Strategy to Balance Control Energy and Extra Inputs.

To further illustrate the concept of physical controllability, we consider a real one-dimensional cascade parallel RC circuit network, as schematically illustrated in Fig. 3(a). The network can be represented by a bidirectional 1D chain with self-loops for all the nodes, as shown in Fig. 3(b) (see **Methods**). The network size can be enlarged, say by one unit, by attaching an additional branch of resistor and capacitor at the right end of the circuit. The state $u_i(t)$ of node i at time t is the voltage of capacitor i, and the input voltage $u(t)$ represents the control signal. The purpose of control is to drive the voltages of the capacitors from a set of values to another within time t_{f} through the input voltage $u(t)$. The control energy can then be calculated by Eq. (1.3). The actual energy dissipated in the circuit during the control process is given by

$$E_{\text{real}} = \int_0^{t_{\mathrm{f}}} U(t) \cdot I(t) dt, \tag{1.4}$$

where $U(t) \equiv u(t)$ and $I(t)$ are the input voltage and current at time t, respectively, and E_{real} is in units of Joule. By making the circuit equivalent to a 1D chain network, we have three types of energy: the control energy of the actual circuit calculated from Eq. (1.3), the dissipated energy of the circuit from Eq. (1.4), and the control energy of the 1D equivalent network. Figure 3(c) shows that the control energy and the dissipated energy of the circuit do not differ substantially from the energy calculated from the unidirectional 1D chain. Among the three types of energy, the energy cost associated with the control process calculated from Eq. (1.4) is maximal.

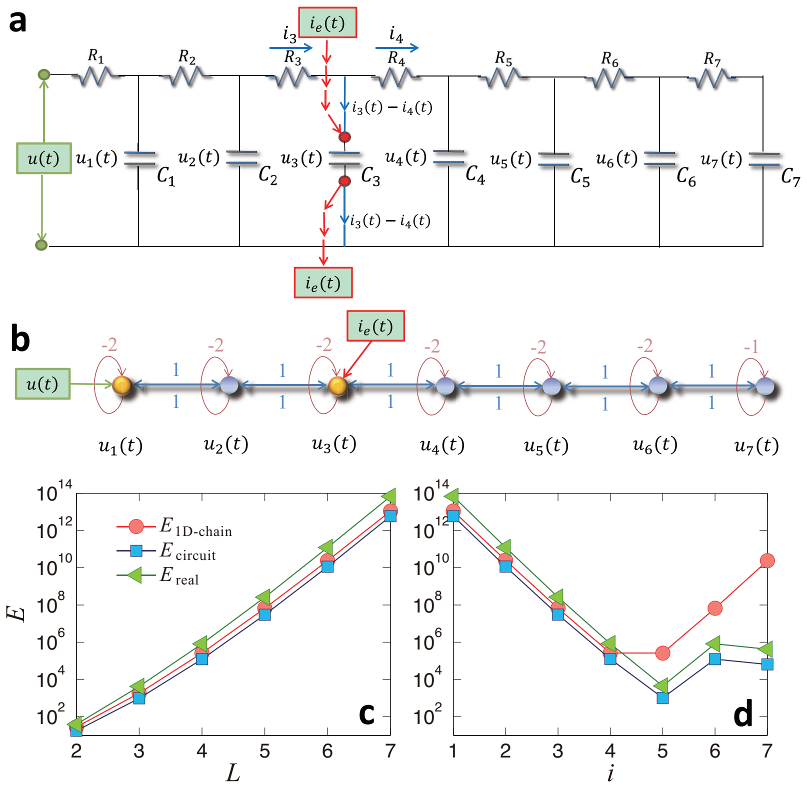

Fig. 3. Illustration of parallel R-C circuit and optimization of control energy. (**a**) A cascade parallel R-C circuit with $L = 7$ resistors (R_1, R_2, $\ldots$, and R_L, each of resistance 1Ω) and 7 capacitors (C_1, C_2, $\ldots$, and C_L, each of capacitance 1F). External voltage input $u(t)$ is applied from the left side of the circuit, and the voltage of capacitor C_i is $u_i(t)(1 \leq i \leq L)$. An extra external current input $i_e(t)$ serves as a redundant control input injected into the capacitor C_3, where i_3 and i_4 denote the currents through resistors R_3 and R_4, respectively. In absence of the extra current input, $i_3(t) - i_4(t)$ is the current through the branch of C_3. (**b**) Network representation of the circuit in (**a**) as a bidirectional 1D chain network of seven nodes, where the external voltage input $u(t)$ is injected into node 1 (yellow driver node, the controller). The dynamical state of node i is described by the voltage of its capacitor, $u_i(t)$. Links (blue) between nodes are bidirectional and have uniform weight 1 in either direction. Each node has a self-link (red) of weight -2, except the ending node (node 7) whose self-link has weight -1. The extra external current input $i_e(t)$ serves as a redundant control input injected into node 3 of the network in (**b**). Now there are two driver nodes (yellow) in the network, nodes 1 and 3. (**c**) Energy required for controlling a unidirectional chain (red circle) and the corresponding circuit (blue square) as well as the dissipated energy (green triangle) of the circuit

Our extensive computations reveal that many structurally controllable networks are not physically controllable due to a combination of the ill-conditioned Gramian matrix and the finite computational or experimental error. Our analysis of the chain model (**Methods**) suggests a simple but effective strategy to reduce the energy significantly so as to enhance the physical controllability of the network: to place extra control signals along the LCCs to break the chains into shorter subchains. (In **Methods**, we show how the redundant control input can be planted in a circuit network.) To be illustrative, we consider a unidirectional 1D chain and add an extra control input at the ith node. As shown in Fig. 3(d), the magnitude of the control energy is reduced dramatically. The optimal location to place the extra control should be near in the middle of the chain so as to minimize the length of the LCC using a minimal number of extra control signals. In Fig. 3(d), the red circles represent a 1D chain and indicate that this simple strategy of adding one redundant control signal near the middle can reduce dramatically the required energy. For the circuit network in Fig. 3, the redundant control input can be realized by inducing external current input into a capacitor. In Fig. 3(d), the real energy is represented by green triangles, which reaches the minimum when the extra input is putting around the middle. Applying a single redundant control input can thus be an extremely efficient strategy to make the one-dimensional chain network physically controllable.

1.2.4. Control Energy Optimization of Complex Networks.

For a complex network, there often exist multiple LCCs, requiring multiple redundant control inputs. With insights from the RC circuit example, we see that a strategy is to place one redundant control input at the middle of each LCC. In this case, each LCC in the network is broken into two subchains. Figure 4(a) shows the effect of this optimization strategy on the energy distribution. For comparison, the same number of redundant control inputs are also applied randomly throughout the network. The reduction ratio between the control energy under optimization strategy, ΔE, and the

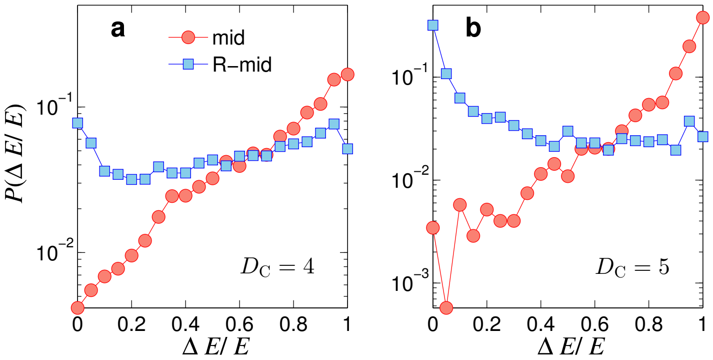

Fig. 4. Effects of redundant control inputs. (**a**) For control diameter $D_{\rm C} = 4$, distribution of the normalized energy reduction $\Delta E/E$ with redundant control in an ensemble of 10000 ER-random networks ($\langle k \rangle = 6$, $P_{\rm b} = 0.1$). Results from the LCC-breaking optimization and random control augmentation are marked by "mid" (red circles) and "R-mid"(blue squares), respectively. For each network, a corresponding number of additional random control inputs are applied to the system 10 times to average out the statistical fluctuations. Panel (**b**) shows the $\Delta E/E$ distributions for networks with control diameter $D_{\rm C} = 5$.

original control energy E characterizes the effectiveness of the optimization process. In particular, if the distribution of $\Delta E/E$ is concentrated on large values of $\Delta E/E$, then the corresponding optimization strategy can be deemed to be effective. As shown in Fig. 4(a), for relatively large $\Delta E/E$ values, $P(\Delta E/E)$ as a result of optimization has values that are systematically larger than those under random control signal augmentation, while the opposite situation is observed for regions with relatively smaller $\Delta E/E$. Thus, our optimization strategy outperforms the random strategy. The networks requiring proper optimization to be physically controlled are typically those with large control diameters. Figures 4(b) show that this is indeed the case: for networks with larger values of D_{C}, the performance of our optimization strategy is significantly better than that with random placement of extra controllers.

1.3. Discussion

As stated in Ref. [4], the ultimate proof that one understands a complex network completely lies in one's ability to control it. However, we find that strong structural controllability is no guarantee that the network can be physically controlled. To resolve this paradox, We develop a physical controllability framework in terms of the control energy cost and the number of external input signals. To illustrate the framework, we focus on the situation where the structural controllability theory yields a minimum number of external input signals required for full control of the network, and determine whether in these situations the control energy is affordable so as to realize actual control. Our systematic computations and analysis reveal a rather unexpected phenomenon: due to the singular nature of the control Gramian matrix, in the parameter regimes where optimal structural controllability is achieved in the sense that the number of driver nodes is minimized, energy cost can be physically impossible to accommodate. To obtain a systematic understanding, we focus on a bidirectional 1D chain and study the relationship between energy and chain length. We then apply the 1D chain model to complex networks based on the idea of LCCs. In fact, the simple chain model captures the scaling behavior of energy distribution found in random networks [23, 27]. The chain model also provides a guiding principle to articulate optimization strategies to reduce the control energy, which are tested using a RC circuit network and model complex networks.

An intuitive picture of the interrelation between mathematical controllability [4, 10] and our physical controllability is the following. In a fictitious world where the Gramian matrix is not singular (regardless of its condition number) and the computer round off or experimental errors are absolutely zero, using N_D controllers as determined by the structural controllability theory can bring the networked system from any initial state to any final state in a given time. However, in the physical world, the inevitable measurement or computational errors will have a devastating consequence in the execution of actual control as the Gramian matrix is typically effectively singular with an arbitrarily large condition number. The dynamical interplay between the error and the singular Gramian matrix makes the system uncontrollable in the sense that it cannot be driven to the final state in finite time within the desirable precision and the energy required in the process diverges. Often, to realize physical control, many more control signals than those determined by the structural controllability theory are needed.

Our work indicates the difficulty of achieving actual control of complex networks associated with even linear dynamics. Although the mathematical controllability theories [4, 10] offer theoretically justified frameworks to guide us to apply external inputs on a minimum set of driver nodes, when we implement control to steer a system to a desired state, the energy consumption is likely to be too large to be affordable. For nonlinear dynamical networks, we continue to lack a general controllability framework and an understanding of required control energy, although progress has been made [22, 41–46]. At the present we still know very little about controlling complex networks

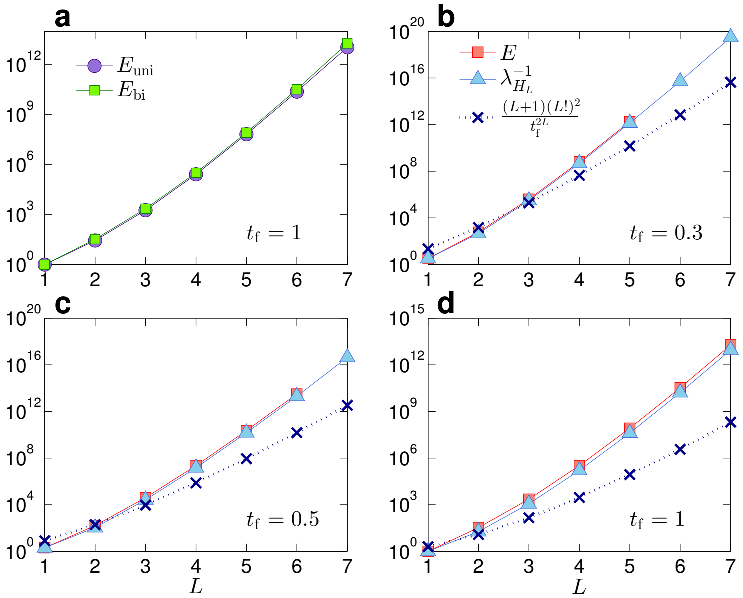

Fig. 5. Control energy for 1D chain. (**a**) Energies required to control a unidirectional chain E_{uni} (purple circles) and a bidirectional one E_{bi} (green squares) versus chain length L. (**b**), (**c**) and (**d**) Control energies of bidirectional chain calculated by simulation (red squares), $\lambda_{H_L}^{-1}$ (azure triangles), and chain length L as shown in Eq. (1.12) (navy crosses) for different values of the control time $t_{\mathrm{f}} = 0.3, 0.5, 1$, respectively.

hosting nonlinear dynamics, and further effort is needed to address this challenging but greatly important problem shared by a wide range of fields.

1.4. Methods

1.4.1. Control Energy of One-Dimensional Chain Model.

To gain insights into how a network's structure affects the control energy, we rewrite Eq. (1.3) as $E(t_{\mathrm{f}}) = \mathbf{x}_0^T \cdot H^{-1} \cdot \mathbf{x}_0$, where $H = e^{-At_{\mathrm{f}}} \cdot W \cdot e^{-A^T t_{\mathrm{f}}}$. Since H is positive definite and symmetric like W, its inverse H^{-1} can be decomposed in terms of its eigenvectors as $H^{-1} = Q \cdot \Lambda \cdot Q^T$, where $Q = [q_1, q_2, \ldots, q_N]$ is composed of the orthonormal eigenvectors that satisfy $Q \cdot Q^T = Q^T \cdot Q = I$, and $\Lambda = \mathrm{diag}\{\lambda_1, \lambda_2, \ldots, \lambda_N\}$ is the diagonal eigenvalue matrix of H^{-1}

in a descending order. Numerically, we find that λ_1 is typically much larger than other eigenvalues. We thus have $E(t_\mathrm{f}) = \mathbf{x}_0^T \cdot Q \cdot \Lambda \cdot Q^T \cdot \mathbf{x}_0 = \sum_{i=1}^N \lambda_i (q_i^T \cdot \mathbf{x}_0)^2 \approx \lambda_1 (q_1^T \cdot \mathbf{x}_0)^2$.

In an undirected network, the adjacency matrix A is positive definite and symmetric. We can decompose A into the form $A = V \cdot S \cdot V^T$, where the columns of V constitute the orthonormal eigenvectors of A and $S = \mathrm{diag}\{s_1, s_2, \ldots, s_N\}$ is the diagonal eigenvalue matrix of A in a descending order. We thus have

$$H = e^{-At_\mathrm{f}} \cdot W \cdot e^{-A^T t_\mathrm{f}} = V \cdot e^{-St_\mathrm{f}} \cdot V^T \cdot W \cdot V \cdot e^{-St_\mathrm{f}} \cdot V^T.$$

Let

$$\Lambda_H = \mathrm{diag}\{\lambda_{H_1}, \lambda_{H_2}, \ldots, \lambda_{H_N}\} = \mathrm{diag}\{1/\lambda_N, 1/\lambda_{N-1}, \ldots, 1/\lambda_1\}$$

be the eigenvalue matrix of H in a descending order. The energy can be expressed as

$$E(t_\mathrm{f}) \approx \lambda_1 (q_1^T \cdot \mathbf{x}_0)^2 = \lambda_{H_N}^{-1} (q_1^T \cdot \mathbf{x}_0)^2. \tag{1.5}$$

We consider a bidiretional 1D chain network and provide an analytical calculation of the relationship between control energy and chain length L. In the undirected chain, the adjacency matrix is defined as

$$A = \begin{bmatrix} 0 & 1 & & & \\ 1 & 0 & \ddots & & \\ & 1 & \ddots & 1 & \\ & & \ddots & 0 & 1 \\ & & & 1 & 0 \end{bmatrix}_{L \times L},$$

the control matrix is $B = [1, 0, \ldots, 0]^T$, and the eigenvalues and eigenvectors of A are, respectively,

$$s_i = 2\cos\left(\frac{\pi}{L+1} i\right), \quad i = 1, \ldots, L, \tag{1.6}$$

$$V_j^{(i)} = \sqrt{\frac{2}{L+1}} \sin\left(\frac{\pi}{L+1} ij\right), \quad i, j = 1, \ldots, L. \tag{1.7}$$

Recall that $H = V \cdot e^{-St_\mathrm{f}} \cdot (\int_0^{t_\mathrm{f}} e^{St} \cdot V^T \cdot B \cdot B^T \cdot V \cdot e^{St}\, \mathrm{d}t) \cdot e^{-St_\mathrm{f}} \cdot V^T$. Substituting this in Eqs. (1.6) and (1.7), after some algebraic manipulation, we obtain

$$H = \frac{1}{L+1} V \cdot D \cdot P \cdot D \cdot V^T, \tag{1.8}$$

where $D = \mathrm{diag}\{\sin(\theta), \sin(2\theta), ..., \sin(L\theta)\}$. and $P_{jk} = \int_0^{2t_\mathrm{f}} e^{-[\cos(j\theta)+\cos(k\theta)]t}\, \mathrm{d}t$ with $\theta = \pi/(L+1)$, $j, k = 1, \cdots, L$.

The Rayleigh-Ritz theorem can be used to bound P as:

$$\lambda_{P_L} \leq \frac{\mathbf{y}^T \cdot P \cdot \mathbf{y}}{\mathbf{y}^T \cdot \mathbf{y}} \leq \lambda_{P_1},$$

and $\mathbf{y} = [y_1, y_2, \ldots, y_L]^T$ is an arbitrary nonzero column vector, λ_{P_L} and λ_{P_1} are the maximal and minimal eigenvalues of P, respectively. Letting $T = 2t_\mathrm{f}$, we have

$$\begin{aligned}
\mathbf{y}^T \cdot P \cdot \mathbf{y} &= (y_1 \cdots y_L) \left[\int_0^T e^{-[\cos(j\theta)+\cos(k\theta)]\tau}\, \mathrm{d}\tau \right]_{L \times L} \begin{pmatrix} y_1 \\ \vdots \\ y_L \end{pmatrix} \\
&= \sum_{j,k=1}^{L} y_j y_k \int_0^T e^{-[\cos(j\theta)+\cos(k\theta)]\tau}\, \mathrm{d}\tau \\
&= \langle \sum_{j=1}^{L} y_j e^{-[\cos(j\theta)]t}, \sum_{j=1}^{L} y_j e^{-[\cos(j\theta)]t} \rangle,
\end{aligned} \tag{1.9}$$

with $\langle f, g \rangle \equiv \int_0^T fg\, \mathrm{d}\tau$. Letting $b_j = e^{-\cos(j\theta)}$ and performing a Taylor expansion on b_j^t around $t = 0$, we obtain $b_j^t = \sum_{k=0}^{L-1} [-\cos(j\theta)]^k \frac{t^k}{k!} + [-\cos(j\theta)]^L \frac{t_j^L}{L!}$, with $t_j \in [0, T]$. Now letting $q_j(t) = \sum_{k=0}^{L-1} [-\cos(j\theta)]^k \frac{t^k}{k!}$, we have $b_j^t = q_j(t) + [-\cos(j\theta)]^L \cdot (t_j^L / L!)$. Consequently, the numerator in the Rayleigh quotient can be expressed as

$$\begin{aligned}
\mathbf{y}^T \cdot P \cdot \mathbf{y} =& \langle \sum_{j=1}^{L} y_j b_j^t, \sum_{j=1}^{L} y_j b_j^t \rangle \\
=& \langle \sum_{j=1}^{L} \left(y_j q_j(t) + y_j [-\cos(j\theta)]^L \frac{t_j^L}{L!} \right), \sum_{j=1}^{L} \left(y_j q_j(t) + y_j [-\cos(j\theta)]^L \frac{t_j^L}{L!} \right) \rangle \\
=& \langle \sum_{j=1}^{L} y_j q_j(t), \sum_{j=1}^{L} y_j q_j(t) \rangle + 2 \langle \sum_{j=1}^{L} y_j q_j(t), \sum_{j=1}^{L} y_j [-\cos(j\theta)]^L \frac{t_j^L}{L!} \rangle \\
& + \langle \sum_{j=1}^{L} y_j [-\cos(j\theta)]^L \frac{t_j^L}{L!}, \sum_{j=1}^{L} y_j [-\cos(j\theta)]^L \frac{t_j^L}{L!} \rangle \\
\leq & \underbrace{\langle \sum_{j=1}^{L} y_j q_j(t), \sum_{j=1}^{L} y_j q_j(t) \rangle}_{\text{Denote as } K_1} + \underbrace{2 \frac{T^L}{L!} \sum_{k=1}^{L} |y_k| \left(\left| \langle \sum_{j=1}^{L} y_j q_j(t), 1 \rangle \right| \right)}_{\text{Denote as } K_2} \\
& + \underbrace{\left(\frac{T^L}{L!} \right)^2 \sum_{j,k=1}^{L} |y_j y_k| T}_{\text{Denote as} K_3} . \qquad (1.10)
\end{aligned}$$

Since $\mathbf{y} = [y_1, y_2, \ldots, y_L]^T$ is an arbitrary nonzero column vector, for each L and T, we can choose $\mathbf{y} = \mathbf{y}_m$ insofar as K_1 and K_2 are relatively small compared with K_3. We can normalize $\mathbf{y}_m^T \cdot \mathbf{y}$ to arrive at

$$\lambda_{P_L} \leq \frac{\mathbf{y}_m^T \cdot P \cdot \mathbf{y}_m}{\mathbf{y}_m^T \cdot \mathbf{y}_m} = \left(\frac{T^L}{L!} \right)^2 \sum_{j,k=1}^{L} |y_{m_j} y_{m_k}| T \sim \mathcal{O}\left(\frac{T^{2L}}{(L!)^2} \right), \qquad (1.11)$$

where λ_{P_L} is the smallest eigenvalue of P. Since P is symmetric and positive definite, using Cholesky decomposition we can obtain its factorization [40] as $P = U^T \cdot U$, where U is the upper triangular matrix with its diagonal being the square roots of eigenvalues of P. Equation (1.8) can then be written as $H = \frac{1}{L+1} V \cdot D \cdot U^T \cdot U \cdot D \cdot V^T$. Since orthonormal transform does not change the eigenvalues of a matrix, H has the same eigenvalues as $R = \frac{1}{L+1} D \cdot U^T \cdot U \cdot D = \frac{1}{L+1} D \cdot U^T \cdot (D \cdot U^T)^T$. Suppose $\Lambda_P = \text{diag}\{\lambda_{P_1}, \lambda_{P_2}, \ldots, \lambda_{P_L}\}$ is the diagonal eigenvalue matrix of P in a descending order. We then have

$$\lambda_{H_j} = \lambda_{R_j} = \frac{1}{L+1} \lambda_{P_j} (\sin k\theta)^2 \leq \frac{1}{L+1} \lambda_{P_j},$$

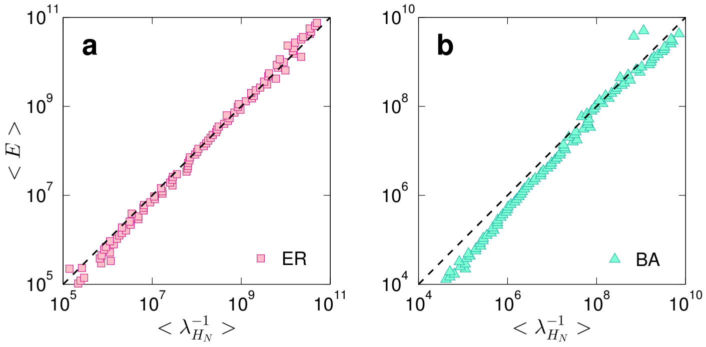

Fig. 6. Correlation between network control energy and the smallest eigenvalue of H-matrix. Network size is $N = 100$, directional link probability between any pair of nodes is $P_\mathrm{b} = 0.1$, and average degree is (**a**) $\langle k \rangle = 6$ for ER random networks and (**b**) $\langle k \rangle = 8$ for BA sale-free networks.

where j and k run from 1 to L. For arbitrary but fixed $\mathbf{x_0}$, the control energy $E(t_\mathrm{f})$ can be approximated as

$$E(t_\mathrm{f}) \sim \mathcal{O}(\lambda_{H_L}^{-1}) = \mathcal{O}\left((L+1)\frac{(L!)^2}{t_\mathrm{f}^{2L}}\right), \tag{1.12}$$

where we see that $E(t_\mathrm{f})$ increases faster than exponential with L. As shown in Fig. 5(a), the energy required to control a unidirectional 1D chain nearly overlaps with that of a bidirectional one with identical weights. From Figs. 5(b,c,d) we see that Eq. (1.12) provides a reasonably accurate estimate of the control energy.

Furthermore, we find numerically that Eq. (1.5) holds for random and scale-free networks. As shown in Fig. 6, there is a strong correlation between the average network control energy, $\langle E \rangle$, and the smallest eigenvalue of the H-matrix, $\lambda_{H_N}^{-1}$, for ER random and BA scale-free networks, indicating that the network control energy is essentially determined by the smallest eigenvalue of its H-matrix.

1.4.2. Network Representation of a Circuit System.

We consider a cascade parallel R-C circuit consisting of three identical resistors and capacitors as an example to illustrate how the circuit can be abstracted into a directed network, as shown in Fig. 7. For convenience, we set $R_1 = R_2 = R_3 = R$ and $C_1 = C_2 = C_3 = C$, and denote the currents through R_1, R_2, and R_3 as $i_1(t)$, $i_2(t)$, and $i_3(t)$, respectively. The equations of the circuit are

$$\begin{cases} u(t) = i_1(t)R + u_1(t) \\ u_1(t) = i_2(t)R + u_2(t) \\ u_2(t) = i_3(t)R + u_3(t) \\ C\frac{\mathrm{d}u_1(t)}{\mathrm{d}t} = i_1(t) - i_2(t) \\ C\frac{\mathrm{d}u_2(t)}{\mathrm{d}t} = i_2(t) - i_3(t) \\ C\frac{\mathrm{d}u_3(t)}{\mathrm{d}t} = i_3(t) \end{cases} \tag{1.13}$$

After some algebraic manipulation, we have

$$\begin{cases} \frac{\mathrm{d}u_1(t)}{\mathrm{d}t} = -\frac{2}{RC}u_1(t) + \frac{1}{RC}u_2(t) + \frac{1}{RC}u(t) \\ \frac{\mathrm{d}u_2(t)}{\mathrm{d}t} = \frac{1}{RC}u_1(t) - \frac{2}{RC}u_2(t) + \frac{1}{RC}u_3(t) \\ \frac{\mathrm{d}u_3(t)}{\mathrm{d}t} = \frac{1}{RC}u_2(t) - \frac{1}{RC}u_3(t), \end{cases} \tag{1.14}$$

which can be written as

$$\begin{pmatrix} \frac{\mathrm{d}u_1(t)}{\mathrm{d}t} \\ \frac{\mathrm{d}u_2(t)}{\mathrm{d}t} \\ \frac{\mathrm{d}u_3(t)}{\mathrm{d}t} \end{pmatrix} = \begin{pmatrix} -\frac{2}{RC} & \frac{1}{RC} & 0 \\ \frac{1}{RC} & -\frac{2}{RC} & \frac{1}{RC} \\ 0 & \frac{1}{RC} & -\frac{1}{RC} \end{pmatrix} \begin{pmatrix} u_1(t) \\ u_2(t) \\ u_3(t) \end{pmatrix} + \begin{pmatrix} \frac{1}{RC} \\ 0 \\ 0 \end{pmatrix} u(t). \tag{1.15}$$

Setting $R = 1\Omega$ and $C = 1F$, we have

$$\begin{pmatrix} \frac{\mathrm{d}u_1(t)}{\mathrm{d}t} \\ \frac{\mathrm{d}u_2(t)}{\mathrm{d}t} \\ \frac{\mathrm{d}u_3(t)}{\mathrm{d}t} \end{pmatrix} = A \cdot \begin{pmatrix} u_1(t) \\ u_2(t) \\ u_3(t) \end{pmatrix} + B \cdot u(t), \tag{1.16}$$

where

$$A = \begin{pmatrix} -2 & 1 & 0 \\ 1 & -2 & 1 \\ 0 & 1 & -1 \end{pmatrix} \tag{1.17}$$

is the adjacency matrix of the network representing the circuit, and

$$B = \begin{pmatrix} 1 \\ 0 \\ 0 \end{pmatrix} \tag{1.18}$$

is the control input matrix. The circuit has thus been transferred into a 3-node bidirectional 1D chain network with adjacency matrix A.

1.4.3. Implementation of Extra Control Input in the Circuit System.

Without loss of generality, we inject an extra external current input $i_\mathrm{e}(t)$ into the capacitor C_2, and the circuit equations become:

$$\begin{cases} u(t) = i_1(t)R + u_1(t) \\ u_1(t) = i_2(t)R + u_2(t) \\ u_2(t) = i_3(t)R + u_3(t) \\ C\frac{\mathrm{d}u_1(t)}{\mathrm{d}t} = i_1(t) - i_2(t) \\ C\frac{\mathrm{d}u_2(t)}{\mathrm{d}t} = i_2(t) - i_3(t) + i_\mathrm{e}(t) \\ C\frac{\mathrm{d}u_3(t)}{\mathrm{d}t} = i_3(t) \end{cases} \tag{1.19}$$

The state equations are

$$\begin{pmatrix} \frac{\mathrm{d}u_1(t)}{\mathrm{d}t} \\ \frac{\mathrm{d}u_2(t)}{\mathrm{d}t} \\ \frac{\mathrm{d}u_3(t)}{\mathrm{d}t} \end{pmatrix} = A \cdot \begin{pmatrix} u_1(t) \\ u_2(t) \\ u_3(t) \end{pmatrix} + B_\mathrm{e} \cdot \begin{pmatrix} u(t) \\ i_\mathrm{e}(t) \end{pmatrix}, \tag{1.20}$$

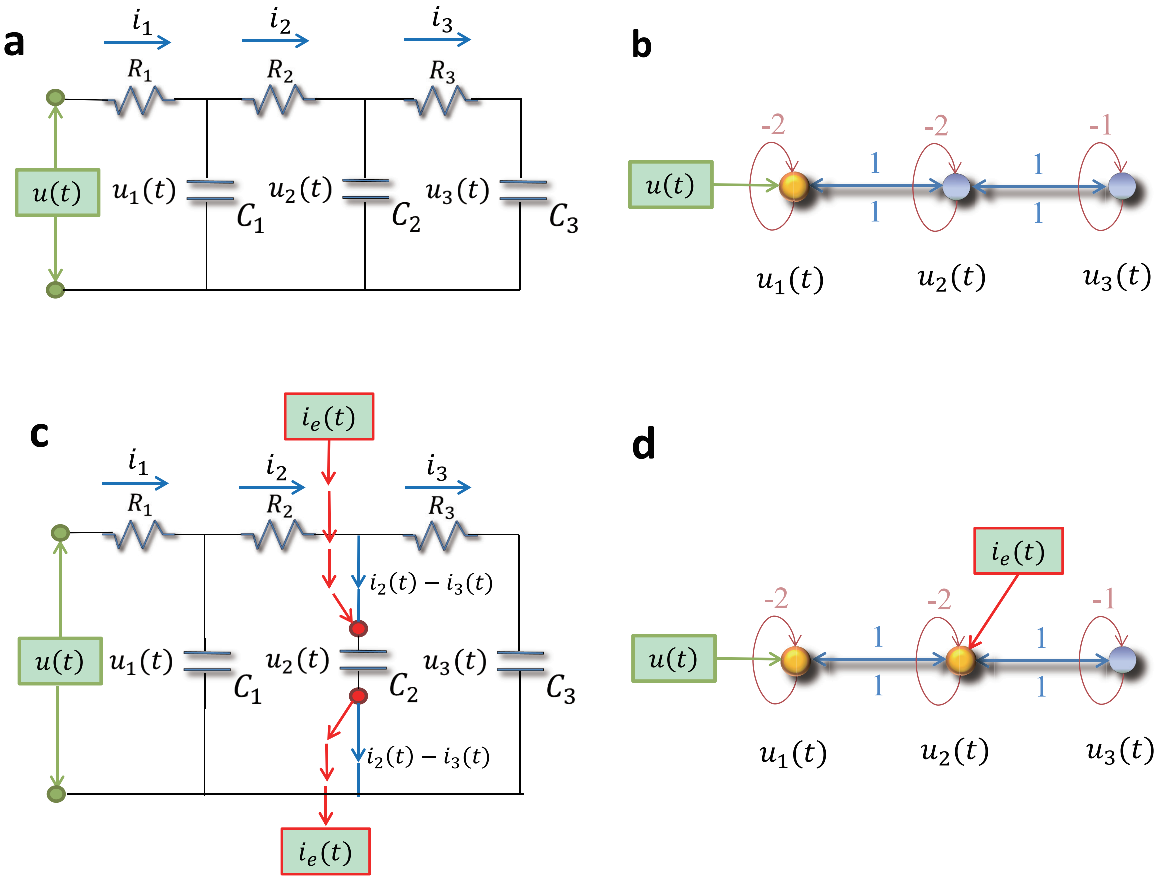

Fig. 7. Controlling and optimizing a cascade parallel RC circuit system and the corresponding network presentation. (**a**) A cascade parallel R-C circuit with 3 resistors (R_1, R_2, and R_3, each of resistance 1Ω) and 3 capacitors (C_1, C_2, and C_3, each of capacitance 1F), where $u(t)$ is the external input voltage, $u_1(t)$, $u_2(t)$, and $u_3(t)$ are the voltages on the capacitors C_1, C_2, and C_3, and $i_1(t)$, $i_2(t)$, and $i_3(t)$ are the currents through the resistors R_1, R_2, and R_3, respectively. (**b**) Network representation of the circuit in (**a**). (**c**) Circuit with an extra external current input $i_{\mathrm{e}}(t)$ into the capacitor C_2. (**d**) The extra external current input $i_{\mathrm{e}}(t)$ serves as a redundant control input injected into node 2 of the network in (**b**). There are two driver nodes (yellow) in the network: 1 and 2.

where

$$B_{\mathrm{e}} = \begin{pmatrix} 1 & 0 \\ 0 & 1 \\ 0 & 0 \end{pmatrix} \tag{1.21}$$

is the control input matrix of the circuit under the original control input $u(t)$ on node 1 and a redundant control input $i_{\mathrm{e}}(t)$ to node 2. Similarly, the redundant control input can be injected into any capacitor.

It is necessary to keep all other nodes unaffected while introducing exactly one extra control input into the circuit. However, any additional voltage change in any part of the circuit can lead to voltage changes on all the capacitors. A change in the current through a capacitor will not affect the currents in other components of the network, since only the time derivative of its voltage is affected. Thus, a meaningful way to introduce an extra control signal input to one node of a circuit's network is to inject current into one particular capacitor in the circuit.

2 . A GEOMETRICAL APPROACH TO CONTROL AND CONTROLLABILITY OF NONLINEAR DYNAMICAL NETWORKS

In spite of the recent interest and advances in linear controllability of complex networks, controlling nonlinear network dynamics remains an outstanding problem. We develop an experimentally feasible control framework for nonlinear dynamical networks that exhibit multistability (multiple coexisting final states or attractors), which are representative of, e.g., gene regulatory networks (GRNs). The control objective is to apply parameter perturbation to drive the system from one attractor to another, assuming that the former is undesired and the latter is desired. To make our framework practically useful, we consider *restricted* parameter perturbation by imposing the following two constraints: (a) it must be experimentally realizable and (b) it is applied only temporarily. We introduce the concept of *attractor network*, in which the nodes are the distinct attractors of the system, and there is a directional link from one attractor to another if the system can be driven from the former to the latter using restricted control perturbation. Introduction of the attractor network allows us to formulate a controllability framework for nonlinear dynamical networks: a network is more controllable if the underlying attractor network is more strongly connected, which can be quantified. We demonstrate our control framework using examples from various models of experimental GRNs and the beneficial role of noise in facilitating control.

2.1. Introduction

An outstanding problem in interdisciplinary research is to control nonlinear dynamics on complex networks. Indeed, the physical world in which we live is nonlinear, and complex networks are ubiquitous in a variety of natural, social, economical, and man-made systems. Dynamical processes on complex networks are thus expected to be generically nonlinear. While the ultimate goal to study complex systems is to control them, the coupling between nonlinear dynamics and complex network structure presents tremendous challenges to our ability to formulate effective control methodologies. In spite of the rapid development of network science and engineering toward understanding, analyzing and predicting the dynamics of large complex network systems in the past fifteen years, the problem of controlling nonlinear dynamical networks has remained open.

In the past several years, a framework for determining the *linear* controllability of network based on the traditional control and graph theories emerged [4, 7, 8, 10, 14–16, 22, 23, 47], leading to a quantitative understanding of the effect of network structure on its controllability. In particular, a structural controllability framework was proposed [4], revealing that the ability to steer a complex network toward any desired state, as measured by the minimum number of driver nodes, is determined by the set of maximum matching, which is the maximum set of links that do not share starting or ending nodes. A main result was that the number of driver nodes required for full control is determined by the network's degree distribution [4]. The framework was established for weighted and directed networks. An alternative framework, the exact controllability framework, was subsequently formulated [10], which was based on the principle of maximum multiplicity to identify the minimum set of driver nodes required to achieve full control of networks with arbitrary structures and link weight distributions. Generally, a limitation of such rigorous mathematical frameworks of controllability is that the nodal dynamical processes must be assumed to be *linear*. For nonlinear dynamical networks, to establish a mathematical controllability framework similar to those based on the classic Kalman's rank condition [29] for linear networks is an unrealistically broad objective. Traditionally, controllability for nonlinear control can be formulated based on Lie brackets [48], but to extend the abstract framework to complex networks may be difficult. A recent work extended the linear controllability and observability theory to nonlinear networks with symmetry [22]. In spite of the previous works, at the present there is no known general framework for controlling nonlinear dynamics on complex networks.

Due to the high dimensionality of nonlinear dynamical networks and the rich variety of behaviors that they can exhibit, it may be prohibitively difficult to develop a control framework that is universally applicable to different kinds of network dynamics. In particular, the classic definition of linear controllability, i.e., a network system is controllable if it can be driven from an arbitrary initial state to an arbitrary final state in finite time, is generally not applicable to nonlinear dynamical networks. Instead, controlling collective dynamical behaviors may be more pertinent and realistic. Our viewpoint is that, for nonlinear dynamical networks, control strategies may need to be specific and system-dependent. The purpose of this paper is to articulate control strategies and develop a controllability framework for nonlinear networks that exhibit multistability. A defining characteristic of such systems is that, for a realistic parameter setting, there are multiple coexisting attractors in the phase space [49, 50]. The goal is to drive the system from one attractor to another using physically meaningful, temporary and finite parameter perturbation, assuming that the system is likely to evolve into an undesired state (attractor) or the system is already in such a state and one wishes to implement control to bring the system out of the undesired state and steer it into a desired one.

In biology, nonlinear dynamical networks with multiple attractors have been employed to understand fundamental phenomena such as cancer mechanisms [51], cell fate differentiation [52–55], and cell cycle control [56, 57]. For example, Boolean network models were used to study gene evolution [58], attractor number variation with asynchronous stochastic updating [59], gene expression in the state space [53], and organism system growth rate improvement [60]. Another approach is to abstract key regulation genetic networks [61, 62] (or motifs) from all associated interactions, and to employ synthetic biology to modify, control and finally understand the biological mechanisms within these complicated systems [52, 56]. An earlier application of this approach led to a good understanding of the ubiquitous phenomenon of bistability in biological systems [63], where there are typically limit cycle attractors and, during cell cycle control, noise can trigger a differentiation process by driving the system from a limit circle to another steady state attractor [52]. Generally speaking, there are two candidate mechanisms for transition or switching between different attractors [54]: through signals transmitted within cells and through noise, which were demonstrated recently using synthetic genetic circuits [64]. More recently, a detailed numerical study was carried out of how signal-induced bifurcations in a tri-stable genetic circuit can lead to transitions among different cell types [55].

In this paper, we develop a control and controllability framework for nonlinear dynamical networks based on the concept of *attractor networks* [44]. An attractor network is defined in the phase space of the underlying nonlinear system, in which each node represents an attractor and a directed edge from one node to another indicates that the system can be driven from the former to the latter using experimentally feasible, temporary, and finite parameter changes. A well connected attractor network implies a strong feasibility that the system can be controlled to reach a desired attractor. The connectivity of the attractor network can then be used to characterize the controllability of the nonlinear dynamical network. More specifically, for a given pair of attractors, the relative weight of the shortest path is the number of accessible control parameters whose adjustments can lead to the attractor transition as specified by the path. We use gene regulatory networks (GRNs) to demonstrate the *practicality* of our control framework, which includes low-dimensional, experimentally realizable synthetic gene circuits and a realistic T-cell cancer network of 60 nodes. A finding is that noise can facilitate control by reducing the required amplitude of the control signal. We emphasize that the development of our nonlinear control framework is based entirely on physical considerations, rendering feasible experimental validation.

2.2. Results

A complex, nonlinear dynamical network of N variables can be described by a set of N coupled differential equations:

$$\dot{\mathbf{x}} = \mathbf{F}(\mathbf{x}, \mu), \tag{2.1}$$

where $\mathbf{x} \in \mathbf{R}^N$ denotes the N-dimensional state variable, $\mathbf{F}(\mathbf{x}, \mu)$ is the nonlinear vector field, and $\mu \in \mathbf{R}^M$ represents the set of coupling parameters. In a GRN, the nodal dynamics is typically one dimensional. For simplicity, we assume that this is the case to be treated so that the size of the network represented by Eq. (2.1) is N. From consideration of realistic GRNs, we assume that the coupling parameters can be adjusted externally, which are effectively the set of *control parameters*. Specifically, for a GRN, we assume that the various coupling strengths among the nodes (genes) can be experimentally and systematically varied through application of specific targeted drugs. On a larger scale, the fate of a cell can be controlled by adding drugs to the cell-growth environment, which adjust the interaction parameters in the underlying network [63]. While dynamical variables themselves can also be perturbed for the purpose of control, for GRNs this is unrealistic. For this reason the scenario of perturbing dynamical variables will not be considered in this paper.

We focus on nonlinear dynamical networks with *multiple* coexisting attractors. For a given set of parameters μ, the multiple attractors (e.g., stable steady states) and the corresponding basins are fixed. In the absence of stochasticity, for a given initial condition, the system will approach one of the attractors. Each attractor has specific biological significance, which can be regarded as either desired or undesired, depending on the particular function of interest. Suppose, without any control, the system is in an undesired attractor or is in its basin of attraction. The question is how to steer the system from the undesired state to a desired state by means of *temporary and small* parameter variations that are experimentally feasible.

2.2.1. Control Principle Based on Bifurcation.

To motivate the development of a feasible control principle, we consider the simple case where the system is near a bifurcation point and control is to be applied to drive the system from one attractor to another through temporal perturbation to a *single* parameter. That is, the parameter variation is turned on and takes effect for a finite (typically short) duration of time. After control perturbation is withdrawn, the system is restored to its parameter setting before control but its state has been changed: the system will have moved to the basin of the desired attractor and will approach the desired attractor spontaneously. Let μ_0 be the initial parameter value and the system is in an undesired attractor denoted as $\mathbf{x}_{\mathrm{i}}^*$, and let $\mathbf{x}_{\mathrm{f}}^*$ be the desired attractor to which the system is driven. Imposing control means that we change the parameter from μ_0 to μ_1. The dynamical mechanism to drive the system out of the initial attractor is bifurcations, e.g., a saddle-node bifurcation at which the original attractor disappears and its basin is absorbed into that of an *intermediate attractor* [57], denoted as $\bar{\mathbf{x}}_{\mathrm{k}}^*$. Turning on control to change μ from μ_0 to μ_1 thus makes the system approach $\bar{\mathbf{x}}_{\mathrm{k}}^*$. This process continues until the system falls into the original basin of $\mathbf{x}_{\mathrm{f}}^*$, at which point the control parameter is reset to its original value μ_0 so that the system will approach the desired attractor $\mathbf{x}_{\mathrm{f}}^*$. Success of control relies on the existence of a "path" from the initial attractor to the final one through a number of intermediate attractors. If a single parameter is unable to establish such a path, variations in multiple parameters can be considered, *provided that such parameter adjustments are experimentally realizable*. For a biological network, this can be achieved through application of a combined set of drugs [65, 66]. However, even when potential complications induced by inter-drug interactions are neglected, the search space for suitable parameter perturbation can be prohibitively large if we allow all available parameters to be adjusted simultaneously. We demonstrate below that this challenge can be met by constructing an *attractor network* for the underlying system.

We note that, not only is it now feasible to perturb gene expressions directly, but the technology for fine-tuning regulation strengths is also commonly available. For example, in our previous synthetic biology studies [64, 67], we used chemical inducers such as aTc, IPTG, and Arabinose to fine tune the strength of inhibition or activation. These chemical inducers do not change the protein abundance but rather chemically modify the protein structures upon binding so as to change their functions including binding affinity. Other techniques such as RNAi can also be used to fine-tune gene regulation strength. In general, there are many different ways to tune gene regulation without chaining its transcription and translation.

2.2.2. Attractor Network for the T-Cell Signaling Network.

For a complex, nonlinear dynamical network, an attractor network can be constructed by defining each of all possible attractors of the system as a node. There exists a directed link from one node to another if an experimentally accessible parameter of the system can be adjusted to drive or control the system from the former to the latter. There can be multiple edges from one node to another, if there are multiple parameters, each enabling control. Starting from an initial attractor, one can identify, using all accessible parameters with variations in a physically reasonable range, a set of attractors that the system can be driven into. Repeating this procedure for all attractors in the system, we build up an attractor network that provides a *blueprint* for driving the whole networked system from any attractor to any other attractor in the system, assuming at the time the latter attractor would lead to desired function of the system as a whole. As we can see from following examples, all these can be done using relatively small parameter perturbation in the sense that the

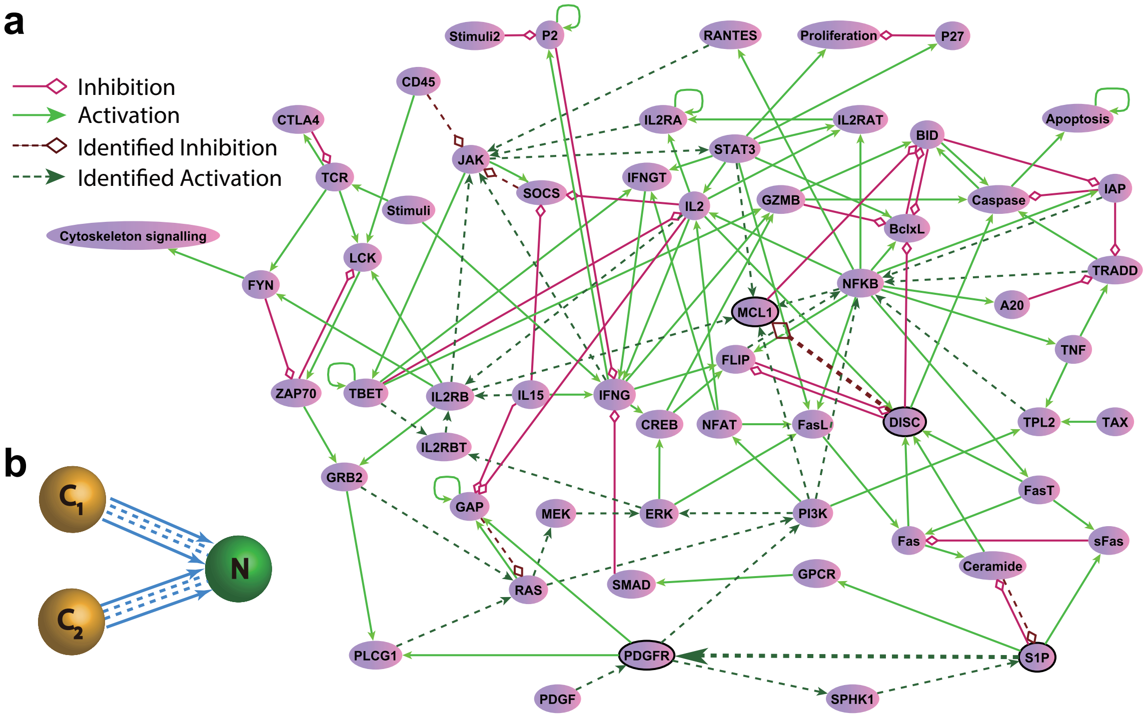

Fig. 8. T-cell survival signaling network and its attractor network. (a) Structure of T-cell survival network: each node is labeled with its generic name, and the arrowhead and diamond-head edges represent activation and inhibition regulations, respectively. The inhibitory edges from "Apoptosis" to other nodes are not shown (for clarity). (b) Attractor network of the T-cell network, which contains three nodes: two cancerous states denoted as $\mathbf{C}_1$ and $\mathbf{C}_2$ and a normal state denoted as $\mathbf{N}$. The two directed edges in the attractor network are multiple, each containing altogether 48 individual edges corresponding to controlling the 48 edges in the original network, which are indicated by the dark dashed lines, whereas the remaining edges in the original network are signified by the light solid lines. Our detailed computations reveal that parameter perturbation on any one of the 48 edges can drive the system from a cancerous state to the normal state. That is, regardless of whether the initial state is $\mathbf{C}_1$ or $\mathbf{C}_2$, with a proper modification to one of the 48 parameters, the system can be driven to the normal state $\mathbf{N}$.

modifications are small as compared with the ranges over which the corresponding parameters can vary.

To demonstrate the construction of attractor networks, we take as an example a realistic biological network, T cells in large granular lymphocyte (T-LGL) leukemia associated with blood cancer. Specifically, apoptosis signaling of the T cells can be described by a network model: T-cell survival signaling network [68, 69], which has 60 nodes and 195 regulatory edges, as shown in Fig. 8(a). Nodes in the network represent proteins and transcripts, and the edges correspond to either *activation* or *inhibitory* regulations. Experimentally, it was found that there are three attractors for this biophysically detailed network [68, 69]. Among the three attractors, two correspond to two distinct cancerous states (denoted as $\mathbf{C}_1$ and $\mathbf{C}_2$) and one is associated with the normal state (denoted as $\mathbf{N}$). The two cancerous states are biologically equivalent, differing only on node P2 (either activated or inactivated). Since the T-LGL leukemia disease originates from the failure of the programmed T-cell, the normal state corresponds to the situation where the node Apoptosis is activated while all other nodes are inactivated. By translating the Boolean rules into a continuous form using the method in [70, 71] and setting the strength of each edge to unity, one can obtain a set of nonlinear dynamical equations for the entire network system. Direct simulation of the model indicates that there are three stable fixed point attractors, in agreement with the experimental observation [68, 69]. The attractor network is thus quite simple: it has three nodes only, as shown in Fig. 8(b). Testing all the 195 experimentally adjustable parameters, we find 48 edges from each cancerous attractor to the normal one (see Supplementary Table 1). Our detailed computations reveal that parameter perturbation on any one of the 48 edges can drive the system from a cancerous state to the normal state. That is, regardless of whether the initial state is $\mathbf{C}_1$ or $\mathbf{C}_2$, with a proper modification to one of the 48 parameters, the system can be driven to the normal state $\mathbf{N}$. Since the goal of control is to bring the system from one of the cancerous states to the normal one, it is not necessary (or biologically meaningful) to test whether parameter perturbation exists that drives the system from the normal node to a cancerous node.

2.2.3. Control Implementation Based on Attractor Network.

Given a nonlinear dynamical network in the real (physical) space, the underlying phase space dimension may be quite high, rendering analysis of the dynamical behaviors difficult. The attractor network is a coarse grained representation of the phase space, retaining information that is most relevant to the control task of driving the network system to a desired final state. Once an attractor network has been constructed, actual control can be carried out through temporary changes in a set of experimentally adjustable parameters, one at a time. This should be contrasted to one existing approach [72] that requires accurate adjustments in the state variables, which may not always be realistic.

We detail how actual control can be implemented based on the attractor network for the T-cell system. To be concrete, we assume that the control signal has the shape of a rectangular pulse in the plot of a parameter versus the time, as shown in Fig. 9(a), where the control parameter is μ and the rectangular pulse has duration τ and amplitude $\Delta\mu = |\mu_{\rm n} - \mu_0|$, with μ_0 denoting the nominal parameter value and $\mu_{\rm n}$ being the value during the time interval when control is on. For the T-cell network, we set $\mu_0 = 1.0$. As μ is reduced the system approaches a bifurcation point. (In other examples a bifurcation can be reached by increasing a control parameter, as in the low-dimensional GRNs detailed in **Methods**.) Extensive numerical simulations for controlling the T-cell network from a cancerous state ($\mathbf{C}_1$ or $\mathbf{C}_2$) to the normal state $\mathbf{N}$ shows that, to achieve control, there are wide ranges of choices for $\Delta\mu$ and τ. In fact, once $\mu_{\rm n}$ is decreased through the bifurcation point $\mu_{\rm c}$ at which the initial attractor loses its stability, the goal of control can be realized. The critical value

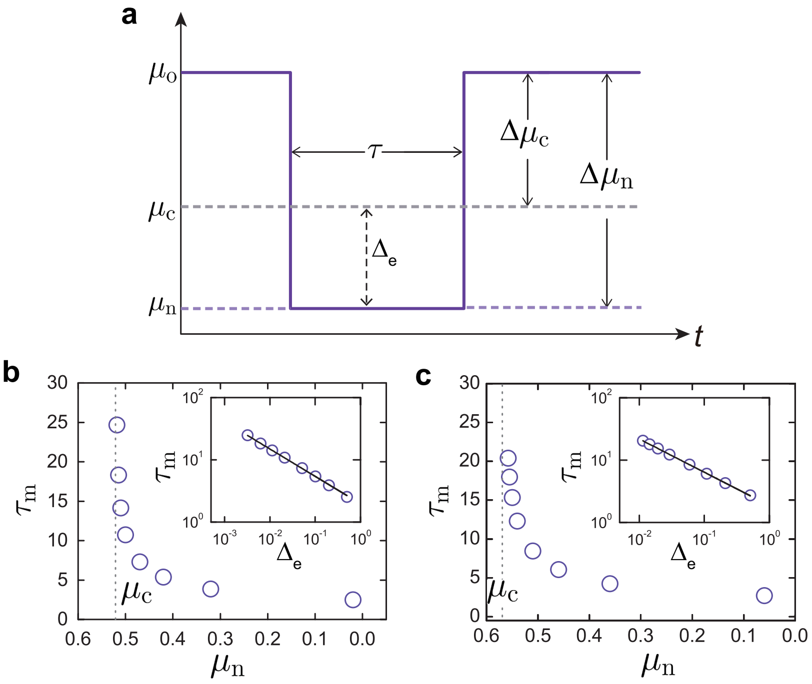

Fig. 9. Relationship between edge control strength and minimal control time. For the T-cell network, (a) an inverted rectangular control signal of duration τ and amplitude $\Delta\mu_n = |\mu_n - \mu_0|$, where μ_0 is the original parameter value and μ_n is the control parameter value. A saddle-node bifurcation occurs for $\mu = \mu_c$, so $\Delta_e = \mu_c - \mu_n$ is the excessive amount of the parameter change over the critical value μ_c. (b,c) Minimal control time τ_m versus μ_n, where parameter control is applied to the activation edge from node "S1P" to node "PDGFR" and to the inhibitory edge from "DISC" to "MCL1", respectively. These four nodes are indicated with the solid black circles in Fig. 8(a). The corresponding plots on a logarithmic scale in the insets of (b) and (c) suggest a power-law scaling behavior between τ_m and Δ_e [Eq. (2.2)]. The fitted power-law scaling exponents are $\beta \approx -0.44$, and -0.55, respectively, for (b) and (c).

μ_c for each parameter can be identified from the bifurcation analysis. Additionally, for $\mu_\mathrm{n} < \mu_\mathrm{c}$, there exists a required minimum control time τ_m, over which the system will move into the original basin of the target attractor before control is activated. Insofar as $\tau > \tau_\mathrm{m}$, the control signal can be released. Longer duration of control is not necessary since the system will evolve into the target attractor following its natural dynamical evolution associated with the nominal parameter μ_0. The value of τ_m increases as μ_n is closer to μ_c, where if $\mu_\mathrm{n} = \mu_\mathrm{c}$, τ_m is infinite due to the critical slowing down at the bifurcation point μ_c. Figures 9(b) and 9(c) show, respectively, for the T-cell network, the relationship between τ_m and μ_n when controlling the strength of the activation edge from node "S1P" to node "PDGFR", and that of the inhibitory edge from node "DISC" to node "MCL1" [cf., Fig. 8(a), the nodes denoted as black circles and connected by bold coupling edges]. The critical value μ_c (indicated by the dotted line) can be estimated accordingly. The insets of (b) and (c) show the corresponding plots of the relationships on a double logarithmic scale, with the horizontal axis to be $\Delta_\mathrm{e} = \mu_\mathrm{c} - \mu_\mathrm{n}$, the *exceeded* value of μ_n over the critical point μ_c. We observe the following power-law scaling behavior:

$$\tau_\mathrm{m} = \alpha|\mu_\mathrm{n} - \mu_\mathrm{c}|^\beta \equiv \alpha|\Delta_\mathrm{e}|^\beta, \tag{2.2}$$

where β is the scaling exponent. The upper right region in the plane of the control parameters over the curve of $\tau_\mathrm{m}(\Delta_\mathrm{e})$, i.e., the region with larger Δ_e value or longer duration τ, corresponds to the case where control is successful in the sense that the system can definitely be driven to the desired final state.

The power-law scaling relation for τ_m demonstrated in Figs. 9(b) and 9(c) for the T-cell network is quite general, as it also holds for two-node and three-node GRNs (see **Methods**). For the T-cell system, the critical values of parameters for all the possible controllable edges from $\mathbf{C}_1$ or $\mathbf{C}_2$ to $\mathbf{N}$, and the corresponding values of α and β in Eq. (2.2) are provided in Supplementary Table 1 and

Supplementary Note 1. The control magnitude and time for some parameters are identical, for the reason that the logic relationship from the corresponding edges to the same node can be described as "AND" (c.f., Fig. 8) so that in the continuous-time differential equation model, all these in-edges are equivalent. (The control results for the two-node and three-node GRNs between any pair of nearest-neighbor attractors are listed in Supplementary Tables 2 and 3 respectively.) Due to the flexibility in choosing the control signal, our control scheme based on the attractor network is amenable to experimental implementation. We can assign weights to the shortest paths in the attractor network. For example, if we assume all the links are equally implementable, from Supplementary Table 1, the path from the $\mathbf{C}$ state to the $\mathbf{N}$ state that involve any one of IL2RB, STAT3, NFkB, PI3K or Apoptosis to MCL1 has a relatively larger weight, representing the relatively more efficient control protocol as the required parameter change Δ_{e} can be minimized.

2.2.4. Beneficial Role of Noise in Control.

More than three decades of intense research in nonlinear dynamical systems has led to great knowledge about the role of noise, in terms of phenomena such as stochastic resonance [73, 74], coherence resonance [75, 76], noise-induced chaos [50] and noise-induced state transitions [77]. Common to all these phenomena is that a proper amount of noise can in fact be beneficial, for example, to optimize the signal-to-noise ratio, to enhance the signal regularity or temporal coherence, or to facilitate the transitions among the attractors. This can be understood intuitively by noting that our control mechanism is to make the system leave an undesired attractor and approach a desired one but noise in combination with parameter adjustments can facilitate the process of escaping from an attractor. To demonstrate this, we assume that the T-Cell network is subject to Gaussian noise, which can be modeled by adding independent normal distribution terms $\mathbf{N}(0, \sigma^2)$ to the system equations, where σ is the noise amplitude. We find that, with noise, the required magnitude of pa-

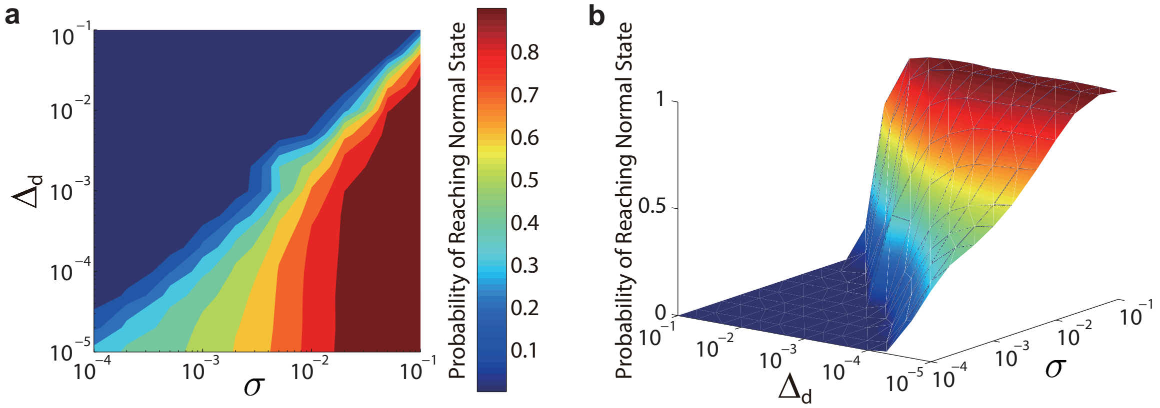

Fig. 10. The benefit of noise in controlling the T-cell network. (a) Success rate to control the T-cell network from the cancerous state $\mathbf{C}_1$ to the normal state $\mathbf{N}$ using a combination of parameter perturbation and external noise (of amplitude) σ, where $\Delta_\mathrm{d} \equiv \mu_\mathrm{n} - \mu_\mathrm{c}$ is the parameter deficiency. Warm colors indicate higher probability values of successful control. The perturbation duration is $\tau = 200$. The results are averaged over 1000 realizations. (b) A three-dimensional plot: success rate versus Δ_d and σ.

rameter change can be reduced. In fact, even when the controlled parameter $\mu_{\rm n}$ has not yet reached the bifurcation point $\mu_{\rm c}$, noise can lead to a finite probability for the system to escape the basin of the undesired attractor. We note that, in a recent work on stochastic control [77], a method was presented to switch the dynamical states. In a real experimental setting, there can be different sources of noise such as temperature and metabolic burden. In our parametric control method, the control signals are flexible with adjustable duration and amplitude, and noise can enhance the flexibility.

Suppose the control parameter is set to the value μ_n, which is insufficient to induce escape from the undesired attractor in the absence of noise. When noise is present, the system dynamics is stochastic. To characterize the control performance, we use a large number of independent realizations with the same initial condition. Specifically, we perform independent simulations starting from one cancerous state, e.g., $\mathbf{C}_1$, but with insufficient control strength as characterized by the deficiency parameter $\Delta_{\rm d} \equiv \mu_{\rm n} - \mu_{\rm c}$, and calculate the probability P of control success through the number of trials that the system can be successfully driven to the normal state $\mathbf{N}$. Figure 10(a) shows, on a double logarithmic scale, the values of P in the parameter plane of σ and $\Delta_{\rm d}$, where the control parameter is the strength of the activation edge from node “S1P” to node “PDGFR” in the T-cell network. A three-dimensional plot of P versus σ and $\Delta_{\rm d}$ is shown in Fig. 10(b). We see that, for fixed σ, P decreases with $\Delta_{\rm d}$ but, for any fixed value of $\Delta_{\rm d}$, the probability P increases with σ, indicating the beneficial role of noise in facilitating control. In the parameter plane there exists a well-defined boundary, below which the control probability assumes large values but above which the probability is near zero. Testing alternative control parameters yields essentially the same results, due to the simplicity of the attractor network for the T-cell system and the multiple directed edges from each cancerous state to the normal state.

2.3. Conclusion

The field of controlling chaos in nonlinear dynamical systems has been active for more than two decades since the seminal work of Ott, Grebogi, and Yorke [78]. The basic idea was that chaos, while signifying random or irregular behavior, possesses an intrinsically sensitive dependence on initial conditions that can be exploited for controlling the system using only small perturbation. This feature, in combination with the fact that a chaotic system possesses an infinite set of unstable periodic orbits, each leading to different system performance, implies that a chaotic system can be stabilized about some desired state with optimal performance. Controlling chaos has since been studied extensively and examples of successful experimental implementation abound in physical, chemical, biological, and engineering systems [79]. The vast literature on controlling chaos, however, has been mostly limited to low-dimensional systems, systems that possess one or a very few unstable directions (i.e., one or a very few positive Lyapunov exponents [80]). Complex networks with nonlinear dynamics are generally high dimensional, rendering inapplicable existing methodologies of chaos control. While mathematical frameworks of controllability of complex networks [4, 10] were developed and extensively studied recently, the limitation of such rigorous mathematical frameworks is that the nodal dynamical processes must be assumed to be linear.

Controlling nonlinear dynamics on complex networks remains to be an outstanding and challenging problem, especially in terms of the two key issues: controllability and actual control. To assess the controllability of nonlinear dynamical networks, drastically different approaches than the linear controllability framework are needed. While there were previous works on specific control methods such as pinning control [41, 81] and brute-force control that rely on altering the state variables of the underlying system (which in realistic situations can be difficult to implement), we continue to lack a general framework for actual control of complex networks with nonlinear dynamics through realistic, physical means. The main difficulty lies in the extremely diverse nonlinear dynamical behaviors that a network can generate, making it practically impossible to develop a general mathematical framework for control. In particular, the traditional control theoretical tools for linear dynamical systems aim to control the detailed states of all of the variables, which is in fact an overkill for most systems. For nonlinear dynamical networks, a physically meaningful approach may not require detailed control of all state variables. With this relaxation of the control requirement, it may be possible to develop a framework of controllability and devise actual control strategies for nonlinear dynamical networks based on physical/experimental considerations.

A common feature of nonlinear dynamical systems is the emergence of a large number of distinct, coexisting attractors [50, 82]. Often the performance and functions of the system are determined by the particular attractor that the system has settled into, associated with which the detailed states of the dynamical variables are not relevant. The key is thus to develop control principles whereby we nudge a complex, nonlinear system from attractor to attractor through small perturbation to a set of physically or experimentally feasible parameters. The main message of this paper is that a controllability framework can be developed for nonlinear dynamical networks based on controlling attractors.

Generally, the reason for control is that the current system is likely to evolve into an undesired state (attractor) or the system is already in such a state, and one wishes to apply perturbation to bring the system out of the undesired state and steer it into a desired state. The first step is then to identify a final state or attractor of the system that leads to the desired performance. The next step is to choose a set of experimentally adjustable parameters and determine whether small perturbation to these parameters can bring the system to the desired attractor. That is, under physically realizable perturbation there should be a control path between the undesired and the desired attractors. The path can be directly from the former to the latter, or there can be intermediate attractors on the path. For example, due to the physical constraint on the control parameters and the ranges in which they can be meaningfully varied, one can drive the system into some intermediate attractors by perturbing one set of parameters, and then from these attractors to the final attractor by using a different set of parameter control. For a complex, nonlinear dynamical network, the number of coexisting attractors can be large. (See Supplementary Note 5 for a systematic method to find the attractors.) Given a set of system performance indicators, one can classify all the available attractors into three categories: the undesired, desired, and the intermediate. We say a nonlinear network is controllable if there is a control path from any undesired attractor to the desired attractor under finite parameter perturbation. Regarding each attractor as a node and the control paths as directed links or edges, we generate an attractor network whose properties determine the controllability of the original networked dynamical system. For example, the average path length from an undesired to a desired attractor and the "control energy" (or the amount of necessary parameter perturbation) can serve as quantitative measures to characterize the controllability of the original network. We demonstrate our idea of control and construction of attractor networks using realistic networks from systems and synthetic biology. We also find that noise can facilitate control of nonlinear dynamical networks, and we provide a physical theory to understand this phenomenon.

Our framework can be adopted to controlling nonlinear dynamical networks other than the GRNs. For example, for the Northern European power grid network recently studied by Menck et al. [83], a rewiring method was proposed and demonstrated to be able to enhance the system stability through the addition of extra transmission lines. For a power grid network, the synchronous states are desired while other states, e.g., limit cycles, detrimental. Treating the link density (or number) as a tunable parameter, the minimum transfer capacity required for extra lines to realize the control can be estimated through our method. Another example is Boolean networks with discrete dynamics, for which Campbell and Albert proposed a perturbation method based on modification of update rules to rescue the system from the undesired states [84]. In terms of our method, an attractor network can be constructed based on perturbation to multiple parameters to drive the system out of the undesired, damaged states toward a normal (desired) state. For biological systems, Wang et al. proposed an epigenetic state network (ESN) approach [85] to analyze the transitions among different phenotypic processes. In an ESN, nodes represent attractors and edges represent pathways between a pair of attractors. By construction, different parameter values would result in a different ESN. (See Supplementary Note 6 and Supplementary Fig. 2 for an example of using the principle of attractor network to control a stochastic, biochemical reaction network.) In our attractor network, nodes are attractors but edges are directed and represent controllable paths (through parameter perturbation) to drive the system from one attractor to another.

While we emphasize the need to focus on physically meaningful and experimentally accessible parameter perturbation, there can still be a large number of attractor networks depending on the choice of the parameters, making it difficult to formulate a rigorous mathematical framework. Moreover, since the attractor network is directed and typically does not have an all-to-all coupling configuration, multiple parameter perturbation may be needed to realize control (e.g., as demonstrated using our three-node system), rendering the amount of computation prohibitive for relatively large dynamical networks. Successfully addressing these issues will ultimately enable us to achieve the grand goal of controlling nonlinear dynamical networks.

2.4. Methods

2.4.1. Construction of Attractor Networks.

For a system with known attractor basins and given initial and final states, the attractor network can be constructed through the following steps.

(1) Find all the parameters that can be adjusted externally and determine the possible range of variation of each tunable parameter based on experimental considerations and computational efficiency. For example, the T-cell network has 195 tunable parameters. Using the differential equation model one can test each parameter separately to determine its range of variation that can drive the system from one attractor to another. (Testing different parameter combinations is computationally prohibitive.)

(2) For a tunable parameter, choose a small set of values in its variable range, which include its original or nominal value.

(3) Simulate the system dynamics for each parameter value, starting from the initial attractor and determine the final attractor. Record the parameter values that can drive the system into the basin of the desired attractor. For example, for the T-cell network, parameter variations lead to saddle-node bifurcations, rendering applicable a straightforward *bisecting* algorithm to reduce the computational complexity in searching for the set of parameter values that result in a desired attractor.

(4) An attractor network can be constructed after all tunable parameters have been tested, from which distinct control paths can be identified for any given pair of initial and final attractors. (For the systems treated in this paper, the computational time required to construct the attractor network is listed in Supplementary Table 4.)

For systems whose attractors are unknown *a priori*, it is necessary to execute an attractor finding algorithm before an attractor network can be reconstructed. An example of such an algorithm is presented in Supplementary Note 5. The issues of multiple parameter based control and computational cost are discussed in Supplementary Notes 7 and 8 respectively.

2.4.2. Bifurcation Diagram and Continuation Algorithm.

Bifurcation diagram is a visualized method to characterize a system's steady state behavior with respect to parameter variation. In this paper, we used the *MATCONT* package in MATLAB to draw the bifurcation diagrams [86]. The bifurcation curves in MATCONT are computed based on the numerical continuation algorithm with a predictor-corrector procedure to enhance the stability and reduce the computational time. For the two-node GRN example, we calculate the bifurcation diagrams with respect to all 4 tunable parameters, based on which the attractor network can be constructed.

2.4.3. Attractor Network for a GRN of Two Nodes.

In spite of the simplicity of its attractor network, the original T-cell network itself is still quite complicated from the point of view of nonlinear dynamical analysis. To have a better understanding of our control mechanism, we study GRNs of relatively low dimensions and carry out a detailed analysis of the associated attractor networks.

We use a two-node GRN to understand the dynamical underpinning of the attractor network. As shown in Fig. 11(a), the network contains two auto-activation nodes (genes) and together they form a mutual inhibitory circuit. Such a topology was shown to be responsible for the regulation of blood stem cell differentiation [87]. In addition, it is conceivable that such topologies can be constructed with tunable inputs using synthetic biology approaches [64].

In a typical experimental setting, four coupling parameters can be adjusted externally through the application of repressive or inductive drugs. To demonstrate attractor network and control implementation, we consider the parameter regime in which the system has four stable steady states

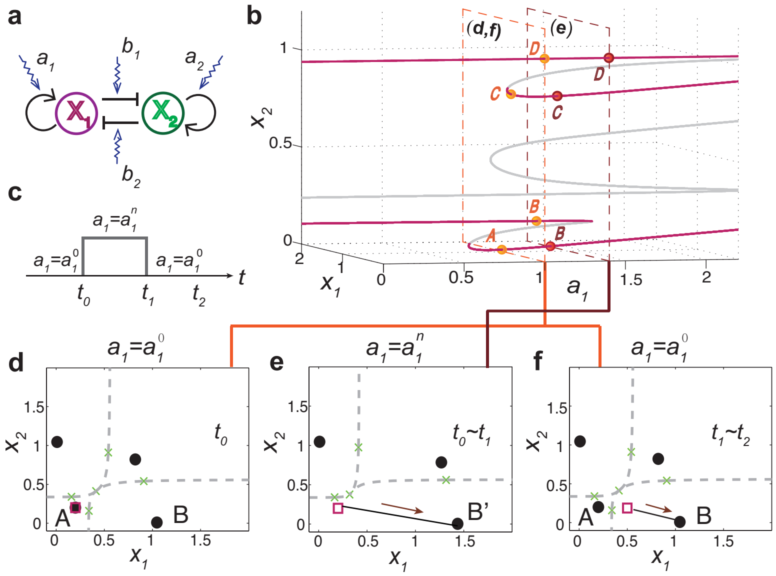

Fig. 11. Control of a GRN of two nodes. (a) Simplified model of the two-node GRN, where the arrowhead and bar-head edges represent activation and inhibition regulations, respectively, and the sawtooth lines denote the strength of the tunable edge. (b) Bifurcation diagram with respect to the control parameter a_1, where the red and gray solid lines denote the stable and unstable steady states, respectively. In the two parallel cross-sections (with dashed line boundaries) for $a_1 = a_1^0$ and $a_1 = a_1^n$, the yellow and brown dots represent the corresponding stable attractors, respectively. (c) Control signals required to drive the system from attractor $\mathbf{A}$ to attractor $\mathbf{B}$. In (d-f), gray dashed lines represent the basin boundaries; black solid circles and green crosses denote attractors and unstable steady states, respectively. (d) For the initial parameter setting, $a_1 = a_1^0$, the system is at a low concentration state $\mathbf{A}$, and the target state is $\mathbf{B}$. (e) By changing a_1 from a_1^0 to a_1^n, attractor $\mathbf{A}$ is destabilized and its original basin is absorbed into that of the intermediate attractor $\mathbf{B}'$, so the system approaches $\mathbf{B}'$. (f) When control perturbation upon a_1 is released, the landscape recovers to that in (d). Once the system has entered the basin of the target state $\mathbf{B}$ during the process in (e), it will evolve spontaneously towards $\mathbf{B}$. Parameters in simulation are $a_1^0 = 1.0$, $a_1^n = 1.4$, $t_0 = 0$, $t_1 = 23$, and $t_2 = 40$.

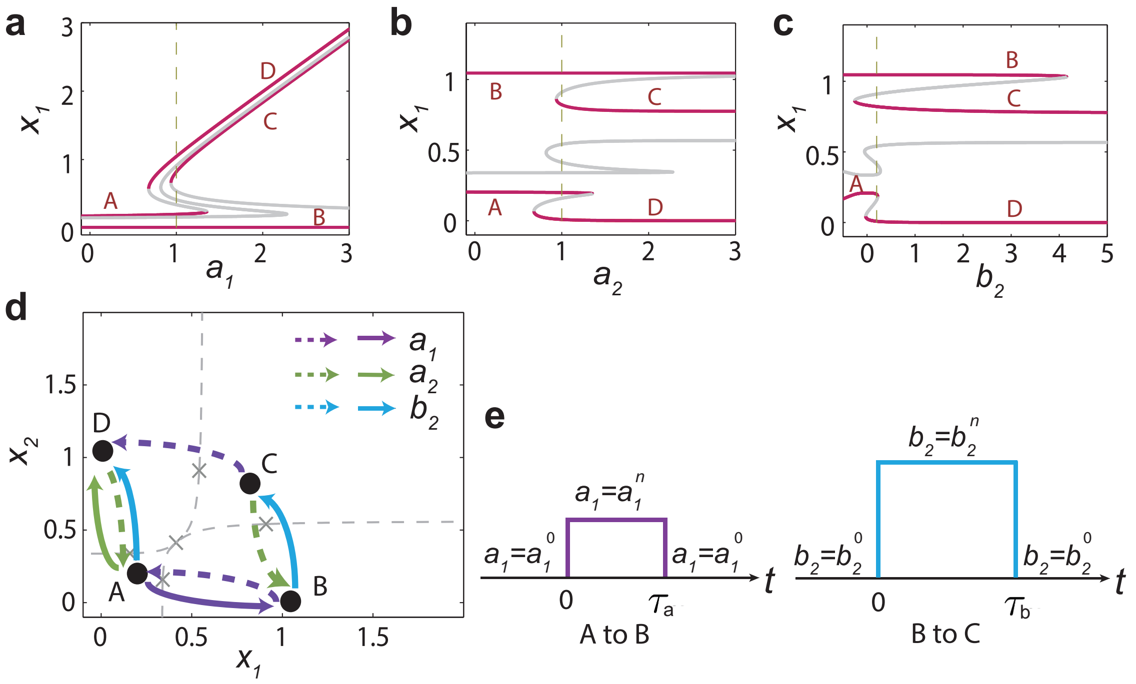

Fig. 12. Attractor network construction for a GRN of two nodes. (a-c) Bifurcation diagrams with respect to the coupling parameters a_1, a_2 and b_2, respectively, where each bifurcation point can be exploited to design control. (d) The corresponding attractor network, in which a directed edge corresponds to an elementary control that is designed to steer the system from the original attractor to the directed one. The solid and dashed edges, respectively, denote the positive and negative changes in the corresponding control parameters. (e) Sequential control signals required to drive the system from attractor **A** to attractor **C** through the path **A** $\rightarrow$ **B** $\rightarrow$ **C**. In simulation, the original parameter values are $a_1^0 = 1.0$ and $b_2^0 = 0.2$. We set $a_1^n = 1.4$, followed by setting $b_2^n = 4.2$, and the respective durations of the parameter perturbation are $\tau_a = 23$ and $\tau_b = 32$.

(attractors) that correspond to four different cell states during cell development and differentiation. In particular, the dynamical network can be mathematically described as,

$$\begin{aligned} \dot{x_1} &= a_1 \cdot \frac{x_1^n}{s^n + x_1^n} + b_1 \cdot \frac{s^n}{s^n + x_2^n} - k \cdot x_1, \\ \dot{x_2} &= a_2 \cdot \frac{x_2^n}{s^n + x_2^n} + b_2 \cdot \frac{s^n}{s^n + x_1^n} - k \cdot x_2, \end{aligned} \tag{2.3}$$

where the dynamical variables (x_1, x_2) characterize the protein abundances of the gene products, k denotes the degradation rate of each gene, and the tunable parameters a_1, a_2, b_1, and b_2 represent the strengths of auto or mutual regulations. In a GRN, the dynamical behaviors of inhibition and activation are captured by the Hill function: $f(x) = x^n/(x^n + s^n)$ for activation and $f(x) = s^n/(x^n + s^n)$ for inhibition, where the parameter s characterizes half activation (or inhibition) concentration (for $x = s$, the output is 0.5), and n quantifies the correlation between the input and output concentrations, with a larger value of n corresponding to a stronger inhibition or activation effect. For any specific GRN, the values of both s and n can be determined experimentally. For simplicity, we assume the system to be symmetric in that inhibition and activation share the same Hill function (i.e., with the same parameters s and n). To have four attractors, we set the auto activation strengths, a_1 and a_2, to 1.0, and mutual inhibition strengths, b_1 and b_2, to 0.2. The value of the degradation rate k is set to 1.1, taking into account the effects of protein degradation and cell volume expansion.

Figures 11(b-f) show a particular process of controlling the system from an initial state, denoted as $\mathbf{A}$, in which both x_1 and x_2 have low abundance, to a final state $\mathbf{B}$ where x_1 and x_2 have high and low abundance, respectively. From the bifurcation diagram [Fig. 11(b)] with respect to the control parameter a_1, we see that, as a_1 is increased from 1.0 to 1.4, in the lower branch, the initial attractor $\mathbf{A}$ is destabilized through a saddle-node bifurcation. The control signal is shown in Fig. 11(c), where the original and perturbed parameter values are denoted as a_1^0 and a_1^n, respectively. The bifurcation based control process is shown in Figs. 11(d-f), where panel (d) exhibits the phase space of the system prior to control ($a_1 = 1.0$). When control is activated so that a_1 is set to $a_1 = 1.4$, the original basin of attractor $\mathbf{A}$ merges into the basin of an intermediate attractor $\mathbf{B}'$, and the system originally in $\mathbf{A}$ starts to migrate towards the intermediate attractor $\mathbf{B}'$, as indicated by the arrowed trajectory in panel (e). Control perturbation upon a_1 can be withdrawn once the system enters the region belonging to the original basin of the target attractor $\mathbf{B}$, after which the system spontaneously evolves into $\mathbf{B}$ for $a_1 = 1.0$, as shown in Fig. 11(f).

To obtain a global picture of all possible control outcomes, we construct the attractor network for the two-node GRN system, assuming that three parameters: a_1, a_2 and b_2, are available for control. The corresponding bifurcation diagrams are shown in Figs. 12(a-c), from which all saddle-node bifurcations can be identified for control design. When all the attractors are connected with directed and weighted edges through the control processes, i.e., when none of the attractor is isolated, we obtain an attractor network, as shown in Fig. 12(d). Specifically, the edge weight can be assigned by taking into account the key characteristics of control such as the critical parameter strength $\mu_{\rm c}$ and the power-law scaling behavior of the required minimum control time $\tau_{\rm m}$ (see Supplementary Table 2). From the attractor network, we can find all possible control paths for any given pair of original and desired states.

From Fig. 12(d), we see that the two-node GRN system is *fully controllable* since any of the coexisting attractors is reachable by applying proper sequential controls to the available parameters. The concept of attractor network is appealing because it provides a clear control scenario to drive the system from any initial attractor to any desired attractor. In fact, the attractor network provides a blueprint that can be used to design a proper combination of parameter changes to induce the so-called synergistic or antagonistic effects [88]. For example, $\mathbf{A}$ is not directly connected with $\mathbf{C}$, neither is $\mathbf{B}$ directly connected to $\mathbf{D}$. However, the system can be steered from $\mathbf{A}$ to $\mathbf{B}$ through perturbation on a_1, and then from $\mathbf{B}$ to $\mathbf{C}$ through a change in b_2, as shown in Fig. 12(e). Another example to demonstrate the need of multiple parameter perturbation is to control the system from $\mathbf{B}$ to $\mathbf{D}$. A viable control path is $\mathbf{B} \to \mathbf{C} \to \mathbf{D}$, which can be realized through perturbation on parameters (b_2, a_1). We also see that the two $\mathbf{B} \to \mathbf{A} \to \mathbf{D}$ paths can be realized through parameter changes in (a_1, a_2) and (a_1, b_2), respectively. A phase diagram illustrating hoe different choices of the parameters affect the final attractor is provided in Supplementary Note 2 and Supplementary Fig. 1.

When multiple control paths exist from an initial attractor to a final one, a practical issue is to identify the optimal path that is cost effective and robust. The concept of *weighted-shortest path* can be used to address this issue. Particularly, the weights of edges can be determined from experimental considerations such as the cost, limitation in drug dose, the control duration time, etc.

2.4.4. Potential Landscape and Noise in Nonlinear Control.

The role of noise in facilitating control of a nonlinear dynamical network can be understood using the concept of *potential landscape* [89–91] or Waddington landscape [92] in systems biology, which essentially determines the biological paths for cell development and differentiation [93, 94]. The potential landscape was used to manipulate time scales to control stochastic and induced switching in biophysical networks [77, 94]. Intuitively, the power of the concept of the landscape can be understood by resorting to the elementary physical picture of a ball moving in a valley under gravity. The valley corresponds to one stable attractor. To the right of the valley there is a hill, or a potential barrier in the language of classical mechanics. The downhill side to the right of the barrier corresponds to a different attractor. Suppose the confinement of ball's motion within the valley is undesired and one wishes to push the ball over the barrier to the right attractor (desired).

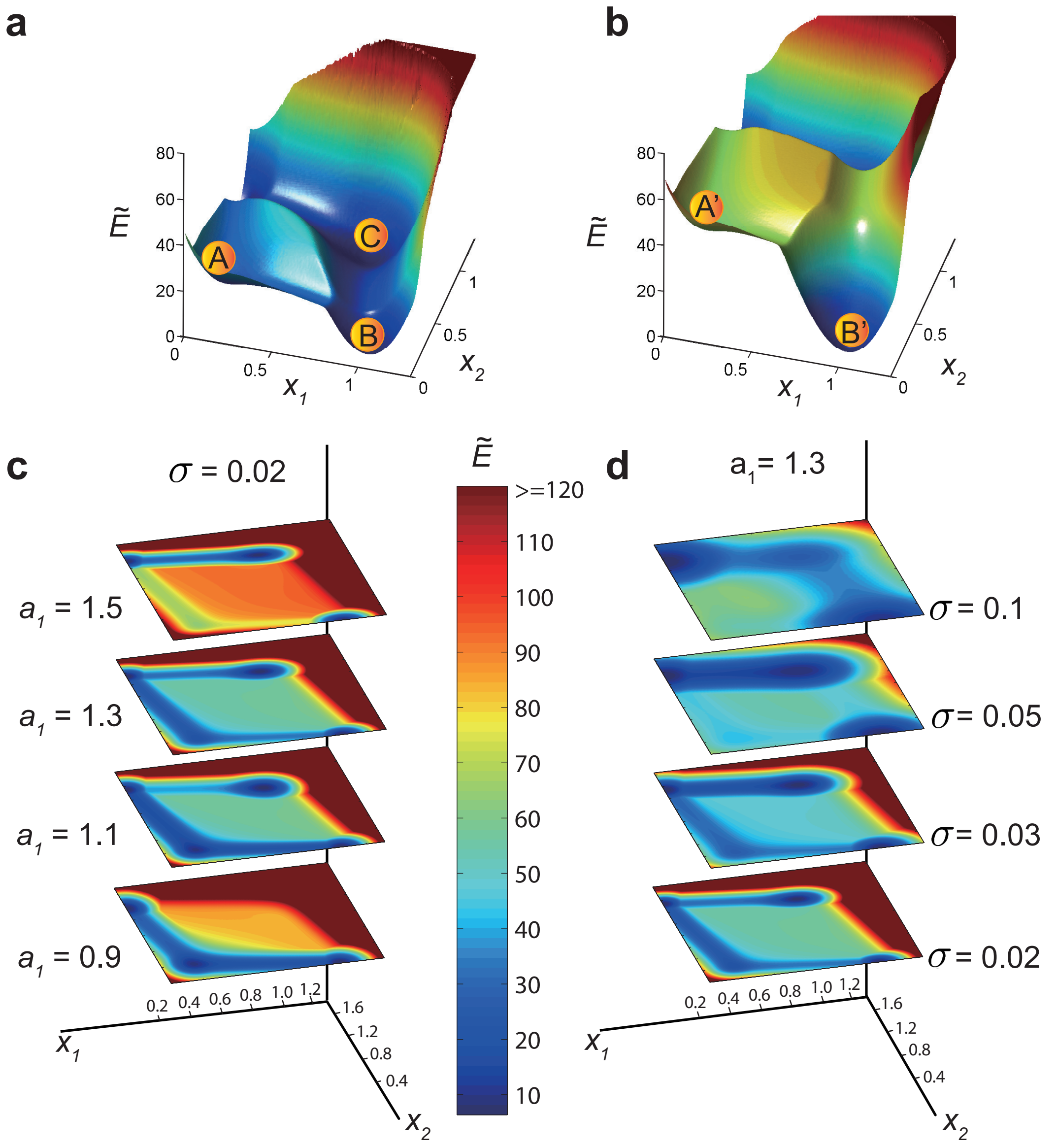

Fig. 13. Illustration of pseudo potential landscape. "Pseudo" potential $\tilde{E}$ of the two-node GRN system (**a**) for $a_1 = 1.0$ ($\Delta_{\mathrm{d}} \approx 0.3549$), $\sigma = 0.05$ and (**b**) for $a_1 = 1.3$ ($\Delta_{\mathrm{d}} \approx 0.0549$), $\sigma = 0.05$. Regions of warm and cold colors indicate the states with large and small pseudo energies, respectively. (**c**) For fixed $\sigma = 0.02$, two-dimensional representation of $\tilde{E}$ for a number of values of a_1. (**d**) For fixed $a_1 = 1.3$, two-dimensional representation of $\tilde{E}$ for a number of values of σ.

If the barrier is large, there will be little probability for the ball to move across the top of the barrier towards the desired attractor. In this case, a small amount of noise is unable to enhance the crossover probability. However, if the barrier height is small, a small amount of noise can push the ball over to desired attractor on the right side of the barrier. Thus, the beneficial role of noise is more pronounced for small height of the potential barrier, a behavior that we observe when controlling the T-cell network (Fig. 10). In mechanics, the system can be formulated using a potential function so that, mathematically, the motion of the ball can be described by the Langevin equation, which has been a paradigmatic model to understand nonlinear phenomena such as stochastic resonance [73, 95, 96]. In the past few years, a quantitative approach has been developed to map out the potential landscape for gene circuits or GRNs [89, 97, 98]. In nonlinear dynamical systems, a similar concept exists - *quasipotential* [99–101], which plays an important role in understanding phenomena such as noise-induced chaos.

For an attractor network, in the presence of noise each node corresponds to a potential valley of certain depth that characterizes the stability of the attractor. For a fixed depth, noise of larger amplitude σ leads a higher escaping probability or shorter escaping time. When the amplitude of the control signal is not sufficient to drive the system across the local potential barrier, noise can facilitate control by pushing the system out of the undesired valley (attractor).

The potential landscape for a GRN under Gaussian noise can be constructed from the dynamical equations of the system using the concept of "pseudo" energy [91] (see **Methods**). For the two-node GRN system [Eq. (2.3)] subject to stochastic disturbance $N(0, \sigma^2)$, we can compute the potential landscape for any combination of some system parameter (say a_1) and the noise amplitude σ. Figures 13(a) and 13(b) show two examples of the landscape (in three-dimensional representation) for $a_1 = 1.0$ and $a_1 = 1.3$, where the noise amplitude is $\sigma = 0.05$. Figures 13(c) shows, for $\sigma = 0.02$, a two-dimensional representation of the pseudo-energy for a number of values of a_1. We observe that, for a same noise amplitude, as a_1 is increased, the transition rate from $\mathbf{A}$ to $\mathbf{B}$ becomes higher (the color becomes warmer).

What if the system is at an attractor that is deep in its basin and not close to the boundary? Since our approach is based on parameter adjustment, such a case can still be effectively controlled in the sense that the system can be brought out of the attractor. For example, consider the attractor $\mathbf{C}$ for $a_1 = 1.5$ in the two-node GRN system, which is deep inside its own basin, as shown in Fig. 13(c). When parameter perturbation is applied to the system, its energy landscape and basin structure are changed (from top to bottom). Under control, the attractor "moves" towards the basin boundary and is destroyed when it reaches the boundary, thereby bringing the system out of this attractor. Another example is attractor $\mathbf{A}$ in Fig. 13(c), where it can be seen that, when the control parameter a_1 increases its value from 0.9 to 1.5, its basin changes and the attractor moves towards the boundary as well. Similar plots but for fixed $a_1 = 1.3$ and different values of σ are shown in Fig. 13(d). We see that, for example, for $a_1 = 1.0$, there are four valleys (attractors). For $a_1 = 1.3$, the pseudo energy for $\mathbf{A}$ (the original valley at the lower-left corner) becomes higher, and the path for the transition from $\mathbf{A}$ to $\mathbf{B}$ becomes more pronounced. Further increasing a_1 towards the critical value (about 1.35) raises the energy of $\mathbf{A}$ to the level of the potential barrier, effectively eliminating the corresponding valley and the attractor itself. Note that, for a fixed value of a_1, increasing noise amplitude can lead to a mixture of cold colors, meaning that the valley range becomes wider and the ridge between two adjacent valleys becomes shallower, resulting in a higher transition probability for each attractor.

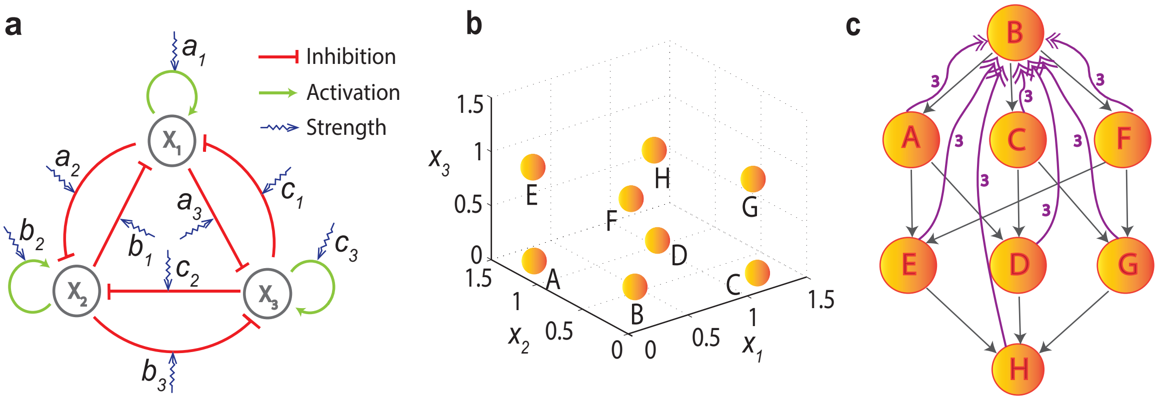

Fig. 14. A GRN of three nodes and its attractor network. (a) Schematic illustration of a three-node GRN system. The arrowhead and bar-head edges represent activation and inhibitory regulations, respectively. The sawtooth lines specify that the corresponding edge strength is experimentally adjustable. (b) Coexisting attractors (**A** to **H**) in the phase space. (c) The underlying attractor network, where each node represents an attractor and each weighted directed link indicates that its strength can be experimentally tuned to steer the system from the starting attractor to the pointed attractor. Each grey directed link with a single arrow indicates that only one parameter is needed to achieve control, and each purple link with a double-arrow and the label 3 represent the case where three parameters are required to achieve control.

2.4.5. Attractor Network for a Three-Node GRN.

We also study a three-node GRN system, as shown in Fig. 14(a). Similar to the two-node GRN system, there exist both auto and mutual regulations among the nodes. All the interactions are assumed to be characterized by the same parameters, s and n, in the Hill function. The nonlinear dynamical equations of the system are [61, 102]

$$\begin{aligned}
\dot{x_1} &= a_1 \cdot \frac{x_1^n}{s^n + x_1^n} + b_1 \cdot \frac{s^n}{s^n + x_2^n} + c_1 \cdot \frac{s^n}{s^n + x_3^n} - k \cdot x_1, \\
\dot{x_2} &= a_2 \cdot \frac{s^n}{s^n + x_1^n} + b_2 \cdot \frac{x_2^n}{s^n + x_2^n} + c_2 \cdot \frac{s^n}{s^n + x_3^n} - k \cdot x_2, \\
\dot{x_3} &= a_3 \cdot \frac{s^n}{s^n + x_1^n} + b_3 \cdot \frac{s^n}{s^n + x_2^n} + c_3 \cdot \frac{x_3^n}{s^n + x_3^n} - k \cdot x_3,
\end{aligned} \tag{2.4}$$

where the state variables (x_1, x_2 and x_3) represent the abundances of the three genes products, the auto-activation parameters a_1, b_2, c_3 and the mutual-inhibition parameters a_2, a_3, b_1, b_3, c_1, c_2 are all experimentally accessible. To be concrete, initially all the auto activation and mutual inhibition parameters are set to be 1.0 and 0.1, respectively, and k (the degradation rate) can be conveniently set to unity. The parameters in the Hill function are $n = 4$ and $s = 0.5$. there are altogether eight attractors in this system, as shown in Fig. 14(b), which are distributed symmetrically in the three-dimensional state space. For example, attractor $\mathbf{H}$ has relatively high values for all three dynamical variables, and attractor $\mathbf{B}$ exhibits the opposite case with low abundances. For attractors $\mathbf{A}$, $\mathbf{C}$ and $\mathbf{F}$, one of the three state variables is high and the other two are low. For attractors $\mathbf{D}$, $\mathbf{E}$ and $\mathbf{G}$, one of the three state variables is low but the other two are high.

From numerical simulations, we find that the features of control are essentially the same as those for the two-node GRN system, in terms of characteristics such as the existence of critical control strength and the power-law scaling behavior of the minimum control time (see Supplementary Table 3, Supplementary Notes 3 and 4). We construct the attractor network in Fig. 14(c) through combinations of all eight attractors (as nodes) and directed elementary controls (as weighted directed edges). Information in Supplementary Table 3 can also be used to estimate the respective weights of the edges. From the attractor network, for any given pair of initial and final states, we can identify all the viable control paths. Furthermore, the *weighted-shortest path* can be calculated once the edge weights are determined.

We note that, typically, the attractor network based on elementary control is not an all-to-all directed network so that certain control paths are absent, e.g., from attractor $\mathbf{H}$ to $\mathbf{B}$. Therefore, we need to extend the control method to a combination of multiple parameters. From Fig. 14(c), we note that attractor $\mathbf{H}$ has incoming links only while $\mathbf{B}$ has outgoing links only. The structure of the attractor network thus indicates that full control can be achieved (i.e., to drive the system from any initial attractor to any final attractor) if we can build a directed path from $\mathbf{H}$ to $\mathbf{B}$. Since attractors $\mathbf{B}$ and $\mathbf{H}$ have low and high abundance, respectively, in the phase space, we modify the three auto-activation parameters simultaneously to steel the system from $\mathbf{H}$ to $\mathbf{B}$. We find that the relationship between control strength and minimal control time also follows the power law scaling with $\mu_c \approx 0.7973$, $\alpha \approx 1.26$, and $\beta \approx -0.77$. In fact, when all the auto-activation strengths are smaller than μ_c, the system has one attractor only: $\mathbf{B}$, meaning that perturbation based on parameter combinations can be used to realize the control from other attractors as well, i.e., from one of the attractors $\mathbf{A}$, $\mathbf{C}$, $\mathbf{D}$, $\mathbf{E}$, $\mathbf{F}$, and $\mathbf{G}$ to attractor $\mathbf{B}$.

2.4.6. Construction of Pseudo Potential Landscape.

For a dissipative, nonlinear dynamical system subject to noise, we can construct a pseudo potential landscape based on the state probability distribution. Assume that, asymptotically, the system approaches a stationary distribution. For a canonical dynamical system, the potential can be defined as $E(\mathbf{x}) = -\log P(\mathbf{x})$, where $P(\mathbf{x})$ is the probability density function. For a conservative dynamical system, the direction of system evolution is nothing but the direction of the gradient of the potential function. However, this does not hold for dissipative dynamical systems. The potential function thus does not have the same physical meaning as that for a conservative system, henceforth the term pseudo potential. This approach can be adopted to GRNs.

To obtain the stationary distribution, we use the modified weighted-ensemble algorithm proposed by Kromer et al. [91], which offers faster convergence than, for example, the traditional random walk method. To be illustrative, we take the two-node GRN system [Eq. (2.3)] as an example to demonstrate how the pseudo potential landscape can be numerically constructed. The state space of the two-dimensional dynamical system is partitioned into an $M \times M$ lattice with reflective boundaries conditions. Initially the probability $P_{m,n}(t)$ of all gird points are set to be uniform. The simulation time is divided into T steps, where each step has the duration Δt. At the beginning of each step t, there are N walkers randomly distributed at the grid point (m, n), which carry equal weight $P_{m,n}(t)/N$ and perform random walk under the system dynamics and noise. The locations of these walkers in the grid are recorded at the end of each time step, and the probability at the next time step, $P_{m,n}(t+1)$, is the summation of the probabilities carried by all the walkers at time t. At time $(t+1)$, N new walkers carrying the updated probability at each grid point perform random walk again on the grid. This procedure repeats until the probability distribution becomes stationary, say $P_{m,n}$, which gives the pseudo potential landscape as $\tilde{E}(m,n) = -\log P_{m,n}$. Numerically, the time evolution of all walkers can be simulated using the second-order Heun method for integrating stochastic differential equations. For Fig. 13, the state space is divided into a 500×500 grid. At each grid point there are $N = 20$ walkers, each evolving $T = 2000$ time steps with $\Delta t = 10^{-4}$.

Instead of calculating the stationary probability distribution density, an alternative approach to constructing the potential landscape is the Freidlin and Wentzel's large deviation theory [103]. According to this theory, first, one maps the stochastic dissipative system of interest to a Hamiltonian system [104]. Then, using the Freidlin and Wentzel theory [103], one can estimate the transition rate from an attractor to a saddle point as $r \sim \exp(-S_0/\sigma)$, where σ is the noise amplitude and $S_0(\cdot)$ characterizes the action functional associated with the optimal energy path, which can be numerically solved through an unconstrained nonlinear optimization method [85, 89]. Since this theory relies on solving a nonlinear optimization problem, in order to visualize the energy landscape, it is necessary to use a large number of state values $\mathbf{x}$ and solve the optimization problem for each, which is computationally exhaustive. We find that, to capture the essential features of the energy landscape, it suffices to use the stationary distribution method.

In the small noise limit $\sigma \to 0$, according to the theory of Freidlin and Wentzell [85, 103], to the leading order the transition rate r from one fixed point in a nearby saddle point can be approximated as

$$r \sim \exp\left[(-S_0(\mathbf{x}_{\mathrm{sp}})\right],$$

where $S_0(\mathbf{x})$ characterizes the action function of the optimal energy path ending at state $\mathbf{x}$ and can be numerically solved through an unconstrained nonlinear optimization method, and $\mathbf{x}_{\mathrm{sp}}$ denotes the saddle point. The minimum control time satisfies $\tau_{\mathrm{m}} \sim r^{-1}$, so we have $\tau_{\mathrm{m}} \sim \exp\left[S_0(\mathbf{x}_{\mathrm{sp}})\right]$. From Eq. (2.2) we obtain

$$\Delta_{\mathrm{e}} \sim \exp(S_0(\mathbf{x}_{\mathrm{sp}})/\beta),$$

indicating that the exceeded value Δ_{e} of the control parameter μ is exponentially related to the optimal energy S_0 between the initial state and the nearby saddle point in the potential landscape.

2.5. Supplementary Information

2.5.1. Supplementary Tables

TABLE 1: Edge control in the T-cell system. The first and the second columns, respectively, give the executor and the receiver of the coupling edges in the T-cell system. For control associated with each edge, the minimum control time τ_m exhibits a power-law scaling behavior: $\tau_\mathrm{m} = \alpha \cdot |\mu_\mathrm{c} - \mu_\mathrm{n}|^\beta$, where μ_c is the critical coupling strength (the third column). The fourth and the fifth columns list the scaling parameters α and β obtained by least squares fitting, with mean squared error (MSE) given in the sixth column. Note that Apoptosis represents the outcome of cellular signaling and it has inhibitory regulations to all the other nodes in the network. If Apoptosis is activated, the system will reach the desired normal state. Because of this the node Apoptosis appears in every row of the first column.

From	To	μ_c	α	β	MSE
S1P or PDGF or Apoptosis	PDGFR	0.5210	1.9921	−0.4360	0.0070
GRB2 or PDGFR or GAP or Apoptosis	RAS	0.5329	1.5664	−0.4892	0.0052
IL2RA or IL2RB or RANRES or IFENG or SOCS or CD45 or Apoptosis	JAK	0.5408	1.5619	−0.5154	0.0272
PDGFR or Apoptosis	SPHK1	0.5496	1.7948	−0.4904	0.0001
SPHK1 or Ceramide or Apoptosis	S1P	0.5697	1.7324	−0.5509	0.0008
RAS or Apoptosis	MEK	0.5805	1.5169	−0.5009	0.0111
JAK or Apoptosis	STAT3	0.5935	1.7482	−0.4587	0.0536
TPL2 or PI3K or FLIP or TRADD or IAP or Apoptosis	NFkB	0.6060	1.2286	−0.6366	0.0004
FDGFR or RAS or Apoptosis	PI3K	0.6187	1.3917	−0.5764	0.0786
MEK or PI3K or Apoptosis	ERK	0.6225	1.7762	−0.4363	0.0500

ERK or TBET or Apoptosis	IL2RBT	0.6412	1.7303	-0.4581	0.0285
IL2RBT or IL2 or IL15 or Apoptosis	IL2RB	0.6520	1.6082	-0.5078	0.0980
DISC or IL2RB or STAT3 or NFkB or PI3K or Apoptosis	MCL1	0.6596	1.5745	-0.5480	0.0510

TABLE 2: Controlling a two-node GRN system. For the two-node GRN system discussed in the main text, the underlying attractor network consists of four nodes, denoted as $\mathbf{A}$, $\mathbf{B}$, $\mathbf{C}$, and $\mathbf{D}$, respectively. The first column represents all possible elementary controls among the nodes in the attractor network. The second column shows the specific coupling parameter adjusted to realize the elementary control and the corresponding critical coupling strength. The remaining columns show the parameters α and β as well as the fitting error (MSE) in the power-law scaling of the minimum control time τ_{m}.

Elementary control	Critical coupling strength μ_c	α	β	MSE
$\mathbf{A}$ to $\mathbf{B}$	$a_1 = 1.3523$	2.7590	-0.6688	0.2148
$\mathbf{A}$ to $\mathbf{B}$	$b_1 = 0.2206$	0.1735	-0.9085	0.0014
$\mathbf{A}$ to $\mathbf{D}$	$a_2 = 1.3523$	2.7590	-0.6688	0.2148
$\mathbf{A}$ to $\mathbf{D}$	$b_2 = 0.2206$	0.1735	-0.9085	0.0014
$\mathbf{B}$ to $\mathbf{A}$	$a_1 = 0.6800$	2.0415	-0.5539	0.0990
$\mathbf{B}$ to $\mathbf{C}$	$b_2 = 4.1557$	5.9264	-0.5364	0.0646
$\mathbf{C}$ to $\mathbf{B}$	$a_2 = 0.9385$	0.7697	-0.6906	0.1870
$\mathbf{C}$ to $\mathbf{D}$	$a_1 = 0.9385$	0.7697	-0.6906	0.1870
$\mathbf{D}$ to $\mathbf{A}$	$a_2 = 0.6800$	2.0415	-0.5539	0.0990

D to **C**	$b_1 = 4.1557$	5.9264	-0.5364	0.0646

TABLE 3: Controlling a three-node GRN system. For the three-node GRN system in the main text, the underlying attractor network has eight nodes, denoted as $\mathbf{A}$, $\mathbf{B}$, …, and $\mathbf{H}$, respectively. The first column specifies all possible elementary controls among the nodes in the attractor network. The second column shows the specific coupling parameter that needs to be adjusted to realize the corresponding elementary control and the critical coupling strength. The remaining columns show the power-law scaling parameters α and β, as well as the fitting error MSE of the minimum control time τ_{m} associated with each elementary control.

Path	Critical coupling strength	α	β	MSE
A to **D**	$a_1 = 6.0540$	10.6386	-0.5326	0.5491
A to **D**	$b_1 = 2.7534$	6.1863	-0.5682	0.2130
A to **D**	$c_1 = 0.1872$	0.4634	-0.7315	0.0100
A to **E**	$a_3 = 0.1872$	0.4634	-0.7315	0.0100
A to **E**	$b_3 = 2.7534$	6.1863	-0.5682	0.2130
A to **E**	$c_3 = 6.0540$	10.6386	-0.5326	0.5491
B to **A**	$a_2 = 0.1011$	0.0487	-0.9492	0.0090
B to **A**	$b_2 = 1.0183$	1.0208	-0.8049	0.2461
B to **A**	$c_2 = 0.1011$	0.0487	-0.9492	0.0090
B to **C**	$a_1 = 1.0183$	1.0208	-0.8049	0.2461
B to **C**	$b_1 = 0.1011$	0.0487	-0.9492	0.0090
B to **C**	$c_1 = 0.1011$	0.0487	-0.9492	0.0090

B to **F**	$a_3 = 0.1011$	0.0487	-0.9492	0.0090
B to **F**	$b_3 = 0.1011$	0.0487	-0.9492	0.0090
B to **F**	$c_3 = 1.0183$	1.0208	-0.8049	0.2461
C to **D**	$a_2 = 2.7534$	6.1863	-0.5682	0.2130
C to **D**	$b_2 = 6.0540$	10.6386	-0.5326	0.5491
C to **D**	$c_2 = 0.1872$	0.4634	-0.7315	0.0100
C to **G**	$a_3 = 2.7534$	6.1863	-0.5682	0.2130
C to **G**	$b_3 = 0.1872$	0.4634	-0.7315	0.0100
C to **G**	$c_3 = 6.0540$	10.6386	-0.5326	0.5491
D to **H**	$a_3 = 3.8127$	6.4535	-0.5125	0.0142
D to **H**	$b_3 = 3.8127$	6.4535	-0.5125	0.0142
E to **H**	$b_1 = 3.8127$	6.4535	-0.5125	0.0142
E to **H**	$c_1 = 3.8127$	6.4535	-0.5125	0.0142
F to **E**	$a_2 = 0.1872$	0.4634	-0.7315	0.0100
F to **E**	$b_2 = 6.0540$	10.6386	-0.5326	0.5491
F to **E**	$c_2 = 2.7534$	6.1863	-0.56823	0.2130
F to **G**	$a_1 = 6.0540$	10.6386	-0.5326	0.5491
F to **G**	$b_1 = 0.1872$	0.4634	-0.7315	0.0100
F to **G**	$c_1 = 2.7534$	6.1863	-0.5682	0.2130
G to **H**	$a_2 = 3.8127$	6.4535	-0.5125	0.0142
G to **H**	$b_2 = 3.8127$	6.4535	-0.5125	0.0142

TABLE 4: Computational setting and cost for constructing the attractor networks. The first row specifies the systems. The second row shows the number of attractors in the system under the original parameter setting. The third row illustrates the method of calculation. The fourth row shows the number of coupling parameters tested. The fifth row shows the number of parameters that can be exploited to achieve control. The sixth row shows the computational time for each method. The software and computers for the T-cell simulation are MATLAB 2012a, 3.4GHz, Intel Core i7, Win7, while those for the two- and three-node GRNs calculations are: MATLAB 2015b, 2.9 GHz, Intel Core i7, OS X.

System	T-cell	Two-node GRN	Three-node GRN
Attractors	3	4	8
Calculation Methods	Bisection Search	Continuation	Continuation
Coupling Parameters	195	4	9
Control Parameters	48	4	9
Computation Time	4.61 hours	64.60 seconds	21.87 minutes

2.5.2. Supplementary Figures

2.5.3. Supplementary Note 1: Control of T-Cell System.

The success of our control scheme relies on one important condition: the underlying dynamical system is capable of responding to control perturbation in the sense that parameter perturbation can lead to dramatic changes in the system's attractors. A "rule of thumb" to determine if a dynamical system satisfies this condition can be, as follows. Given a computational model of the GRN to be controlled, we can increase the perturbation to an accessible control parameter (either activation or inhibition) to test if the corresponding attractor disappears. If it turns out impossible for the system

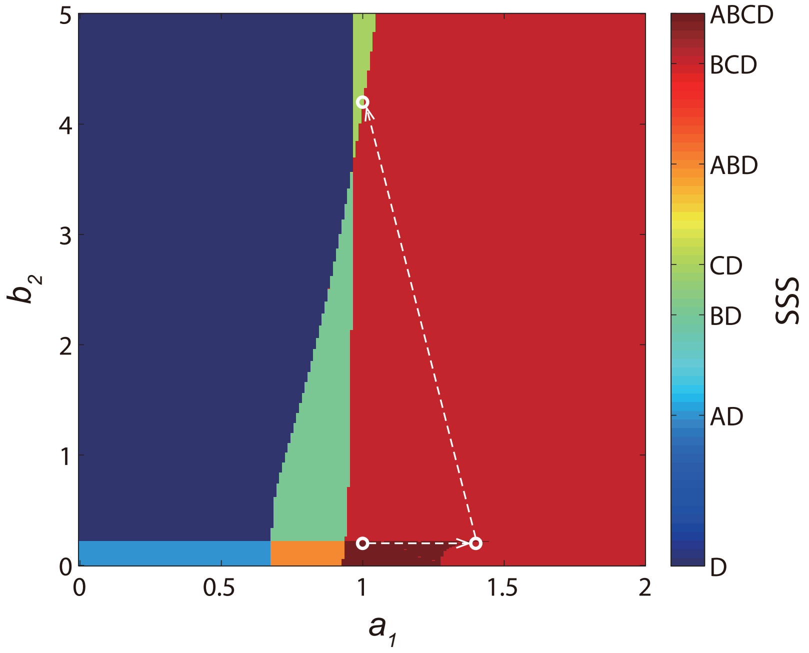

Fig. 15. Phase Diagram of two-node GRN system. For the two-node GRN system treated in the main text, final state of the system in the parameter plane (a_1, b_2), where each colored region represents a specific combination of attractors. Other parameters are set as $a_2 = 1.0$ and $b_1 = 0.2$. Each white circle represents a whole set of possible attractors in one system and white dash lines represent control procedures. The four-attractor state $\mathbf{ABCD}$ can be identified toward the bottom of the phase diagram.

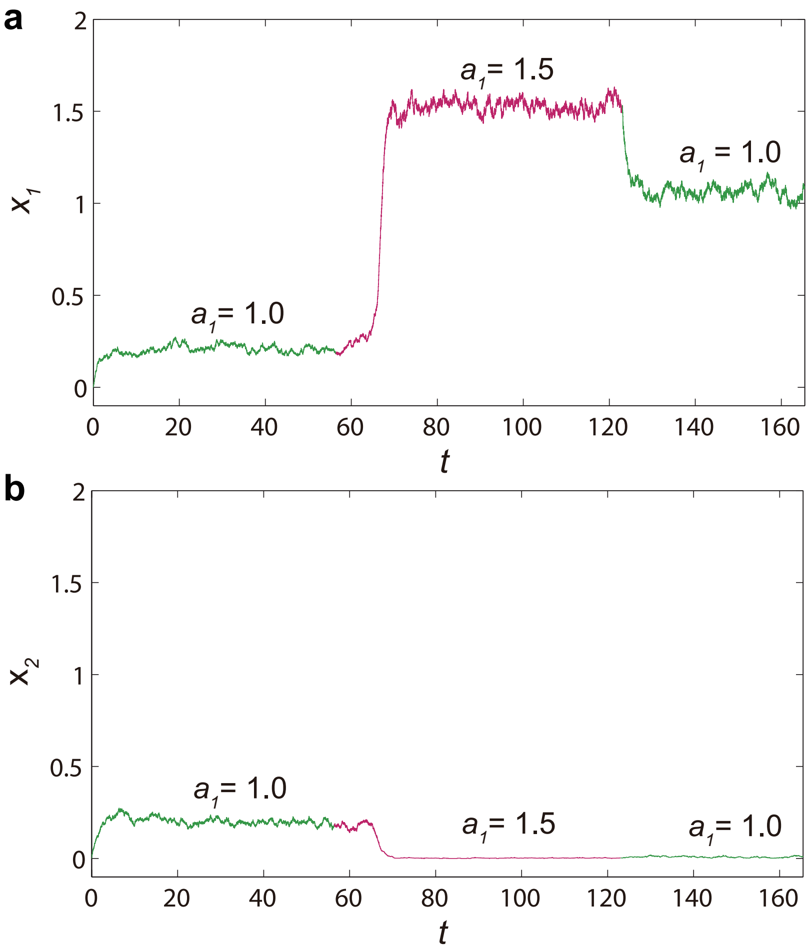

Fig. 16. Control of a stochastic model. Time series of variables x_1 (a) and x_2 (b). In the simulation, we multiply the values a_1, a_2, b_1, b_2 and s by 100 to obtain biologically reasonable protein abundances, while other parameters are unchanged. The final stochastic results are rescaled to match the ODE model results. Green and red lines represent the systems with $a_1 = 1.0$ and $a_1 = 1.5$, respectively.

to escape from the attractor with single parameter perturbation, multiple parameter perturbation should be tested - see Supplementary Note 7.

In the main text, we address the issue of control constraint by focusing on the minimum control time τ associated with two edges in the T-cell system as examples. Here, in Supplementary Table 1 we list the results from tuning all the identified edges that can steer the system from a cancerous state to the normal state, which include the critical coupling strength μ_c for each edge, the power-law scaling parameters α and β for the minimum control time [$\tau_\mathrm{m} = \alpha \cdot |\mu_\mathrm{n} - \mu_\mathrm{c}|^\beta$, Eq. (2) in the main text]. The MSEs in the fitting are also listed. Additionally, in the Boolean model, the logic relationship for all the multiple in-edges towards one given node is identically "AND". Thus, when translating the Boolean model to the continuous-time model, all the in-edges share the same parameter values of μ_c, α, and β.

We also test the case of driving the system from a normal state to a cancerous state. In particular, each of the two experimentally adjustable parameters, the edge from node "Caspase" to "Apoptosis" and the self edge of "Apoptosis," can be used for the control. We find that, for each control parameter, the relationship between its strength and the minimal control time also follows an algebraic scaling law: $\mu_\mathrm{c} \approx 0.8778$, $\alpha \approx 1.1626$, where $\beta \approx -0.6268$. This result is in accordance with clinical studies that revealed that T-LGL leukemia disease results from dysregulation of apoptosis [105, 106].

2.5.4. Supplementary Note 2: Phase Diagram.

A phase diagram illustrates how different choices of the parameters affect the system's stable asymptotic states (attractors). Supplementary Figure 15 shows the phase diagram of the two-node GRN system with respect to variations in a_1 and b_2. Each point in the diagram represents, for the particular combination of values of a_1 and b_2, the whole set of possible attractors of the system.

There are seven possible combinations of attractors in the diagram. As shown in Fig. 5(d) in the main text, if we set out to control the system from attractor $\mathbf{A}$ to attractor $\mathbf{C}$, we can first steer the system from $\mathbf{A}$ to $\mathbf{B}$ through perturbation on a_1 and then drive the system from $\mathbf{B}$ to $\mathbf{C}$ by tuning b_2. Note that the sequence of a_1 and b_2 is important here: if we first perturb b_2, the system in attractor $\mathbf{A}$ will be driven to attractor $\mathbf{D}$. When this happens, the system will remain in $\mathbf{D}$, regardless of any additional parameter adjustments, rendering unrealizable the control goal to drive the system into attractor $\mathbf{C}$. This scenario can also be seen from the phase diagram in Supplementary Fig. 15. In particular, starting from the dark red region, with the particular combination of parameters, there are 4 attractors: $\mathbf{A}$, $\mathbf{B}$, $\mathbf{C}$ and $\mathbf{D}$. As we increase a_1 and set the parameters to the red area, attractor $\mathbf{A}$ disappears and its basin is merged into that of one of the remaining three attractors ($\mathbf{B}$, $\mathbf{C}$, and $\mathbf{D}$). From Fig. 4(e) in the main text, we see that $\mathbf{A}$ migrates into $\mathbf{B}$. Thus, when we withdraw the perturbation on a_1 and turn on the perturbation on b_2, the possible attractors of system are $\mathbf{C}$ and $\mathbf{D}$ (the light green area). Figure 5(d) in the main text also indicates that $\mathbf{B}$ migrates to $\mathbf{C}$. We note that, in the phase diagram, it is difficult to distinguish into which state $\mathbf{A}$ merges, but this can be readily accomplished through the attractor network in Fig. 5(d) in the main text, which indicates unequivocally that the basin of $\mathbf{A}$ is absorbed into that of $\mathbf{D}$.

2.5.5. Supplementary Note 3: Termination Criteria and Calculation of Control Strength and Minimum Control Time.

For all systems studied in this paper, of particular importance to control is the relationship between control strength and minimum control time. The attractor network needs to be constructed first based on the procedures described in **Methods** in the main text. From the attractor network, we can obtain the control parameter for the transition between any two states. For each control parameter, we choose several different values which can realize the control and use a *bisecting* *search* to find the minimum control time. We then apply linear regression to the data on a double logarithmic scale to find the value of μ_c. In the bisecting search process, the time interval is chosen to be $t_\mathrm{s} = 10^{-2}$. For the T-cell and two-node GRN systems detailed in the main text, we choose T_f to be 100. For the three-node GRN system, we choose T_f to be 1000. The results for each system are illustrated in Supplementary Table 1-3 and the following notes.

2.5.6. Supplementary Note 4: Parameter Control in the Two-Node and Three-Node GRNs.

For the two-node GRN system [Eq. (3) in the main text], the corresponding attractor network consists of four attractors, denoted by $\mathbf{A}$, $\mathbf{B}$, $\mathbf{C}$, and $\mathbf{D}$, respectively. All parameter controls to realize the transitions among them are given in Supplementary Table 2, together with the critical coupling strength, the minimum control time, and so on.

Similarly, for the three-node GRN system [Eq. (4) in the main text], eight attractors($\mathbf{A}$, $\mathbf{B}$, $\mathbf{C}$, $\mathbf{D}$, $\mathbf{E}$, $\mathbf{F}$, $\mathbf{G}$ and $\mathbf{H}$,) constitute the attractor network. Supplementary Table 3 illustrates the critical coupling strength and the minimal control time to realize control.

2.5.7. Supplementary Note 5: Algorithms to Find Attractors.

Given a nonlinear dynamical network, the following procedure can be used to locate all the attractors.

1. For a given parameter set, we define the search space according to the maximum and minimum possible values of each state variable. For a GRN, the maximal value of each steady state is the activation rate divided by the degradation rate whereas its minimum value is zero. For example, for our two-node GRN model, we obtain that the maximal initial value for x_1 is $(a_1 + b_1) \cdot k^{-1}$ under the assumption that the leakage term is negligible.
2. Divide the phase space into a grid to generate a large number of initial conditions (grid points). Evolve each initial condition under the system dynamics to determine the final attractors of

the system. Increase the grid resolution until no new attractors appear. For example, for our two-node GRN, the initial conditions are chosen from a 11×11 grid in the two-dimensional phase space region determined by the respective ranges of the dynamical variables. There are then 121 different initial conditions, which lead to four distinct attractors. Doubling the grid resolution results in no new attractors, enabling us to conclude that there are four distinct attractors.

3. For each attractor, calculate the eigenvalues of Jacobian matrix to determine its relative stability.

2.5.8. Supplementary Note 6: Parameter Control Method in Stochastic Model.

Our nonlinear control framework is also applicable to stochastic systems. To demonstrate this, we convert the ODE model of two-node system [Eq. (3) in the main text] to a set of Langevin equations for biochemical reactions and use the Gillespie algorithm to approximate the stochasticity [107]. Supplementary Figure 16 shows a particular control process from attractor $\mathbf{A}$ to $\mathbf{B}$. As discussed in the main text, $\mathbf{A}$ has low abundance in both x_1 and x_2, and $\mathbf{B}$ has high abundance in x_1 and low abundance in x_2. From the attractor network in Fig. 5(d) of the main text, we see that by increasing a_1, we can drive the system from $\mathbf{A}$ to $\mathbf{B}$. Thus, we first set the system in $\mathbf{A}$ with $a_1 = 1.0$. At $t = 60$, we increase a_1 to 1.5, and at $t = 120$, we change a_1 back to 1.0. We see that, for $t > 120$ when the perturbation on a_1 has been withdrawn, the system spontaneously evolves into the attractor $\mathbf{B}$.

2.5.9. Supplementary Note 7: Control Based on Multiple Parameters.

To figure out the optimal parameter combinations for controlling nonlinear networks of even moderate size is computationally prohibitive at the present. However, for small networks, this can be done. For example, for the three-node GRN system studied in this paper, multiple parameter control is needed to induce certain state transition, e.g., from attractor $\mathbf{H}$ to attractor $\mathbf{B}$ in Fig. 7 in the main text. However, for the T-cell network, there are several dozens tunable edges. A surprising finding is that, because of the simplicity of the attractor network, it is only necessary to apply perturbation to any one of the 48 tunable edges to realize control.

It is interesting to note that, the sequential combination of control dosage derived from our attractor network may be regarded as a kind of control based on parameter combination. For example, it has been known that the human embryonic stem cells (hESCs) can be differentiated to a pancreatic fate under stepwise exposures to different signaling factors [108, 109]. However, the functional pancreatic fate would not occur if the differentiation steps are permuted. The non-interchangeable sequence can be understood using the concept of our attractor network, where one parameter modification represents one stage protocol. For example, in Fig. 5(d) in the main text, the hESCs correspond to attractor $\mathbf{A}$, by increasing the value of a_1 (stage 1) and then that of b_2 (stage 2), we can drive the system to attractor $\mathbf{C}$. However, if we increase b_2 first (stage 2 first), we will not be able to drive the system to the attractor $\mathbf{C}$ by increasing the value a_1 (stage 1) [see also the top branch of attractor $\mathbf{D}$ in Fig. 5(a) in the main text]. We emphasize that these results do not imply that the sequential combination method is restricted to perturbation to one parameter at a time. Indeed, recent works suggested that simultaneous therapy with two drugs can be much more effective than sequential therapy [110].

2.5.10. Supplementary Note 8: Algorithmic Complexity and Computational Cost.

In the attractor network, a link is determined when the undesired attractor vanishes upon application of control parameter perturbation of certain magnitude (within some predefined range). For each attractor, we perform a bisecting search for all the tunable parameters to establish the possible links in the attractor network. In each search, the number of checks to see if the attractor has disappeared is $\log_2(1/\Delta)$, where Δ is the accuracy in the estimate of the critical perturbation amplitude. The total number of bisecting searches is the number of attractors, N_{S}, multiplying the number of tunable parameters, N_{L}. In a nonlinear system, the number of attractors depends on the system size. For example, for a boolean network, there are 2^N possible states. While the actual number of attractors can be much less than 2^N, it depends on the network size N. The number of control parameters is the number of controllable links. Assuming that the network is sparse (as in many biological networks), the total number of checks is $\approx \log_2(1/\Delta) \times N_S \times \rho N^2$, where ρ is the connection probability. The bisecting searching needs to be performed once for a sufficiently large time duration τ of the control. The reason is that, if the control is achievable for a link for a longer duration, the same control can be realized for a shorter duration but with a larger control amplitude.

For nonlinear and complex dynamical systems, the relation between control perturbation and escaping from an attractor can be discontinuous and/or non-monotonic. In such a case, a “blind” application of the bisecting search to build up the attractor network and to estimate the computational cost may fail. This difficulty, however, can be overcome by using the method of parameter continuation with multiple initial conditions, which is standard in generating and analyzing the bifurcation diagram of dynamical systems. Especially, one can choose a small number of random initial conditions and a small set of parameters in a physically/biologically meaningful range, and determine the distinct attractors that the system possesses. The result will be a global picture of the possible attractors of the system in a small number of parameter intervals, which will facilitate greatly the computational task.

3 . EMERGENCE, EVOLUTION AND SCALING OF ONLINE SOCIAL NETWORKS

Online social networks have become increasingly ubiquitous and understanding their structural, dynamical, and scaling properties not only is of fundamental interest but also has a broad range of applications. Such networks can be extremely dynamic, generated almost instantaneously by, for example, breaking-news items. We investigate a common class of online social networks, the user-user retweeting networks, by analyzing the empirical data collected from Sina Weibo (a massive twitter-like microblogging social network in China) with respect to the topic of the 2011 Japan earthquake. We uncover a number of algebraic scaling relations governing the growth and structure of the network and develop a probabilistic model that captures the basic dynamical features of the system. The model is capable of reproducing all the empirical results. Our analysis not only reveals the basic mechanisms underlying the dynamics of the retweeting networks, but also provides general insights into the control of information spreading on such networks.

3.1. Introduction

Online social networks have become an indispensable part of our modern society for obtaining and spreading information. A piece of breaking news can activate a corresponding online social network, through which the news topic can spread rapidly to many individuals. By its very nature an online network is necessarily time dependent, growing rapidly in size initially as the news spreads out and saturating after certain amount of time. Since online social networks concerning certain topics can be active for only a transient period of time, they are *extremely dynamic*, which is quite distinct from, *e.g.*, the typical networks studied in the literature where they can be regarded as stationary with respect to the time scale of typical dynamical processes supported. A question of interest is whether there are general rules underlying the evolution of online social networks. A viable approach to addressing this question is to analyze large empirical data sets that are becoming increasingly accessible [111]. In fact, recent years have witnessed a growing research interest in online social network systems. There have been efforts in issues such as network and opinion co-evolution [112], users participation comparison for topics of current interest [113], information diffusion patterns in different domains [114, 115], the dynamics of users' activity across topics and time [116, 117], users behavior modeling on networks [118, 119], popular topic-style analysis in the Twitter-like social media [120–122], users influence in social networks [123], and language geography studies of Twitter data set [124].

In this paper, we aim to uncover the fundamental mechanisms underpinning the dynamical evolution of online social networks through empirical-data analysis. Our data come from Sina Weibo, a twitter-like microblogging social network medium in China. The appealing features of the data include wide publicity, real-time availability of information, and message compactness. Similar to Twitter, Weibo attracts users through all kinds of breaking news and spotlight topics, such as the "Japan Earthquake", "Oscar Ceremony", "Boston Marathon Terrorist" and so on. All users can see messages, called Weibos in Chinese, published by concerned users. Given a specific topic of interest, an individual can join the corresponding online social network simply by retweeting (forwarding) or tweeting (posting) the interesting Weibo [125]. To be concrete, we take the empirical data set of the Weibo topic on "Japan Earthquake" and focus on the spatiotemporal dynamics of the user-user retweeting network in terms of characterizing quantities such as the network size, the in-degree and out-degree distributions which correspond to the frequencies of retweeting other or being retweeted by others, and the in- or out-degree correlations. Our main findings are the following: (1) initially the network size increases algebraically with time but it begins to plateau at a critical time when another significant topic of interest emerges; (2) both the in- and out-degrees of the dynamic online-social network follow fat-tailed, approximately algebraic distributions, and (3) the average out-degree is approximately independent of the average in-degree from degree correlation analysis. Based on these results and the rules of online social-network systems, we articulate a theoretic model for the dynamical evolution of these networks. Simulation results of the model agree well with those from the empirical data. Our analysis also suggests a controlled approach to significantly enhancing information spreading on online-social networks.

3.2. Results

The 2011 Japan earthquake is a 9.0 magnitude undersea mega-thrust earthquake occurred on March 11 in the north-western Pacific Ocean near Tohoku, Japan. It was the most powerful earthquake ever hit Japan, which triggered powerful tsunami waves and caused nuclear accidents in the Fukushima Daiichi Nuclear Power Plant complex [126], leading to tremendous loss of human lives and large-scale infrastructure damages. This catastrophe aroused wide concerns and discussions all over the world, especially in China. Since Weibo is the most accessible online social medium in China, a large number of Chinese users joined Weibo to discuss the earthquake and related issues, forming an extremely dynamic user-user retweeting network. We analyze more than 500 thousands Weibo items concerning “Japan Earthquake”, starting from the 1^{st} day of earthquake until the 100^{th} day (defined in Methods). A simple way for a user to join the Weibo social network is to retweet other users’ Weibos. The user-user retweeting network can be generated from the data by identifying the retweeting actions among the users. In particular, when a Weibo published by user i is retweeted by user j, we draw a *directed* link from i to j. If j retweets the Weibo published by i again, another link from i to j is added, and so on. In some cases, if a Weibo published by user i and retweeted by user j, and then this retweeted Weibo is retweeted by user m, we draw two directed links from i to j and i to m respectively. There can then be duplicate links between any two users in the retweeting network. In the network, a relatively large value of the

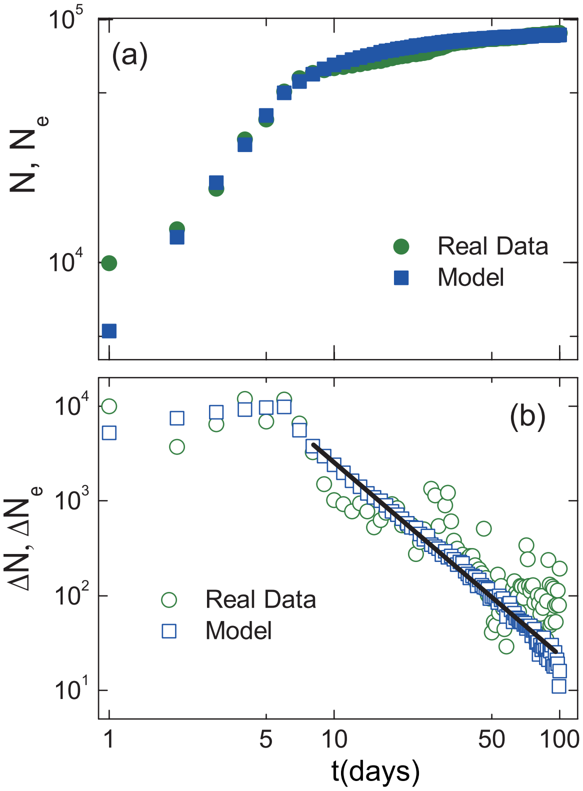

Fig. 17. Evolution of user-user retweeting network triggered by the 2011 Japan earthquake. (a) evolution of the cumulative number N of users with time (green circles), where N_e is from our model (blue squares). (b) The corresponding "instantaneous" growth rates ΔN and ΔN_e.

out-degree indicates that the corresponding user may act as a main source of information, while a large value of the in-degree suggests a high level of retweeting activities of the corresponding user.

3.2.1. Evolution of the User-User Retweeting Network.

Figure 17(a) shows the evolution of the number N of users involved by retweeting links in days (green circles). We observe that for the initial period of about 7 days, the size of the network increases approximately algebraically with the scaling exponent of about 1.3. At the critical time t_c, where $t_c \approx 7$, a crossover behaviors occurs, after which the number of nodes increases slowly or plateaus. While in general, an algebraic scaling relation does not permit the definition of some global growth rate, we can still define an "instantaneous" growth rate, the increment ΔN per day. As shown in Fig.17(b), the "instantaneous" growth rate is approximately constant for $t < t_c$, but for $t \geq t_c$, the rate decreases approximately algebraically from about 10^4 per day to about 10^1 per day at the end of the data duration.

The remarkable change in the temporal behavior of the system on the 7^{th} day demands a sensible explanation. By looking into the data further and searching for other medium information about "Japan Earthquake", we find that, at the critical time t_c, many users switched to discuss the issue of "Salt Rush", which is closely related to "Japan Earthquake." In fact, on the 7^{th} day after the earthquake, a rumor began to spread in Weibo that salt may offer protection against radiation, but the radiation leak from the Fukushima nuclear plant explosion would contaminate sea-salt products [127]. This new topic switched many users' attention from the primary "Japan Earthquake" topic to the "Salt Rush" topic, and for $t > t_c$ many users stopped discussing the "Japan Earthquake" topic. As a consequence, the instantaneous growth rate for the original topic began to decrease.

3.2.2. Fat-Tailed Distribution of In- and Out-Degrees.

Figure 18(a) displays the distributions of the in- and out-degrees on a logarithmic scale, where we observe approximately algebraic scaling behaviors. Here, the out-degree of user j, denoted by k_{out}^{j}, is the total times of j's Weibo(s) being retweeted by other users in the network, and the in-degree of j, denoted by k_{in}^{j}, is the retweeting times j has performed. We note that the algebraic scaling exponents are are 3.50 for in-degree and 2.48 for out-degree distributions. Moreover, the maximum value of in-degree is 67 while the out-degree has a much larger maximum value $(5,825)$. This means that, while the capacity of any individual user to retweet others is limited, users'

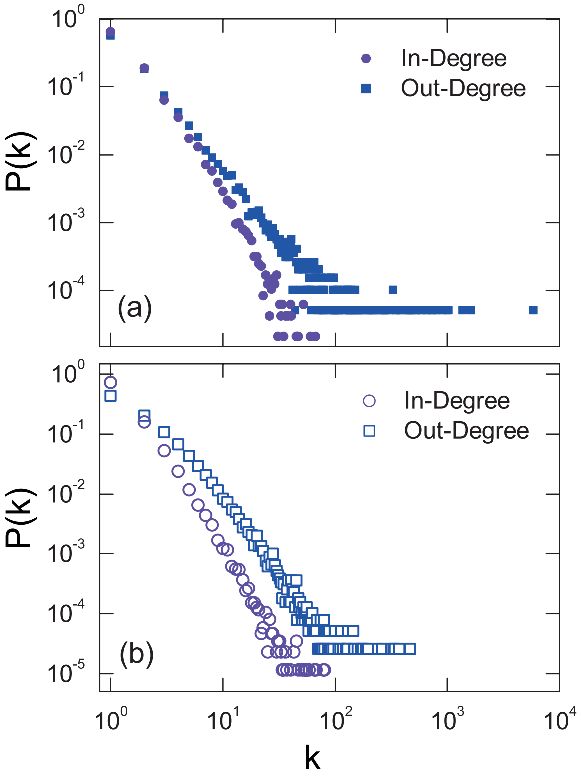

Fig. 18. Degree distribution of user-user retweeting network. In- and out-degree distributions of user-user retweeting network generated from real Japan earthquake data (a) and from model (b). The four distribution can be fitted as $P(k) \sim k^{-\alpha}$ with algebraic scaling exponents $\alpha \approx 3.50$, 2.48, 3.50, and 2.57 for real in- or out-degree and model in- or out-degree distributions respectively. The distributions were recorded at t=100 days, and the value of α are estimated using the maximum-likelihood estimator [128].

collective retweeting behavior may congregate, generating superhubs with very large out-degrees. This can be considered as an evidence for the *preferential selection* in the retweeting process introduced by the scheme that Weibo system updates and recommends information.

3.2.3. Model of User-User Behavior Network

. In the Weibo system, up-to-date topics emerge all the time and are recommended to users through the list of retweeted actions of their *friends* in the order of time. As soon as a new item is added to the recommendation list, one of the early items is removed from the list. This rule stipulates that, when some extreme event occurs, the related topics may rapidly cover the entire recommendation list to attract more users who might not have paid any attention initially. This process could also attract users who are less likely to be interested in the topic. Thus, the number of *potential* users who may join the retweeting network and then become the *enabled* users will increase. This mechanism in fact generates a self-reinforcing (positive feedback) process that makes the messages spread extremely fast initially in the Weibo system. Conversely, this kind of recommendation mechanism may also reduce the number of nodes in the network dramatically when alternative topics emerge. As can be seen from Fig. 17, the event of "Salt Rush" occurring at the 7th day after the Japan earthquake is a typical distractive topic with respect to the original earthquake topic. After the distractive topic emerged, the retweeting dynamics associated with the original topic enters into a phase with distinct scaling behaviors.

The sketch map in Fig. 19 briefly illustrates the generation scheme of retweeting network in our model with the aforesaid empirical rules and observations taking into consideration. The dynamical process of retweeting is usually initiated by some primary users' reporting of some specific events. The basic element in the process is the spontaneous retweeting action of some users, *i.e.*, one po-

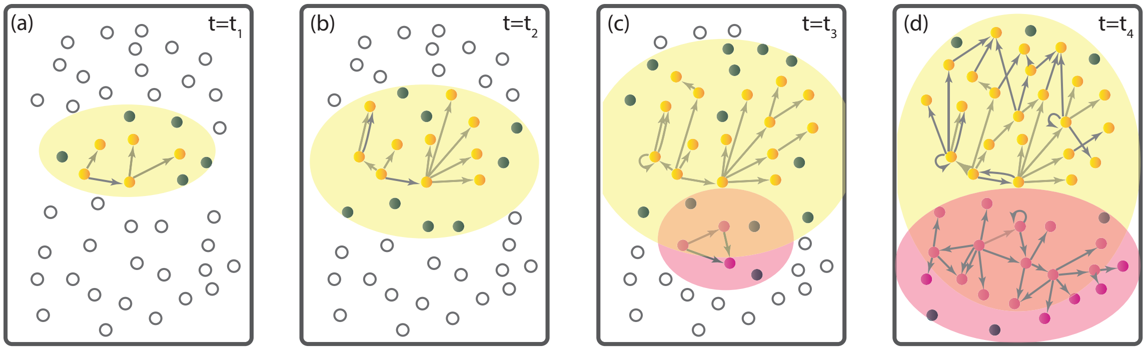

Fig. 19. Degree distribution of user-user retweeting network. (a)-(d) illustrate four instants of the system at $t_1 < t_2 < t_c < t_3 < t_4$, respectively. There exists one topic A_0 initially, while another topic A_1 emerges at t_c. The solid circles (gray, yellow or pink) covered in the yellow (or pink) background areas are the potential users who become interested in the topic A_0 (or A_1), with those colored (yellow or pink) individuals "enabled" by retweeting others. The yellow or pink solid circles respectively are the enabled users of topic A_0 or A_1.

tential user voluntarily built up a directed link pointed from another user towards him-herself. The final in-degree of each user characterizes its inherent property, *i.e.*, the level of activity in the related topic. The algebraic in-degree distribution signifies the heterogeneity and diversity in the user activities. We are thus led to define the activity level of individual i as

$$a_i = k_{\text{in}}^i / \max[k_{\text{in}}], \tag{3.1}$$

where $\max[k_{\text{in}}]$ is the maximum in-degree of all users in the system. A potential user i will retweet a related message from others, *i.e.*, to add one in-link, with probability $I_i \equiv a_i$ at each time step. As soon as the first in-link is established, the user is *enabled* to behave as a new source of the topic and can be retweeted by others. The *enabled* users are thus those connected to the user-user retweeting network, which can be identified from real data. The probability O_i for an enabled user i to be retweeted by another potential user, *i.e.*, to add an out-link, is

$$O_i \equiv (k_{\text{out}}^i + 1) / \sum_{j \in \Pi_e} (k_{\text{out}}^j + 1), \tag{3.2}$$

where Π_e denotes the set of enabled users and the proportional relation is for the reason that, if a user is retweeted by others more frequently, its actions will appear in the recommendation list more times and thus are more likely to be further retweeted.

The temporal evolution of the number of enabled users N_e can be obtained analytically. The recommendation mechanism requires that the number of potential users (denoted by N_p) increases with time rapidly in the initial phase of the retweeting process. To gain insights, we first consider the simple case where N_p is assumed to be constant. The probability for a potential user i to retweet the topic (*i.e.*, to become enabled) at each time step is $I_i = a_i$ (each user's own level of activity). The probability for user i to be enabled before time t is then $p_t^i = 1 - (1 - a_i)^t \equiv f(a_i, t)$. For the case where the users have identical activity level a, the expectation number of the enabled users at time t is $\langle N_e(t) \rangle = N_p f(a, t)$, where $N_e(t)$ is distributed binomially: $P(N_e) = C_{N_p}^{N_e} (p_t^i)^{N_e} (1 - p_t^i)^{N_p - N_e}$. Assuming that the user activity obeys a given probability distribution $P(a_i)$, the expectation number of enabled users is

$$\langle N_e(t) \rangle = \sum_{a_i} N_p P(a_i) f(a_i, t). \tag{3.3}$$

As can be seen from real data in Fig. 18(a), user activities a_i are typically heterogeneous, where the number of retweeted actions performed (the in-degrees) by users ranges from 1 to 67 and approximately follows an algebraic distribution $P(k_{\text{in}}) \sim k_{\text{in}}^{-\gamma}$, with $\gamma \approx 3.5$.

From the expressions of p_t^i and $\langle N_e(t) \rangle$, we see that the growth rate of $\langle N_e(t) \rangle$ is a monotonic decreasing function of time. However, from Fig. 17, the rate $\Delta N_e(t)$ from the real data increases in the initial phase after the network emerges. This discrepancy originates from the simple case assuming constant N_p in our probabilistic model, whereas in the real system, N_p increases rapidly initially as a result of the recommendation mechanism. It is thus necessary to take into account the fact that, at time step t', $\Delta N_p^{t'}$ new potential users become aware of the topic from their respective recommendation list in the Weibo page and then retweet with the probability $I_i = a_i$. Here, $\Delta N_p^{t'} \equiv N_p(t') - N_p(t'-1)$ and $N_p(0) = 0$. We assume that the time step t' for user i to become aware of the topic is independent of its activity level a_i. Equivalently, the activity distribution of new potential users at each time obeys the same distribution $P(a_i)$. Taking the increment of N_p into account, we obtain the expected number of enabled users as

$$\langle N_e(t) \rangle = \sum_{t'=1}^{t} [\sum_{a_i} \Delta N_p^{t'} P(a_i) f(a_i, t - t' + 1)], \tag{3.4}$$

where $t - t' + 1$ is the duration of the potential users since their awareness of the topic at t'. The exact form of the function $\Delta N_p^{t'}$ cannot be obtained explicitly, as we can observe from data only increment in the number N_e of enabled users. However, we note that the analog of N_p is the *coverage* of a spreading process of the topic associated with the recommendation mechanism, which takes place on the underlying *friendship network* of the Weibo system. We thus have [128], approximately, $\Delta N_p^t \sim n t^{\beta}$, where the parameters n and β can be obtained by fitting to the real data.

As can be seen from Fig. 17, there is a crossover behavior in the time evolution of N_e due to the emergence of some alternative topic. For convenience, we name the original topic as A_0 that takes place at $t = 0$ and the new topic as A_1 that emerges at $t = t_c$. For $t \geq t_c$, as is illustrated in Figs. 19(c)(d), A_1 competes for potential users against A_0. We assume that the basic dynamical process underlying A_1 is identical to that of A_0. The number of potential users left in A_0 for $t \geq t_c$ is thus given by $\tilde{N}_p(t) = N_p(t) - N_p(t - t_c)$, giving rise to a decreasing behavior in the instantaneous growth rate in the number of enabled users.

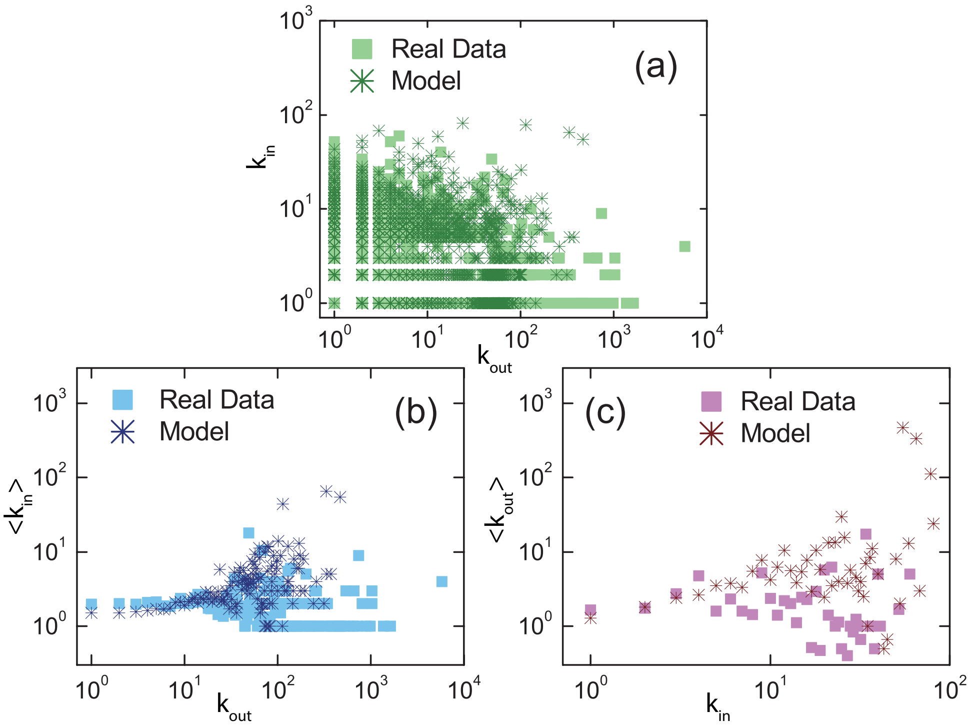

Fig. 20. Degree correlations in the user-user retweeting network generated from real data and model. (a) in-degree (k_{in}) and out-degree (k_{out}) of each user, (b) average in-degree $\langle k_{\text{in}} \rangle$ over the users of the same out-degree k_{out}, and (c) average out-degree $\langle k_{\text{out}} \rangle$ over the users of the same in-degree k_{in}.

Our model can be simulated to yield behaviors that reproduce those from the real data. In particular, in the simulation, each user's activity level a_i is proportional to its in-degree, whose distribution can be obtained from data. The increment of potential users obtained from data fitting is $\Delta N_p(t) \approx 1.89 \times 10^5 t^{-1.1}$. The topic A_0 is initially notified by $N_e(0)$ enabled users to trigger the retweeting process [*e.g.*, $N_e(0) = 3$]. Results of $N_e(t)$ from our model agree well with those from the data, as shown in Fig. 17. The reproduced in- and out-degree distributions are shown in Fig. 18, which again agree with the distributions from the real data.

To further validate our model, we calculate and compare the degree-degree correlation behaviors from the real data and our model. Figure 20(a) plots the out-degree versus the in-degree for all users in the network at time $t = 100$. Figures 20(b) and 20(c) show, respectively, the average in-degrees for users having the same out-degrees and the average out-degrees for users with the same in-degrees. The two types of average values are approximately constant but with significant spreads, and the results from our model are qualitatively consistent with those from the real data. The spread can be attributed to the fluctuation due to small amount of large in- or out-degree nodes. Furthermore, we have also calculated the Pearson correlation of the directed networks [129] of the user-user retweeting relation, and the network generated from our model. The four directed assortativity measures from Pearson correlation, i.e., the (in, in), (in, out), (out, in), and (out, out) degree correlations averaged over pairs of neighbor nodes are all found to be around zero.

What would be an effective way to spread information? In a twitter-like virtual social network, the performance of individual users in the spreading process is determined by their out-degrees k^i_{out} [130, 131]. To select users with larger out-degrees as the sources of spreading would then result in higher coverage in the subsequent time steps. To better understand the spreading process, we plot in Figs. 21(a) and 21(c) the average out-degrees of each user's neighbors, denoted by $\langle k^{\mathrm{n}_i}_{\mathrm{out}} \rangle$, versus the user's own out-degree k^i_{out}, obtained from both real data and from model, respectively, where the solid circles denote the average values of $\langle k^{\mathrm{n}_i}_{\mathrm{out}} \rangle$ over the users with the same value of k^i_{out}. We see that for those users with one given out-degree k_{out}, the value of $\langle k^{\mathrm{n}_i}_{\mathrm{out}} \rangle$ is distributed in a wide interval of about 3 orders of magnitude. However, the average of $\langle k^{\mathrm{n}_i}_{\mathrm{out}} \rangle$ over each k^i_{out} (the solid circle) is approximately constant. Figures 21(b) and 21(d) plot the product of the out-degree and the average neighbor out-degree $k_{\mathrm{out}} \cdot \langle k^{\mathrm{n}_i}_{\mathrm{out}} \rangle$, which measures the new information coverage one step after spreading from that particular user. The correlation of $k_{\mathrm{out}} \cdot \langle k^{\mathrm{n}_i}_{\mathrm{out}} \rangle$ and k_{out} on a

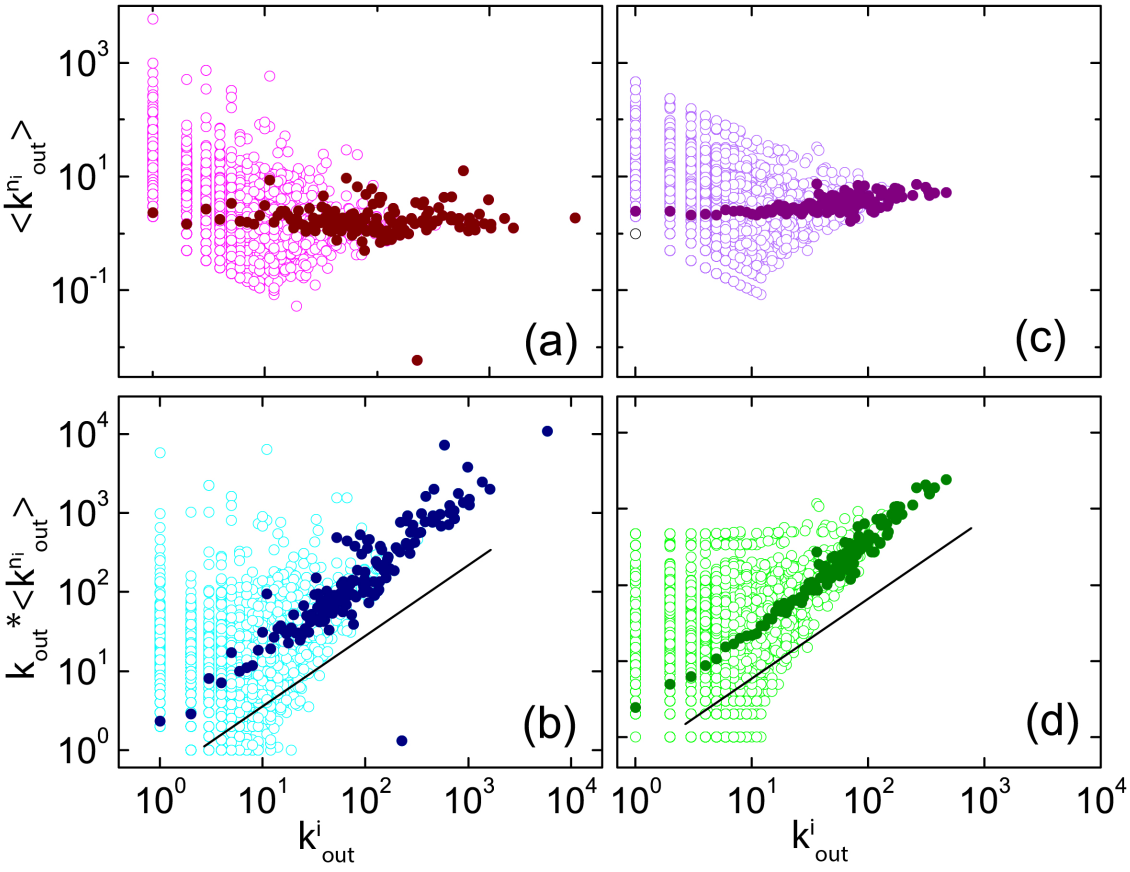

Fig. 21. Neighboring out-degrees in user-user retweeting network generated from real data and model. (a) average neighboring out-degree ($\langle k^{\mathrm{n}_i}_{\mathrm{out}} \rangle$) and out-degree ($k^{i}_{\mathrm{out}}$) of each user from real data, (b) product between the out-degree and the average neighboring out-degree ($k_{\mathrm{out}} \cdot \langle k^{\mathrm{n}_i}_{\mathrm{out}} \rangle$) of each user from real data, and (c,d) respective results from model.

logarithmic scale is approximately linear with unit slope both for real data and model. Moreover, the users with larger sum of neighboring out-degrees are those who perform well in the spreading process if they are selected to be the source. The upper-left regions in Figs. 21(b) and 21(d) thus locate the users who are not so popular (small out-degrees) but can spread news efficiently because they have relatively large sums of neighboring out-degrees. These users are the optimal candidates to be controlled for spreading information if a rapid growth of the underlying network is desired.

3.3. Discussion

Online social network systems are becoming increasingly ubiquitous in a modern society. At the present few research are considering their dynamical behavior. Using the approach of empirical-data analysis, we have developed a probabilistic model for the growth dynamics of an important class of such systems: user-user retweeting networks. Our model is capable of reproducing the dynamical and statistical behaviors of the key characterizing quantities such as the growth of the network size, in- and out-degree distributions, and the degree-degree correlations. The development of our model also leads to insights into controlling the information-spreading dynamics on these extremely dynamic networks. Our work represents an initial step in understanding, modeling, and controlling online social network systems, with potential applications not only in social sciences (*e.g.*, for controlling opinion spreading) and commerce (*e.g.*, for developing efficient recommendation algorithms), but also in other disciplines where rapidly time-varying, dynamic networks arise.

3.4. Materials and Methods

3.4.1. Data Collection

The data contains $490,243$ Weibo items with the key word “Japan Earthquake”, starting from the day of earthquake (March 11) and ending on June 19, so the duration of the data set is 100 days. **In the dataset,** $89,113$ **items have the retweeting or retweeted actions.** The collected Weibos have the following features: unique message ID of each published Weibo (Mid), unique user ID of each Weibo user (Uid), the publishing time of each Weibo (CreatedAt), the source Weibo's Mid if it is retweeted (rtMid, empty if the Weibo is not retweeted).

4 . A BIOMIMICRY BASED UNIVERSAL MODEL FOR MEME POPULARITY IN DIVERSE SOCIAL NETWORKING SYSTEMS

We analyze large data sets from a diverse online social networking (OSN) systems and find that the growth dynamics of meme popularity exhibit characteristically different behaviors. For example, there is a linear growth associated with online recommendation and sharing platforms, a plateaued (or an "S"-shape) type of growth behavior from a web service focusing on helping users to collect bookmarks, and an exponential increase from the largest and most popular microblogging website in China. Does a single framework with a common set of dynamical rules exist that can explain the distinct behaviors in a universal manner? We provide an affirmative answer in this paper. In particular, inspired by biomimicry to take advantage of cell population growth in microbial ecology, we first construct a base growth model for meme popularity in OSNs. We then take into account human factors by incorporating a general model of human interest dynamics into the base model. The final hybrid model contains a small number of free parameters that can be estimated from data. We demonstrate, using five big OSN data sets from diverse OSN systems, that our model is universal in the sense that it can successfully predict the various distinct meme growth dynamics. Our study represents the first attempt to incorporate traditional microbial growth models in biology with meme popularity, and our universal model can be used to gain insights into critical issues such as classification, robustness, optimization, and control of online social networking systems.

4.1. Introduction

Online social networking (OSN) systems are becoming ubiquitous and play an increasingly important role in the modern society, as they provide an unprecedented platform that supports communications among a vast number of users all over the world. Due to the availability of massive time series data sets in OSN systems, a quantitative system analysis becomes feasible [112,114–122,132–145]. There were previous efforts in investigating issues such as network and opinion co-evolution [112], users behavior modeling on networks [118,119], the dynamics of users' activity across topics and time [116,117], human interest dynamics in e-commerce and communication data sets [135], evolution dynamics of forwarding network in the Weibo platform [136], competition among different Twitter topics [134,137,141], popular topic-style analysis in the Twitter-like social media [120–122], information diffusion patterns in different domains [114,115], and the effect of coexistence of different OSN network services [140]. These studies mainly considered two common perspectives, the collective behaviors of users and the dynamics of posts or memes. Based on specific empirical findings, e.g., certain power-law scaling relations, mathematical or physical models were developed with the aim to reproduce the scaling relations. For instance, a two-layer model was proposed to characterize the viral dynamics and media influence [146], a branching process was used to explain the power-law distributions of meme popularity [137,141], and a Bayesian probabilistic model was developed to characterize the evolution of tweets [147]. Although these models are able to simulate or predict certain aspects of the meme popularity in real OSN systems, they are often dependent upon the structure of the underlying social network, which limits their applicability to a specific type of social networking platform with specialized functions. Due to the vast complexity of and diversity in the OSN systems, to develop a quantitative, generally applicable model for the dynamical evolution of key variables of empirical interest remains an outstanding and challenging problem. In this paper, we present, for the first time, a hybrid model for the dynamics of memes based on a combination of biomimicry consideration with inspiration from microbial ecology, physical reasoning of human behaviors, and empirical laws extracted from big data sets. The model is universal as it predicts accurately characteristically distinct growth behaviors from a diverse array of OSN systems.

Typically in an OSN system, memes such as news, ideas, information, knowledge or rumors attract users' attention and induce heterogeneous dynamical behaviors in the network. Some memes can go viral, some might receive consistent attention, and some simply get ignored. It has been challenging to study the mechanisms that drive the fates of different types of memes on a microscopic scale. In a previous work [134], it was found that in OSN systems, the distribution of meme popularity is typically heterogeneous as a result of the mutual "competition" among different coexisting memes for users' attention. This observation provides the base for the proposal of a theoretical model to describe the dynamical evolution of memes with a particular focus on the influence of users actions on information diffusion [137, 141]. The mathematical backbone of the theory is branching processes and it has successfully explained certain empirical observations such as the distribution of meme popularity growth associated with the *Twitter* datasets. A key assumption of the theory, which makes feasible a detailed analytic treatment, is that users have constant activity rates and memes are equipped with the same "fitness." While identical users and memes enables a mathematical analysis, a key ingredient of meme dynamics in real-world systems, namely heterogeneity in user and meme behaviors which is typical and indispensable in OSN systems, is not captured by the theory. An alternative modeling approach is to apply a self-exciting point process (e.g., the Hawkes process [148]) to predict the popularity of tweets based on partial information about the network structure and observations of retweet times [147, 149]. This type of models can successfully predict the total final number of retweets but, because of the focus on information diffusion at the individual level, the common phenomenon of group popularity is not accounted for. At the present, a comprehensive model that incorporates the heterogeneity of users and memes to describe quantitatively the collective dynamics of meme popularity is lacking.

A more significant challenge in the construction of a model for meme popularity lies in its distinct growth behaviors for different OSN systems. In particular, from five big data sets from diverse social networking platforms, we find three characteristically different types of behaviors: linear, plateaued (or "S" shaped), and exponential growth in time. Is it possible to construct a single model that can explain these distinct growth behaviors? Naturally, such a model will contain a small number of free parameters whose values depend on the specific OSN system and can be estimated from data. Except for the differences in the values of the free parameters, the basic elements of the model are identical for OSN systems from diverse contexts. In this sense the model can be regarded as universal.

In this paper, we exploit biomimicry to develop a universal model for meme popularity dynamics in diverse OSN systems. The general idea is that, while OSN systems are man-made with a great deal of complexity, nature has solved problems in more complex systems. Animals, plants, microbes, and even cells are extremely well self-organized natural systems with superior functions and efficiency. Our first step is to hypothesize an equivalence between meme evolution in OSN systems and microbial cell population growth and develop a probabilistic, population-level base model. In such a model for the dynamical evolution of cell population [150–162], at a given time a cell can experience one of the three possible events: division (generation), death, and survival. Likewise, memes are the "microscopic" elements of an OSN system. At a given time, the possible events that can happen to a meme are similar: posting/forwarding, being overwritten (exclusion), or simple survival, which are equivalent, respectively, to cell division, death, and survival in a microbial system, as shown on the left side of the schematic illustration in Fig. 22. This equivalence, or biomimicry, leads to a base model for meme population growth. While this model captures certain features of the meme dynamics, our data analysis shows that large

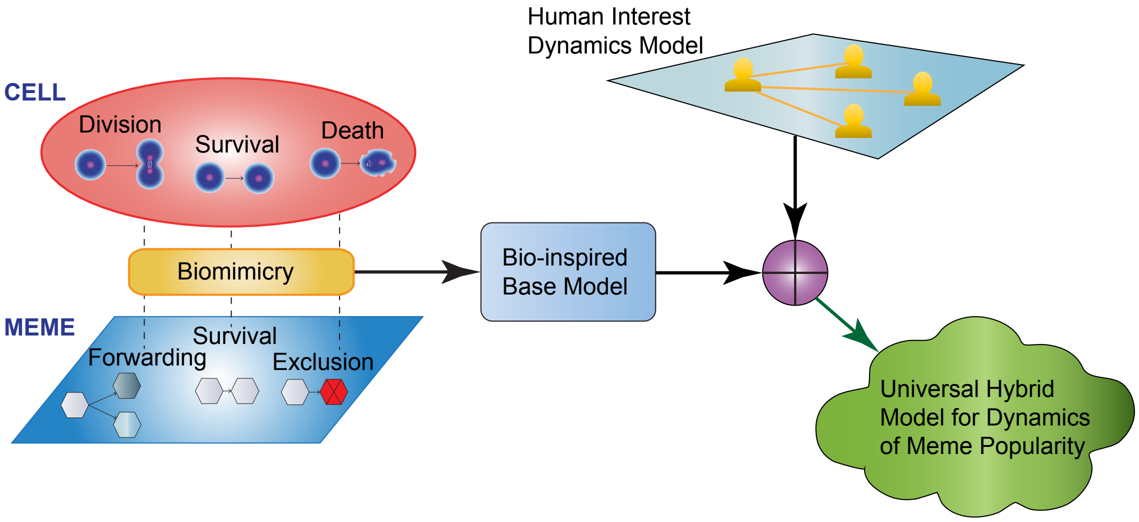

Fig. 22. An illustration of the basic principles underlying the construction of a universal model for meme popularity dynamics: biomimicry and human interest dynamics. Cell population dynamics in microbial ecology contain three basic elements: cell division, death, and survival. The dynamical evolution of memes in OSN systems has three corresponding elements: forwarding, exclusion, and survival. A base model for meme popularity dynamics can then be constructed according to the cell growth model in biology. Human factors, however, play a significant role in meme spreading and propagation and therefore must be taken into account. A combination of the biology inspired base model and human interest dynamics model leads to a universal hybrid model for meme popularity dynamics.

errors can arise when attempting to predict the detailed growth dynamics of meme population. Additional considerations beyond the biological equivalence must be sought. This is reasonable as OSN systems are man-made and human factors can play a significant role in the dynamics. The second step in our model building is then to incorporate human interest dynamics that intuitively should have a strong correlation with meme popularity. Incorporating a general model for the dynamical evolution of human interest into the bio-inspired base growth model, we arrive at a hybrid model for meme popularity dynamics, as shown on the right side of Fig. 22. The final model contains four free parameters that can be determined from data, as we demonstrate using empirical big data sets from diverse OSN systems in interest sharing (e.g., various *Douban* platforms and *Delicious*) and the online OSN platform *Weibo*. The striking result is that the model can predict the detailed meme popularity growth behaviors in all OSN systems studied, regardless of their characteristically distinct underlying mechanisms, providing a solid ground for its validity and universal applicability. While our model predicts three distinct meme popularity growth behaviors from five data sets, we are confident that, with the values of the four free parameters determined from data, the model is capable of predicting growth behaviors beyond the three types uncovered here. To be able to predict the dynamical evolution of memes is of great social, economical, and political interest. What we have achieved in this paper is a universal model that can be used to predict the meme dynamics with only limited available information.

4.2. Results

4.2.1. Biomimicry: From Microbial Ecology to Social Network.

In microbial ecology, quantitative analysis of cell population is a fundamental approach [150–162]. Due to time and economic constraints, most cell models are at the population level because it is impractical to monitor the state of each individual cell and count the number of living cells frequently. A typical cell population model contains three processes: cell division (birth), death, and survival. Likewise, in an OSN system, it is often unrealistic to study the behavior of every single post, but it is feasible to obtain data from the collective behaviors of these posts. Especially, a meme can be generated and passed onto another under in response to certain social event (birth), it can disappear if there is no or no longer any interest it (death), or it can simply be associated with the same user without any change (survival). This analog suggests that a meme associated with an individual is dynamically equivalent to a cell in a microbial ecological system.

To place the cell-meme correspondence on a quantitative footing, we consider the probabilistic model of cell growth and mortality [156]. At each basic time step, three possible events can occur to an individual cell: it can divide, can die, or remain alive. The probabilities of the respective events are represented as functions of time with parameters estimated from experimental data. Consideration of the events and the probabilities provides a base to formulate a meme probabilistic framework. An illustrative example is shown in Fig. 23. In this toy social system, there are are seven users and four types of memes that constitute a bipartite network, as shown in Fig. 23(a), where the former and the latter are connected through posting or forwarding actions. Especially, two users are directionally connected if a meme is forwarded from one to another. Figure 23(b) shows the recording of the posting forwarding actions related to each type of meme - essentially a space-time representation of how the memes are created and evolve. For example, users $U1$, $U4$, $U5$ and $U7$ post meme types $M1$, $M2$, $M3$ and $M4$ at time $t = 0$, $t = 1$, $t = 2$, $t = 2$, respectively, while users $U2$, $U3$ and $U4$ forward the $M1$ type at $t = 3$, $t = 4$ and $t = 5$, respectively. As a result, four users ($U1$, $U2$, $U3$, and $U4$) are linked to the meme type $M1$, as indicated in the bipartite network in Fig. 23(a). Similarly, user $U5$ forwards meme type $M4$ at $t = 3$, $M3$ at $t = 4$ and $M2$ at $t = 5$,

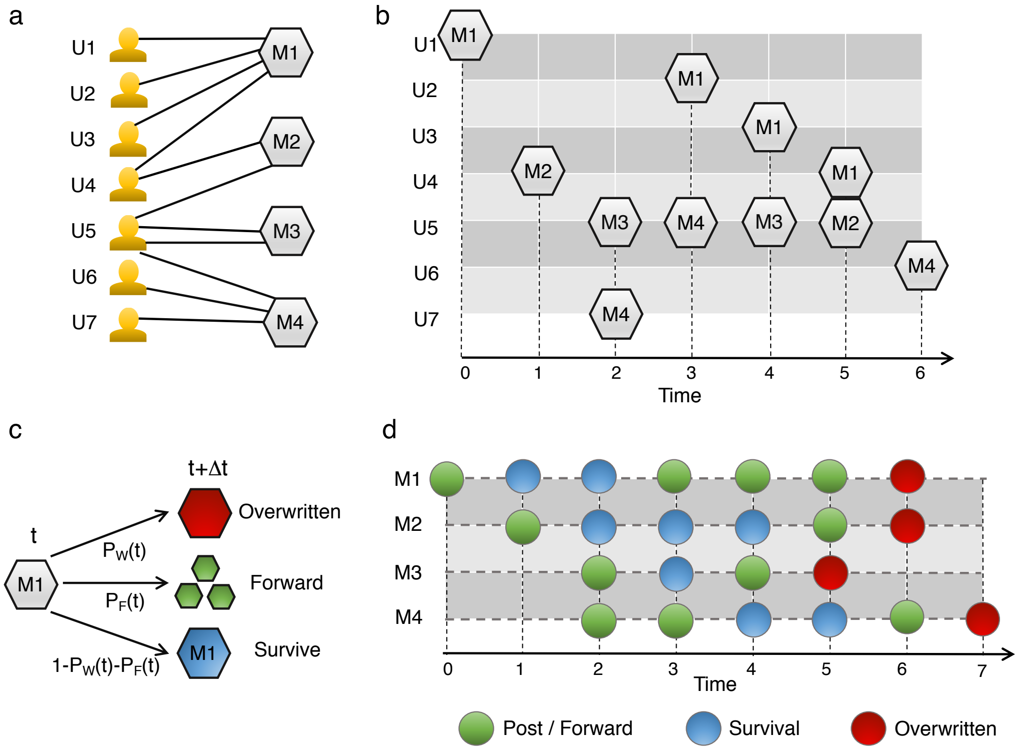

Fig. 23. Schematic illustration of meme popularity dynamics. The system has seven users and four types of memes, where a meme associated with an individual user corresponds to a cell in microbial ecology. (a) Bipartite graph representation of users and memes, which are connected by posting or forwarding actions. (b) Representation of forwarding actions at different time. Each horizontal line is associated with an individual user and each hexagon represents a meme. For a horizontal line, a hexagon appearing at a time indicates that a meme (regardless of its type) has been created or forwarded at this time. (c) The three events that can occur to a meme at a given time, together with the respective probabilities: $P_F(t)$ - the probability of being forwarded, $P_W(t)$ - the probability of being overwritten (exclusion probability), and the survival probability $1 - P_F(t) - P_W(t)$. (d) An example of the time evolution of meme popularity, where the green circles represent the posting or forwarding event, the blue circles define a survival event, and the red circles correspond to an exclusion event.

and user $U6$ forwards type $M4$ at $t = 6$. For a meme associated with a user at a given time, it can be forwarded, be overwritten (excluded), or simply survive, as indicated in Fig. 23(c), which corresponds to the three possible events that can occur to a cell in microbial ecology: division, death, or remaining alive. Figure 23(d) shows an example of the occurrences in time of the three events for each of the four types of meme. From a population perspective, a meme population starts to grow when it is first posted. The population size increases when users have forwarded this meme. Between each pair of consecutive forwarding events, the meme is in the survival state. After the last forwarding event, the meme is regarded as being excluded or dead.

The population of a type of meme at any time is determined by the numbers of newly forwarded, excluded, and survived posts. Let $F(t)$, $W(t)$, and $S(t)$ be the number of forwarded, excluded, and survived memes, respectively, at time t. The meme population at this time can thus be written as

$$N(t) = S(t) + F(t). \tag{4.1}$$

The interactions among memes are described by the forwarding and exclusion probability functions, $P_F(t)$ and $P_W(t)$, respectively, which determine the values of $F(t)$ and $W(t)$.

4.2.2. Empirical Findings.

The probabilities $P_F(t)$ and $P_W(t)$ are key quantities in our meme popularity model, which can be estimated from empirical data. We consider five big empirical data sets: *Delicious*, *Douban Book*, *Douban Movie*, *Douban Music*, and *Sina Weibo* (or *Weibo*). Details of how memes are defined and how data are recorded are described in **Methods**. Figure 24 shows the forwarding and exclusion probabilities for the five data sets. We find it convenient to organize the five data sets into three groups in terms of their nature: *Douban Book, Movie and Music*, *Weibo*, and *Delicious*. To make a meaningful comparison, we normalize the time (L) as well as the probabilities $P_F(L)$ and $P_W(L)$. Initially, the two normalized probabilities have relatively low values and they begin to increase after certain time. This initial "silent" phase corresponds to the lag phase that occurs before the accumulation phase for cell growth in microbial ecology [150–162], where the growth and mortality rates are expected to be low at the beginning and increase with time. The striking phenomenon is that, for the five data sets arising from a diverse variety of social networking contexts, the time evolution of the probabilities exhibits quite similar features, suggesting a universal mechanism underlying the evolution of meme popularity.

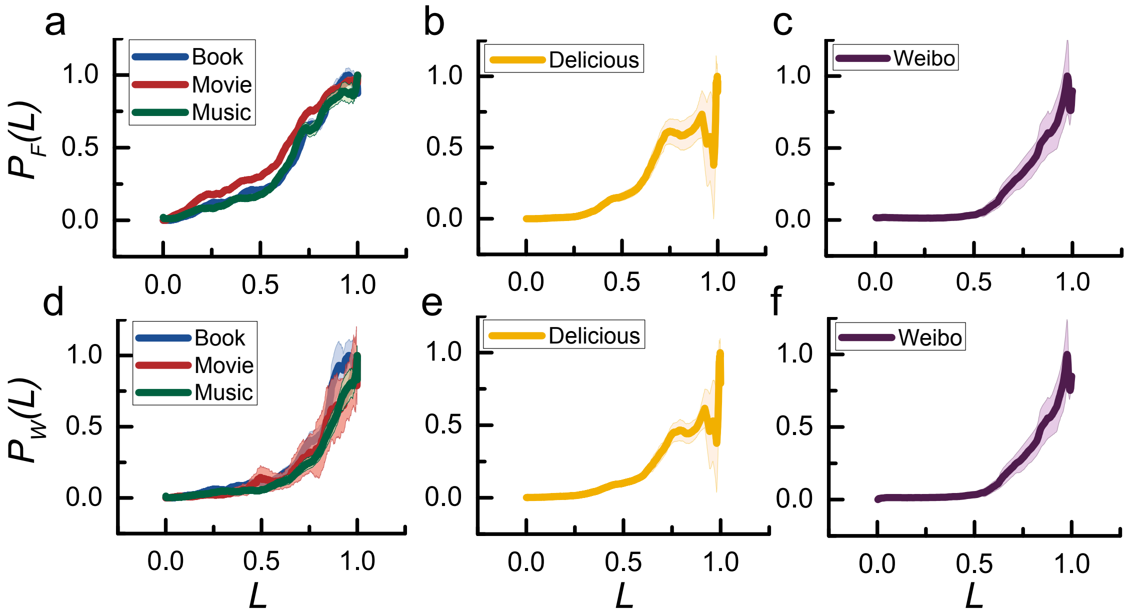

Fig. 24. Evolution of forwarding and exclusion probabilities estimated from empirical data sets. In each panel, lines and the corresponding shadow areas indicate the average forwarding or exclusion probabilities, together with the error bars. The time and the probabilities have been normalized to facilitate a quantitative comparison among the five data sets that arise from different social networking contexts. The probabilities for the group of data sets *Douban Book, Movie* and *Music* (a,d), for *Delicious* (b,e), and for *Weibo* (c,d).

4.2.3. Beyond Biomimicry: Incorporation of Human Interest Dynamics.

While biomimicry can provide pivotal insights into uncovering the laws governing human systems, certain aspects of the human behaviors are fundamentally absent in any biological system. In particular, in the context of our present study, while microbial cell evolution provides a base for constructing models for OSN systems, the former is a purely biological system and the latter are man-made. There ought to be differences between the two types of systems. Indeed, in spite of the remarkable agreement among the forwarding and exclusion probability functions across OSN systems of different nature (Fig. 24), a detailed examination of the evolution of the meme population $N(t)$ for the three groups of data sets reveals some discrepancies, indicating the need to include additional factors that are not present in the microbial cell evolution model. Our intuition suggests incorporating human factors into models of OSN systems. For the dynamical evolution of meme popularity, the most pertinent factor is human interest.

Meme growth in OSN systems is a human behavior. In general, human behaviors are driven by human interest. In the past decade or so, there has been a great deal of efforts in modeling and understanding human behavior and interest dynamics [135, 163–169]. Of particular interest are the interevent time and event determination statistics such as the distribution of the interevent time of human behaviors, the distribution of the return time to revisit a particular interest (inter), interest ranking and transition (inter), and the distribution of the time that an interest lasts (event determination). Because of the sensitive dependence of human interest on environment factors, it is reasonable to speculate that the dynamical underpinnings of human interest are random [134, 170, 171], and this has led to the development of Markovian type of models for human interest where an individual history of interests (except those in the immediate past) plays no role in his/her present action [172–174]. However, deviations from the Markovian dynamics were reported [135,175,176].

For example, a systematic analysis of a number of big online data sets revealed that algebraic (power-law) scaling behavior characteristic of non-equilibrium complex systems govern both interevent time and event determination statistics associated with human interest dynamics [135, 163]. This implies that there are intrinsic dynamical rules underlying the human interest dynamics. It was hypothesized that there are three basic dynamical rules governing the evolution of human interest: preferential return, inertial effect, and exploration of new interests, and a mathematical model was developed accordingly to explain the algebraic scaling laws [135].

To take into account human interest dynamics in constructing our meme popularity model, we make use of the previously established principles: the burst characteristic of human behavior, the algebraic distribution of the time required to revisit an interest, and exploration of new interest. In particular, we first assume that the time interval τ for an individual to forward the same meme to other individuals in the OSN system obeys the distribution $p(\tau) \sim \tau^{-\alpha}$, where $\alpha > 0$ is the algebraic scaling exponent that is effectively a parameter in our model. Next, we assume that an individual has the probability $\rho{\cdot}n^{-\beta}$ to discover new interests (memes) and the probability $(1-\rho{\cdot}n^{-\beta})$ to return to previous interests (memes), where $0 < \rho < 1$ and $\beta > 0$ are two parameters, and n is the number of hoppings among different interests [135, 168, 169]. Here, the quantities $p(\tau)$ represent the burst characteristic of human behaviors and ρ can be regarded as an event determination probability, respectively, and the corresponding parameters α and ρ can be determined from data. Parameters n and β have little impact on the popularity, therefore, we approximate individual's event determination activities as ρ to forward new meme and $(1 - \rho)$ to forward old meme.

Figure 25 displays the users behaviors extracted from our empirical datasets based on consideration of human interest dynamics. The particular quantity that we examine is the activation rate, the ratio of the number of activated users at time t to the number of all users involved by this time.

Figures 25(a-c) show, for all five data sets, the user activation probabilities versus the normalized time L. We see that, associated with the datasets *Douban Book, Douban Movie* and *Douban Music*, users exhibit a similar behavior of the activation rates and the three curves can be well fit by a *sigmoid function* [Fig 25(a)]. For the dataset *Delicious* whose activation rate curve is shown in Fig. 25(b), there exists a "step." We thus divide the curve into two parts and fit each with a sigmoid function with distinct parameters. For the dataset *Weibo*, as shown in Fig 25(c), a single sigmoid function fits activation curve well. Figure 25(d) shows the distributions of the individual interevent time from five datasets, which are approximately algebraic with the value of the exponent α ranging from 1 to 3. Figures 25(e) and 25(f) exhibit the distributions of event determination probability ρ associated with the data sets *Delicious* and *Weibo*. Note that in the data sets *Douban Book, Movie* and *Music*, users tend to visit or comment on an item only once, leading to a high peak in the distribution of ρ near the unity value. Table 5 summarizes the parameters of the sigmoid functions in Figs. 25(a-c) and the parameters α and ρ characterizing the interevent time and event determination activities estimated directly from the data sets. Note that, for the *Delicious* data set, there are two fitting parameters, B and C, for the two distinct sigmoid functions.

TABLE 5: Fitting parameters for empirical datasets. Parameters for sigmoid functions are B and C and parameters characterizing the interevent time and event determination activities are α and ρ. B and C are normalized through $B = \frac{\tilde{B}}{\log(T)}$ and $C = \frac{\tilde{C}}{\log(T)}$, where $\tilde{B}$ and $\tilde{C}$ are obtained from empirical datasets, T is the length of the time series.

Data Sets	B	C	α	ρ
Delicious	0.24 and 0.40	0.80 and 0.80	1.73	0.54
Douban Book	0.07	0.55	1.38	1.00

Douban Movie	0.07	0.55	1.53	1.00
Douban Music	0.07	0.55	1.46	1.00
Sina Weibo	0.24	0.61	1.50	0.56

4.2.4. Construction of Model for Dynamical Evolution of Meme Popularity.

Our considerations of microbial cell evolution and human interest dynamics in combination with empirical observations enable a formal construction of a model to describe the dynamical evolution of meme popularity. We start from a basic model that includes meme diffusion and user activities. We assumes a fixed group of potential users. At each time step, a random fraction of the users become active (enabled), and each enabled user can post memes or forward some of the existing memes. In accordance with the quantitative behaviors extracted from the empirical data sets, we assume that the fraction of active users ($P_A(L)$) follows a sigmoid function with parameters B and C:

$$P_A(L) \sim \frac{1}{1 + e^{-B \cdot (L-C)}}. \tag{4.2}$$

For an active user, the interevent time τ indicating the intervals when this user decides to forward (post) memes follows a power law distribution with the parameter α. Finally, the user has the probability $(1 - \rho)$ to forward an old meme that he/she has forwarded before and the probability ρ to forward a new meme. Our hybrid meme diffusion model is illustrated in Fig. 26.

To simulate the model, we consider a fixed group of $N_f = 1000$ users. At each time step t, $N_f \cdot P_A(t)$ randomly selected users become active. The interevent time distribution and event determination activities of these users can be modified through changes in the parameters α and ρ. Specifically, for an activated user U_i, we generate a time series of forwarding actions based on: (1) the time interval τ that a user has forwarding action follows the distribution $p(\tau) \sim \tau^{-\alpha}$, (2) the probability for this user to forward a new meme is ρ and an old meme is $(1-\rho)$. We then record the forwarding and exclusion probabilities, as well as the meme popularity at each time for different choices of the parameters. Note that in the analysis of empirical datasets, to exclude death events caused by the duration of the datasets, i.e. memes or users get into the datasets late, we truncate F and W curves at the peak values, which are around 80% of total duration.

4.2.5. Simulation Results.

Our hybrid model has four parameters: B and C which determine the users' sigmoid activation rate (Eq. 4.2), α that regulates the inter-event time intervals and ρ that accounts for event determination activities (probability of exploring new memes). We simulate the model for different choices of parameters to check the parameter sensitivity of the key quantities representing the model outcome: the forwarding and exclusion probabilities. We then estimate the four parameters directly from the five empirical datasets.

Figure 27 shows the simulation results of the forwarding and exclusion probabilities for different choices of the parameters α, ρ and C. For panels in a row, we modify one parameter and compare the results, where the nominal parameter values are $B = 0.5$, $C = 0.5$, $\alpha = 1.5$, and $\rho = 0.5$, for the reasons that (1) a commonly used sigmoid function has $B = C = 0.5$, (2) users' interevent time distribution exponent α is typically in the range [135] from 1 to 3, and (3) it is reasonable to assign equal probabilities for both old and new meme when the event determination activities are not known, leading to the choice $\rho = 0.5$. A key result of Fig. 27 is that the forwarding and exclusion probabilities are sensitive to user actions. In the sigmoid activation function, a small value of C means that the users get activated at an early time, resulting in increased forwarding and exclusion probabilities at the early time, as shown in Figs. 27(a) and 27(d). In terms of the interevent time distribution, a large value of α means that the distribution of the interevent time is more concentrated, indicating that many users have short τ. This leads to a slow growth in the forwarding probability at an early time, as shown in Fig. 27(b). While the increment is not dramatic as compared with that in the forwarding probability, there is a slight delay in the rising of the exclusion probability in early time when the value of α is large, as shown in Fig. 27(e). Meanwhile, the forwarding probability changes slightly with different event determination parameter ρ where, for example, a large value of ρ, which leads to a higher probability to forward new memes, results in the later increment of forwarding probabilities. And the high probability of new memes indicates small amount forwarding events per meme on the average, which causes the early increment of exclusion probabilities. In all six panels, the amplitude of the increase in the forwarding probability with different parameters are always larger than those of exclusion probabilities. This is because in simulations, a meme is regarded as being excluded only after the last recorded forwarding actions so that the influence of user actions on the overwriting action is postponed.

To validate our model, we set its four essential parameters to the values estimated from real data and compare the model predicted dynamical evolution of meme popularity with the real one. We do this for all five big OSN data sets, as shown in Fig. 28, where the growth curves of the normalized meme popularity with time from the model and from data are displayed. The fitting parameters for all give datasets are listed in Table 6. The remarkable feature in Fig. 28 is that, regardless of the disparity in the nature of the data sets and regardless of the characteristic differences in the growth dynamics of meme popularity, our model predicts behaviors that agree with the actual behavior accurately and in detail. In particular, for the data sets *Douban Book, Movie* and *Music* in Fig. 28(a), the meme popularity grows linearly with time and our model predicts this behavior precisely. For the data set *Delicious*, the meme popularity growth curve exhibits an "S-shape" feature, which is characteristically different from the linear behavior in Fig. 28(a), but the model prediction, which is in good agreement with the empirical result, captures this distinct feature unequivocally! For the growth behavior in Fig. 28(c) from the data set *Weibo*, the meme popularity exhibits an approximately exponential behavior over time, and our model still predicts this behavior correctly!

We have also provided analytic results of the model in **Methods**. We apply Runge-Kutta method to solve Eq. 4.7 and the results are shown in cyan dash lines of Fig. 28.In both simulated and analytic models, the parameters (B, C) associated with the users activation function and the event determination parameter ρ are key to determining the shape of meme popularity growth curves. Comparing the parameters in Table 6 with those in Table 5, we see that, for each data set, the fitting parameter values are largely about the values that are directly retrieved from the data, indicating that fluctuations of the parameters about their "exact" values can be tolerated in our model without affecting dramatically its prediction. That is, our hybrid model not only predicts successfully the meme popularity growth dynamics, but also is robust against parameter inaccuracy and uncertainties.

TABLE 6: Fitting parameters in both simulated and analytic models. B and C are normalized through $B = \frac{\tilde{B}}{\log(T)}$ and $C = \frac{\tilde{C}}{\log(T)}$, where $\tilde{B}$ and $\tilde{C}$ are obtained from empirical datasets, T is the length of the time series.

Data Sets	B	C	α	ρ
Delicious	0.15	0.50	1.50	0.60
Douban Book	0.07	0.50	1.50	0.99
Douban Movie	0.07	0.50	1.50	0.99
Douban Music	0.07	0.50	1.50	0.99

Sina Weibo	0.20	0.68	1.50	0.60

4.3. Discussion

Recent years have witnessed an unprecedented rapid growth of OSN systems. These systems have become ubiquitous in the modern society with the tendency to eventually replace many of the traditional social networks. To understand the dynamics of and the dynamical processes on OSN systems is of uttermost importance to the well being of the human race in the future. There have been efforts in analyzing OSN systems in the past few years [132,135–138,141,146,158,177–181]. A common approach is to uncover certain statistical or scaling relations through (big) data analysis, and then to articulate a quantitative model to reproduce the specific scaling laws (often power-law scaling). While this approach has indeed yielded great insights into the dynamics of specific OSN systems, the inconvenient truth is that these systems are diverse and exhibit characteristically different behaviors even for a single quantity of interest.

A ubiquitous phenomenon with general interest is the growth dynamics of meme popularity in OSN systems. Our analysis of empirical data from a diverse of array of OSN systems reveals a lack of common growth behavior: depending on the system the growth dynamics can be linear, “S-shaped,” or exponential. We ask the following seemingly impossible question: can a universal model be articulated to capture and predict the characteristically different growth behaviors of meme popularity? Naturally, in order to produce distinct dynamics, the model must necessarily contain free parameters whose values depend on the specific system and should be estimated from data. In spite of this relaxation of constraint, some kind of phenomenological model, as done in previous works, would not be generally applicable to diverse OSN systems. We are thus motivated to conceive our model based on the fundamental dynamical elements underlying the growth and spread of meme popularity. We find biomimicry to be highly inspirational, effective, and useful for achieving our goal. Specifically, at one point during our study it striked us that the dynamics of cell evolution in microbial ecology bear similarities to the dynamics of meme popularity.

In microbial ecology, at any time a cell can experience one of the three events: division, death, or survival. Likewise, in OSN systems, at any time a meme can be forwarded, can be overwritten, or can survive. In both contexts, each event is associated with a probability that is a function of time with free parameters. The close resemblance between cell and meme popularity growth dynamics provides the microscopic base for a population model of memes. Through data analysis, we find that the probability functions have the shape of a sigmoid function, with two free parameters that can be determined from data. However, such a bio-inspired growth model is not sufficient to capture the detailed dynamical behaviors of meme popularity growth, as the dynamics of the OSN systems involve human behaviors and can thus be significantly more complex than biological cell growth. For meme popularity, it is natural to attribute the modeling element beyond cell growth to human interest dynamics, for which models have been developed recently. Incorporating the ingredient of human interest into basic cell growth, we end up with a hybrid model that contains four free parameters - all determinable from data. With the parameter values so estimated, we demonstrate that our model has the ability to predict the detailed, characteristically distinct growth dynamics of meme popularity in a diverse array of OSN systems. To our knowledge, this is the first time that a universal model is successfully developed to capture and predict the dynamical evolution of a broadly interested quantity characteristic of modern social networking systems.

From the control point of view, our hybrid model leads to a new framework to understand the general mechanisms underlying the dynamics of OSN systems and how they may be manipulated or harnessed. Regardless of the specific features in the OSNs studied in this paper [from bookmarking shared networks (*Delicious*) to interest discovered media (*Douban*) and microblogging system (*Weibo*), they all share the same "microscopic" dynamical elements (e.g., forwarding and exclusion) that results in certain rapid growth behavior. It is conceivable that the growth dynamics can be controlled through perturbations to these dynamical elements. This may lead to network design that, for instance, optimizes meme populations. It is also possible to manipulate the robustness or resilience of information spreading in OSN systems to external attacks through modulating the forwarding and exclusion probabilities. Taken together, our work uncovers the fundamental principles underlying meme popularity in OSNs through the approach of biomimicry in combination with insights from human behavior dynamics, which may shed lights on further development of social networks and outstanding issues such as classification, robustness, optimization, and control.

4.4. Materials and Methods

4.4.1. Data Collection.

The massive empirical data sets analyzed in this article are from large-scale online systems: *Delicious*, *Douban* and *Weibo*. The basic statistical properties of datasets are listed in Table 7, where the term "Records" represent the number of records in each raw data set, "Memes" denotes the total number of memes in each raw data set, "Users" indicates the total number of users involved in each raw data set, and "Durations" is the duration of each processed data set analyzed. The details of these data sets are described, as follows.

TABLE 7: Basic properties of five data sets studied in this paper.

Data Sets	Records	Memes	Users	Durations (Months)	References
Delicious	361,928,091	886,405	43,968,955	42	[182]

Douban Book	20,199,759	455,177	557,879	53	[135]
Douban Movie	65,205,220	504,066	86,503	52	[135]
Douban Music	25,596,271	403,835	395,035	50	[135]
Sina Weibo	3,868,099	224,079	559,979	13	[136]

Delicious: Delicious is a web service focusing on helping users collect bookmarks. Each record consists of the operation time, user's ID, Universal Resource Locator (URL) and the tag of URL. In this data set, the meme was defined as a bookmark, and users' collections of bookmarks are regarded as forwarding actions.

Douban: Douban is a major Chinese Social Networking Service website. It allows users to record information and make recommendations related to books, movies, and music, etc. Each record contains users id, timestamps and rating action towards item. In this paper, we analyze three Douban datasets: *Douban Book*, *Douban Movie* and *Douban Music*. We define each rated item as a meme, and treat each rating action as a forwarding event.

Weibo: Sina Weibo is by far the largest and most popular microblogging website in China: it is a widely used twitter-like microblogging social network medium with more than 500 million registered users in China [183]. The appealing features of the data include wide publicity, real-time availability of information, and message compactness. Similar to Twitter, Weibo attracts users through all kinds of Breaking news and spotlight topics. All users can see messages, called Weibos in Chinese, published by concerned users. Given a specific topic of interest, an individual can participate by retweeting (forwarding) or tweeting (posting) the interesting Weibo [125]. In this dataset, for each message with the forwarding information, we record the original Weibo id, user id who forwards this Weibo and created time. Each message represents a meme and forwarding action is regarded as a forwarding event.

4.4.2. Theoretical Model and Discussions.

In Eq. 4.1 and Fig. 23, we obtain that memes population at time t depends on the amounts of survived and forwarded memes. Specifically, the relationship can be characterized by,

$$N(t) = S(t-1) + F(t-1) - W(t) + F_A(t).$$

Here $F_A(t)$ is the newly added memes at time t. From this recursive formula we can derive an ordinary differential equation(ODE) as:

$$\frac{dN(t)}{dt} = F_A(t) - W(t). \tag{4.3}$$

In simulation, at each time step we add some users into the system. And the number of new users obeys sigmoid function. Based on natural human behavior as illustrated in Fig. 26, a portion of those newly added users contributes to new memes at the same time. The ratio of added new memes is ρ, so the amount of newly added memes is:

$$F_A(t) = \rho N_i \cdot \frac{1}{1+\exp\bigl(-\tilde{B}(t-\tilde{C})\bigr)}. \tag{4.4}$$

As defined in the main text, after the last forwarding event, the meme is regarded as being overwritten or exclusive. Since users interevent time intervals follow $p(\tau) \sim \tau^{-\alpha}$. we assume the distribution of all users' last inter-event interval also follows $p(\tau) \sim \tau^{-\alpha}$. Similarly, the memes' last inter-event interval is $p(\tau) \sim \tau^{-\alpha}$. And the exclusive term $W(t)$ in Eq. 4.3 is depended on the total number of memes added into the system, which can be written as:

$$W(t) = \int_0^t \frac{\rho N_i}{1+\exp\bigl(-\tilde{B}(t'-\tilde{C})\bigr)} dt' \cdot (T-t)^{-\alpha}. \tag{4.5}$$

Here T is the final observation time as shown in Fig. 26(a). Substituting Eqs. 4.4 and 4.5 to Eq. 4.3, we obtain:

$$\frac{dN(t)}{dt} = \rho N_i \cdot \frac{1}{1+\exp\big(-\tilde{B}(\hat{t}-\tilde{C})\big)} - \int_0^{\hat{t}} \frac{\rho N_i}{1+\exp\big(-\tilde{B}(t'-\tilde{C})\big)} dt' \cdot (\hat{T}-\hat{t})^{-\alpha}, \tag{4.6}$$

where $\hat{t}$ and $\hat{T}$ are normalized time and are defined by, $\hat{t} = \frac{t\cdot\log(T)}{T}$,$\hat{T} = \log(T)$. The integral part of Eq. 4.6 can be theoretic calculated, and the equation becomes:

$$\begin{aligned}\frac{dN(t)}{dt} = \rho N_i \cdot \frac{1}{1+\exp\big(-\tilde{B}(\hat{t}-\tilde{C})\big)} - \frac{\rho N_i}{\tilde{B}} \cdot \Big(\tilde{B}\cdot\hat{t} - \log\big(1+\exp(\tilde{B}\cdot\tilde{C})\big) \\ + \log\Big(1+\exp\big(\tilde{B}\cdot(\tilde{C}-t)\big)\Big)\Big) \cdot (\hat{T}-\hat{t})^{-\alpha}.\end{aligned} \tag{4.7}$$

Note that this model simplifies lots of things, such as averaging the growth and exclusive processes. However, for large quantities of memes and users in OSNs, these approximations are acceptable. Solutions of the ODE Eq. 4.7 under different choices of B, C, α and ρ adopted from Table 6 are curves with increasing and decreasing phases. To match the settings in simulation, we also truncate curves of analytic solutions when they start decreasing, as shown in Fig. 28.

The theoretic curves in Fig. 28 indicate that the analytic model agrees well with simulation and real data results. In Fig. 28, there are three growth types: linear, ”S-shape” and exponential. From Table 6, we see that those three growth curves only differ in parameter B,C, and ρ. First we discuss the effects of B and C on meme popularity curves. B and C are parameters in the activation sigmoid function. B parameter controls the shape of sigmoid function, C controls the value of L when the activation rate reaches 0.5 in Eq. 4.2. So large C results in a late reaching at the half of the total meme popularity. And large B value leads to sharp slope of sigmoid function. In other words, the increasing rate for popularity becomes fast in the region when the normalized time L is close to C value. Therefore, large B and C lead to the popularity start growing at a later time with rapid increasing, which forms an exponential increasing curve as shown in Fig. 28(c). Similarly, when B and C are in the mid ranges, such as B is around 0.15 and C is around 0.5, the popularity curve starts increasing at an early time, reaches maximum rate at the late of time, then the exclusion decrease almost have the same rate with newly added increase rate. This forms the "S-shape" growth curves as illustrated in Fig. 28(b). And when B is small and C in mid ranges, the slope variations in sigmoid function are sluggish, which makes the grow curve of meme popularity approximates to linear. Meanwhile, the second term of Eq. 4.7 represents meme's exclusive numbers. When $\hat{t}$ is small, this exclusive term only adds a small modification to meme's popularity; when $\hat{t}$ is close to $\hat{T}$, this term plays an important role in the growth curves. ρ has a really simple effect, large ρ leads to a large absolute popularity, and small ρ leads to a small absolute popularity, and will not affects the growth shape. In reality, when ρ is very small, such as around 0.02, due to stochastic fluctuation the growth shape maybe will different.(refer to comparison between Fig. 28(a), (c) and (b)).

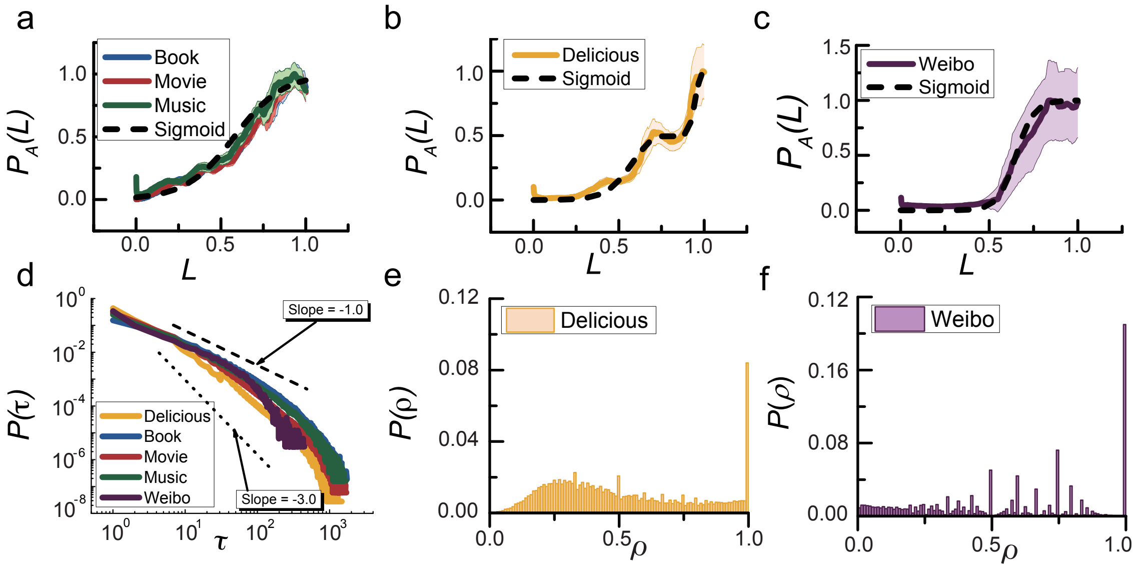

Fig. 25. Users behaviors extracted from the empirical data sets based on consideration of human-interest dynamics. (a-c) Activation curves (the fraction of users activated at normalized time L) together with the error bars for the three groups of empirical data, where the yellow, blue, red, green and purple solid lines and the corresponding shadow areas represent the average activation rates and error bars for *Delicious*, *Douban Book*, *Douban Movie*, *Douban Music*, and *Weibo*, respectively. The black dash curves are the fitted sigmoid functions. For (a), the user activation curves from the three data sets: *Douban Book*, *Movie* and *Music*, strikingly coincide with each other at a detailed level, which can fit by a single sigmoid function. For the data set *Delicious* in (b), a plateau in the user activation curve emerges, which can be fitted by two distinct sigmoid functions. For the data set *Weibo* in (d), the activation curve can be fit by a single sigmiod function. (e) Distribution of the parameter α characterizing the interevent time for all five datasets, where the two dashed lines indicate two distinct slope values. (e,f) Distributions of the parameter ρ characterizing the event determination activities from the data sets *Delicious* and *Weibo*, respectively. See Table. 5 for fitting parameters.

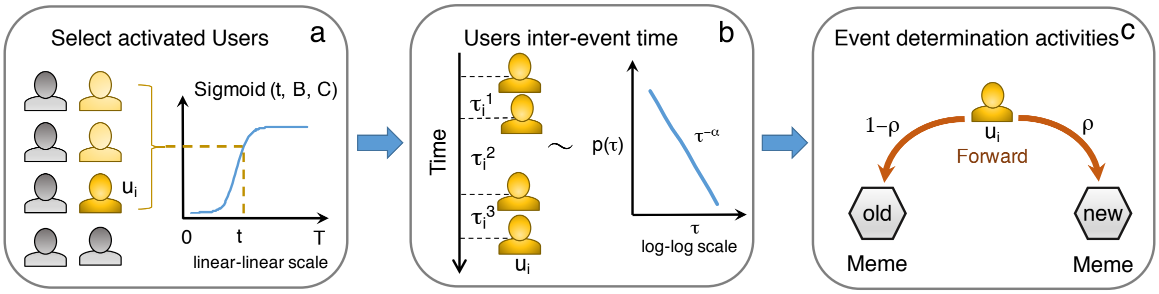

Fig. 26. A schematic illustration of the proposed biomimicry based hybrid meme diffusion model incorporating human interest dynamics and empirical observations. (a) At each time step t, a fraction of users are selected to be activated based on a *sigmoid* curve. (b) For a selected user U_i, the activities occur at different times according to the probability $p(\tau) \sim \tau^{-\alpha}$, where τ is the interval between two adjacent forwarding actions. (c) At time t, the selected user U_i has the probability ρ to forward a new meme and the probability $(1 - \rho)$ to forward an old meme. The model is hybrid because (1) the dynamical evolution of the memes follows the rules of microbial cell diffusion (biomimicry), and the probabilities $p(\tau)$ and ρ are from the human interest dynamics with key parameters extracted from actual data.

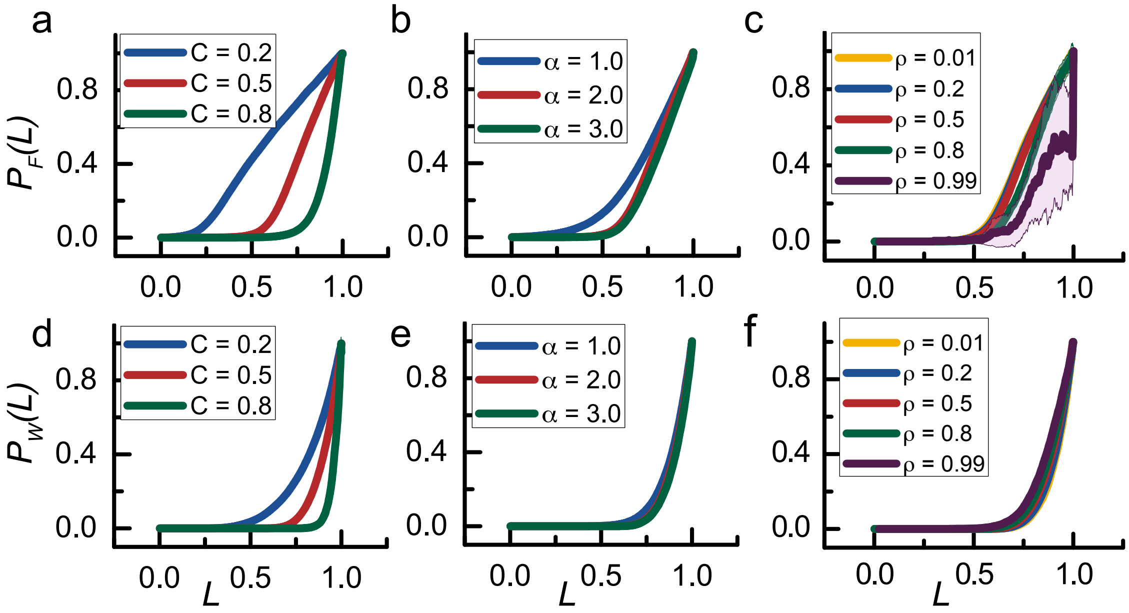

Fig. 27. Time evolution of the forwarding and exclusion probabilities generated from our hybrid model. Normalized probabilities for (a,d) different values of C in the users activation sigmoid function, (b,e) different values of α in the statistical distribution of user interevent time, and (c,f) different values of ρ in the user event determination probabilities. In all panels, the solid lines and the associated shadowed area indicate the average values and the error range.

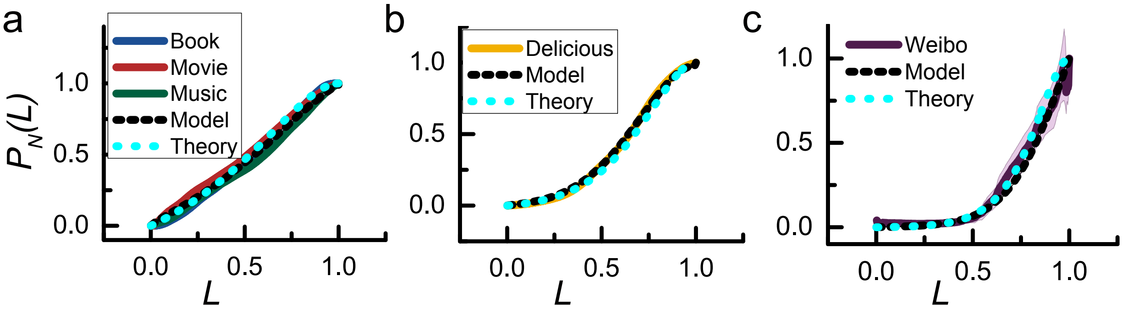

Fig. 28. Test of the predictive power of the proposed model: comparison between model predicted and real grow curves of meme popularity. Dashed and solid curves represent model prediction and the results from the real data, respectively: (a) linear growth of meme popularity for the *Douban Book, Douban Movie* and *Douban Music* OSN systems, (b) an "S-shape" type of growth behavior from the data set *Delicious*, and (c) an approximately exponential growth curve for the data set *Weibo*. The four key model parameters B, C, α, and ρ are estimated from data. The remarkable feature is that, regardless of the characteristically different growth behaviors in the meme popularity associated with diverse OSN systems, both simulated and theoretical models are capable of giving accurate prediction. Details of theoretical modeling are summarized in Methods, parameters in solving Eq. 4.7 are $T = 1000$ and $dt = 0.01$. Fitting parameters are summarized in Table. 6

5 . MULTISTATE MODEL OF WNT SIGNALING PATHWAY IN NEURAL PROGENITOR CELLS

5.1. Introduction

Researchers have found that in neural development, canonical WNT signaling pathway regulates the patterning along the anterior-posterior axis of the CNS (Central Nervous System) [184–191]. When the WNT ligands bind to the frizzled receptor, it initiates a cascade of events which include the activation of β-catenin. The accumulation of β-catenin would facilitate the activation of WNT target genes, which are then involved in the differentiation of Neural Progenitor Cells (NPCs). A recent study demonstrates that a gradient concentration of WNT signaling results in the heterogeneity of neurons from forebrain to midbrain, hindbrain and spinal cord [189]. In the experiment, they integrate TCF Optimal Promoter to clonal human embryonic stem cell. The cell lines uses GFP reporter as a homogeneous response to WNT signaling, which indicates that the level of WNT signaling is characterized by GFP expression. As shown in Fig. 29, in undifferentiated hESCs, GFP reporter is inactive at day 1; and at day 7, a heterogeneous pattern of GFP expression is observed in Neural Progenitor Cells (NPCs). In the experiment, NPCs are sorted by GFP level. Cells with low GFP levels would differentiate into neurons that form forebrain (anterior), cells with medium GFP levels would differentiate into neurons that form midbrain and those with high GFP levels would differentiate into neurons that form hindbrain and spinal cord (posterior).

In view of all the above experimental findings, in this study we propose a mathematical model that characterizes the controlling of WNT signaling pathways towards cell fate along the anterior-posterior axis of the neural tube, as shown in Fig. 30. Each module in the model corresponds to a group of Transcript Factors (TFs) or markers with similar functions. The modules are related to each other by activation or inhibition regulations, which represent positive or negative interconnection respectively. While some interconnections are derived from experiment study findings, others have not yet been observed or verified in experiments. This model uses different states to describe cell fate decisions and our focus is on which combinations of interconnections can result in the multistability of NPCs. We perform computational screening on all possible configurations before searching for triple stable steady states (3 SSSs). Our systematic search identifies three interconnections with high probabilities of generating 3 SSSs. They are (1) inhibition from anterior module (A) to receptor module (R); (2) inhibition from anterior module (A) to WNT module (W); and (3) activation from posterior module (P) to WNT module (W). Detailed analyses reveal that modifying the strength of regulation between WNT module and anterior/posterior module can impact the multistability. This is consistent with experiment findings from a separate work. Moreover, clustering and classification are performed on RNA-seq data used in a recent study and can provide potential TFs that may form anterior and posterior modules. Overall, this study proposes a systematic and integrative method to characterize the role of WNT signals in determining the regional identity of NPCs, and contributes to the studying of human brain development.

5.2. Results

5.2.1. WNT Controlling Network Model.

To explore the heterogeneity of NPCs under the control of WNT signaling pathway, we propose a mathematical model that groups genes or proteins into four modules. As shown in Fig. 30(b), “R” represents genes and proteins that are involved in the process of WNT ligands binding to frizzled receptors, “W” denotes WNT target genes, “A” stands for anterior markers and “P” corresponds to posterior markers. In the experiment, when ligands bind to frizzled receptors, the WNT target

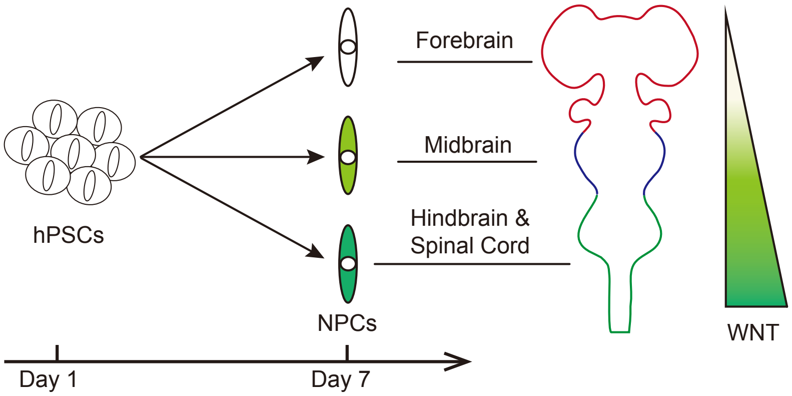

Fig. 29. Endogenous WNT signaling controls NPC differentiation bias. In a recent published experimental study [189], the protocol for differentiation of human Embryonic Stem Cell (hPSC) is: at day 1, hESCs integrated with GFP reporter have been cultured in suitable conditions. At day 7, human Pluripotent Stem Cells (hPSCs) differentiate into Neural Progenitor cells (NPCs) which exhibit varying levels of GFP expression. Then the NPCs are sorted based on the GFP level. At about four weeks, for cells with low GFPs, they would differentiate into neurons that form forebrain; similarly, for cells with medium or high GFP levels, they would differentiate into neurons that form midbrain or hindbrain and spinal cord, respectively. In the experiment, GFP level serves as a direct indication of the WNT level.

genes are activated, where generally low WNT concentration leads to high expression of anterior markers, and high WNT concentration results in high expression of posterior markers. Therefore, in the model, we predefine three interactions between different modules: “R” activating “W”, “W” inhibiting “A” and “W” activating “P”.

Based on the above assumptions, we further apply a Boolean based computational approach to systematically search for network structures based on the potential for multistability. We first enumerate all possible configurations under the predefined structures and interactions (Fig. 31). In Fig. 30(b), we assume that each unknown interaction (p_2, p_3, p_4, p_5 and p_6) has two possible types, activation or inhibition. Therefore, in total we have $2^5 = 32$ possible topologies. Each topology represents a potential interaction combination of "R", "W", "A" and "P" modules. A four-node GRN is applied to understand the underlying dynamics. Taking configuration 1 for example, the dynamical network is mathematically described as,

$$
\begin{aligned}
\dot{x}_R &= p_1 \cdot \frac{s^n}{x_W^n + s^n} + p_2 \cdot \frac{x_A^n}{x_A^n + s^n} + p_3 \cdot \frac{x_P^n}{x_P^n + s^n} - k \cdot x_R, \\
\dot{x}_W &= p_4 \cdot \frac{x_R^n}{x_R^n + s^n} + p_5 \cdot \frac{x_A^n}{x_A^n + s^n} + p_6 \cdot \frac{x_P^n}{x_P^n + s^n} - k \cdot x_W, \\
\dot{x}_A &= p_7 \cdot \frac{s^n}{x_W^n + s^n} - k \cdot x_A, \\
\dot{x}_P &= p_8 \cdot \frac{s^n}{x_W^n + s^n} - k \cdot x_P.
\end{aligned}
\tag{5.1}
$$

Here the dynamical variables (x_R, x_W, x_A, x_P) depict the ensemble gene/protein expression of each module, k represents the degradation rate, and tunable parameters $p_i, i = 1, \cdots, 8$ represent strengths of interactions. In each GRN, the dynamical behaviors of activation or inhibition are captured by the Hill function (activation: $f(x) = x^n/(x^n + s^n)$, inhibition: $f(x) = s^n/(x^n + s^n)$). In the model, we use $k = 1$, $s = 0.5$ and $n = 4$. For simplicity, here we assume the strength from "W" to "A" and "P" are equal, $p_7 = p_8$.

We perform computational screening on each of the 32 configurations. In each configuration, for each of the 7 tunable strengths, we examine five possible values: 0.1, 0.2, 0.5, 1 and 5. Therefore, in total, we have $32 * 5^7 = 2,500,000$ different systems. To be consistent with experiment findings of three regional identity in A/P axis, we calculate the multistability by recording cases that reach 3 SSSs in each of the 32 configurations under various combinations of interaction strengths ($5^7 = 78,125$ combinations). The result is illustrated in Fig. 32(a). Here we set 0.01 as a threshold and select configurations with more than 0.01 probability to reach 3 SSSs under all the 78,125 combination of strengths. We obtain configurations 6, 14, 22 and 30. Referring to the list of configurations in Fig. 31, we see that all four selected configurations only differ in p_1

and p_3, and they share 6 similar interactions: p_2, p_4, p_5, p_6, p_7 and p_8. Excluding the predefined interactions p_4, p_7 and p_8, we see that p_2, p_5 and p_6 are important to maintain the 3 SSSs, which are inhibitions from “A” to “R”, “A” to “W” and activation from “P” to “W”. That is to say, we can make a tentative guess that negative feedbacks from anterior markers to receptors and WNT target genes and positive feedbacks from posterior markers to WNT target genes, are important factors in creating the multistability of 3 SSSs. Later, we will focus on the selected configurations and perform bifurcation analysis to see how multistability changes with strengths.

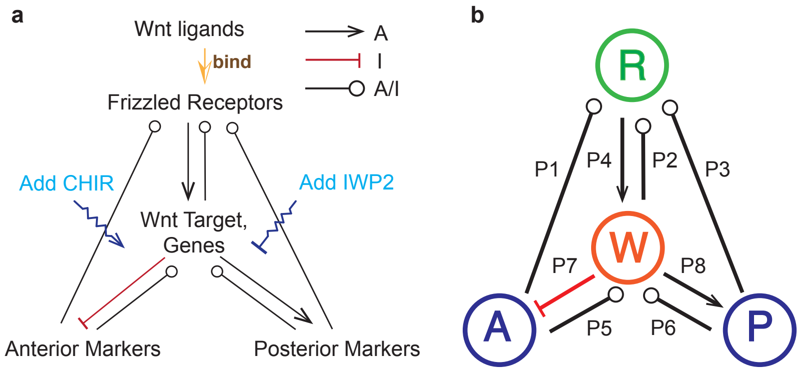

Fig. 30. Illustration of WNT controlling model. (**a**). Overview illustration of WNT signaling pathway’s impact on the heterogeneity in anterior/posterior (A/P) regional identity. (**b**) The corresponding simplified regulation model for the regulation of WNT signaling.

5.2.2. Sensitivity and Bifurcation of Multistability.

Bifurcation diagram is an analytical method that can characterize a system’s stable and unstable steady state behaviors in response to the parameter variations. We use algorithms in MATCONT package to compute the bifurcation curves [86]. From Fig. 32(a) we see that configurations 6, 14, 22 and 30 yield high potential to reach 3 SSSs in all parameter combinations we have examined. To gain a deeper insight into these four configurations, we then perform bifurcation analyses on

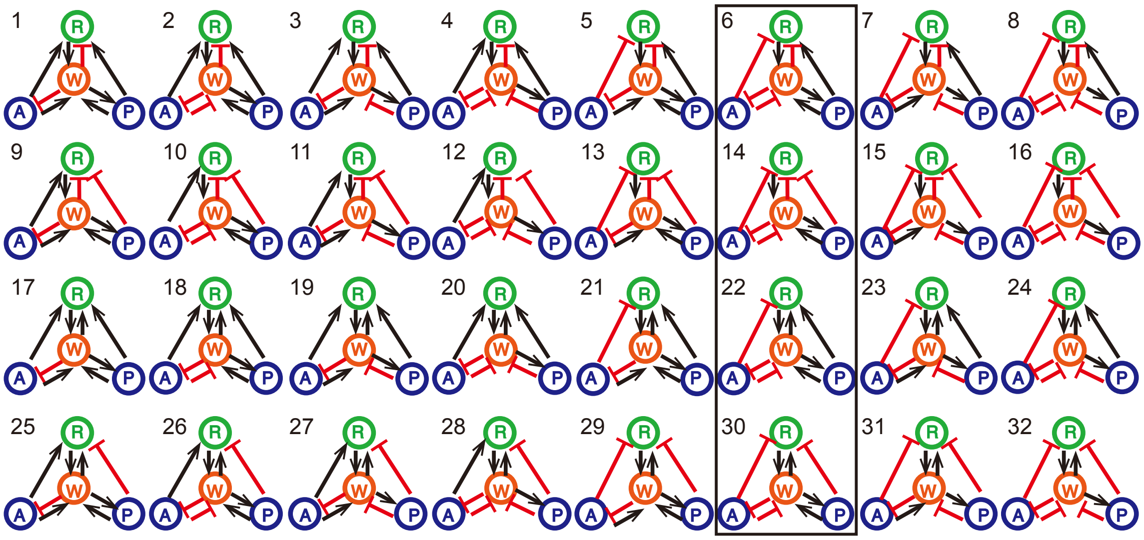

Fig. 31. Computational screening of multistate configurations. Each configuration represents a candidate network structure. Black rectangular highlights four selected configurations with high probability to reach 3SSSs.

each of them to investigate how the change of each interaction strength influences the number of states, while other parameters are kept constant in default values as: $p_1 = 0.1$, $p_2 = 0.1$, $p_3 = 0.1$, $p_4 = 0.1$, $p_5 = 1$, $p_6 = 0.5$ $p_7 = 5$ and $p_8 = 5$.

Figure 32(b) shows bifurcation results in configuration 30, and other 3 selected configurations have similar results. Here red lines denote stable steady states and dash lines represent unstable steady states. We see that strengths p_1, p_2, p_3 and p_4 all result in 3 SSSs in the value range that we have numerically examined. In the bifurcation diagram of p_5, there is a small range of values that can only generate 2 SSSs, and majority ranges of values lead to 3 SSSs. On the contrary, for p_6, only a small range of value leads to 3 SSSs, other ranges lead to 2 SSSs or 1 SSS. Lastly, for p_7 and p_8, we found some interesting phenomena. In these two bifurcation diagrams, the system can be driven from 1 SSS to 2 SSSs and to 3 SSSs. And the parameter ranges for 2 SSSs and 3 SSSs are quite large, which means in the absence of precise control of strength, we can still obtain the multistability. We further draw 2D bifurcation diagram by modifying p_7 and p_8 at the same time. Fig. 33(a) provides an illustration of how the multistability varies with both p_7 and p_8. Note that in the model, p_7 and p_8 represent the interaction from WNT target genes to anterior and posterior markers respectively. And the modeling results in Fig. 33(a) indicate that these interactions play an important role in the decision of multistability. Later, we will discuss results in experiments and how our modeling reflects these findings.

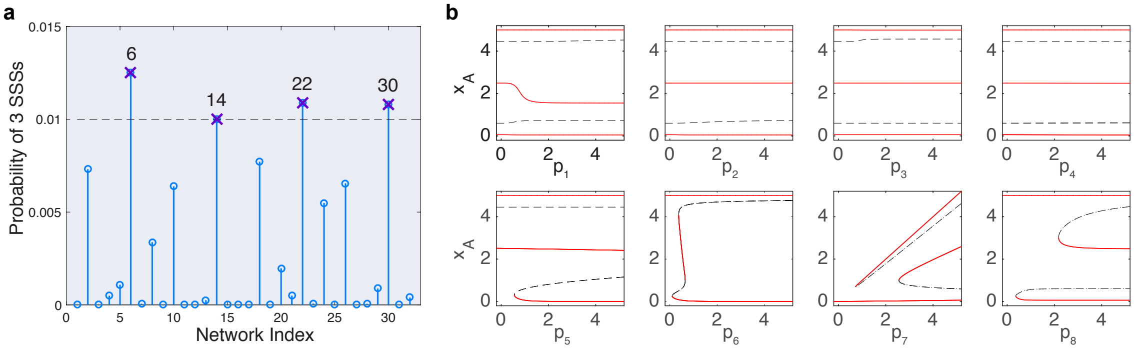

Fig. 32. Model selection and bifurcation analysis. (**a**). Probability of reaching 3 SSSs under different network configurations. Dash line represents threshold of 0.01. (**b**). 1D bifurcation of interaction strength $P1$ to $P8$. Red lines and black dash lines denote SSSs and UnSSSs respectively.

5.2.3. Model Explains Exogenous Manipulation of WNT Signaling.

In the experiment, exogenous manipulation of WNT signaling pathway can alter the multistability in NPCs. In particular, CHIR is an activating drug on WNT, and IWP2 is an inhibitory drug on WNT. In the model, we link strength p_7 with IWP2, and p_8 with CHIR. That is to say, when we add CHIR, the inhibitory strength from SP5 to Anterior is enhanced, so adding CHIR leads to a decrease in anterior markers expression. Meanwhile, when adding IWP2, the activation from SP5 to posterior markers is suppressed, and adding IWP2 results in a reduction in posterior marker expression. We use a phase diagram to illustrate these two processes. In Fig. 33(b), we use configuration 30 with parameter settings: $p_1 = 0.1$, $p_2 = 0.1$, $p_3 = 0.1$, $p_4 = 0.1$, $p_5 = 1$, $p_6 = 0.5$ $p_7 = 5$ and $p_8 = 5$. In the model, when $p_7 = p_8 = 5$, the system has 3 SSSs. Adding CHIR indicates an decrease in p_7, which means the system would be driven from 3 SSSs to 2 SSSs to 1 SSS (Path from top right to top left in Fig. 33(b)). Similarly, if we add IWP2, p_8 will decrease, and the system would also be driven from 3 SSSs to 2 SSSs to 1 SSS (path from top right to bottom right in Fig. 33(b)). When we apply two drugs simultaneously, the multistability of system is also reflected in the phase diagram. In particular, consistent with experiment results, as shown in Fig. 33(c), in the presence of 1000 nM IWP2, when the dose of CHIR increases, the system exhibits transitions from 1 SSS (Anterior only) to 2 SSSs (Anterior and Midbrain) to 2 SSSs (Midbrain to Anterior) and finally reach 1 SSS (Posterior only). In the model, we obtain similar transition as illustrated in the path from bottom right to bottom left of Fig. 33(b).

Together, our model supports and reflects experiment results in which the multistability is controlled by exogenous drugs. Next we will focus on how to identify genes that form each of the four modules.

5.2.4. Preliminary Results of Gene Classifications.

To further determine genes that belong to each module, we study RNA-sequencing data under different doses of CHIR at day 7 NPCs and perform clustering. Based on previous experiment research [192–195], we have predefined three groups of *Seed* genes, as illustrated in Table 8. Here Group 1 (G1) represents genes discovered as anterior markers, G2 corresponds to genes identified as midbrain markers, and G3 stands for genes denoted as hindbrain markers. We plot the dose response curve for seed genes in each group as shown in Fig. 34(a). From this panel we see that, in general,

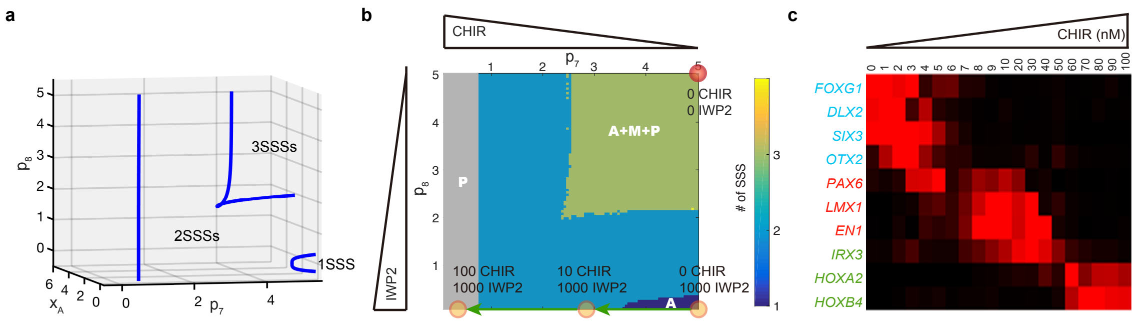

Fig. 33. Modeling and experiment results on modulation of WNT signaling specified NPCs. (**a**). 2-D bifurcation diagram with respect to the interaction parameters p_7, p_8 and state x_A, where blue lines denote boundaries among 3 SSSs, 2 SSSs and 1 SSS. (**b**). Phase diagram of p_7 and p_8. Orange circles denote system state, and green arrowhead lines represent transitions from one state to another. (**c**). Experiment data of gene expression in A/P-related gene markers in the presence of 1,000 nM IWP2 and various concentration of CHIR. For each gene, expressions were normalized with respect to the highest expression value. Data are based on experiment results in a separate work.

forebrain markers expression level is high with low concentration of CHIR (0.0 to 0.05), midbrain markers exhibit high expression level in low-medium concentration of CHIR (mainly in the range of 0.05 to 0.3), and for hindbrain markers, they start expression at around 0.20 concentration of CHIR and reach maximum after 0.60 CHIR. The experiment dose response curves produce two findings: (1) all the markers are valid and represent dynamics of the WNT signaling pathway control, (2) it is possible to use the dose response curves of seed genes to classify other genes. Based on these ideas, later, we perform standard clustering and classification on the RNA-seq data.

First we filter the genes by a list of 1459 transcription factors [196], after which we obtain 1276 genes. Then we use *kmeans* method to cluster filtered genes and choose the number of clusters as 10 which are inferred from the Gap statistic [197, 198]. The clustering result is visualized in Fig. 34(b) based on t-SNE method. To validate the clustering results, we look back to the groups of seed genes, and see whether seed genes in a same group are clustered correctly. The results are summarized in the second column of Table 8. The table suggests an efficient application of the clustering. Specifically, G1, which represents anterior related genes, likely belongs to Cluster 9; G2, which denotes posterior related genes, is most concentrated in Cluster 6; and G3, which consists of genes related to posterior, is represented by Cluster 8. Considering that currently we do not have any replicates in this experiment data, the clustering approach inevitably bears with some inaccuracy. But most seed genes in a same group are clustered together, which indicates that, if we want to find more genes for each group, we can relate to the clustering results.

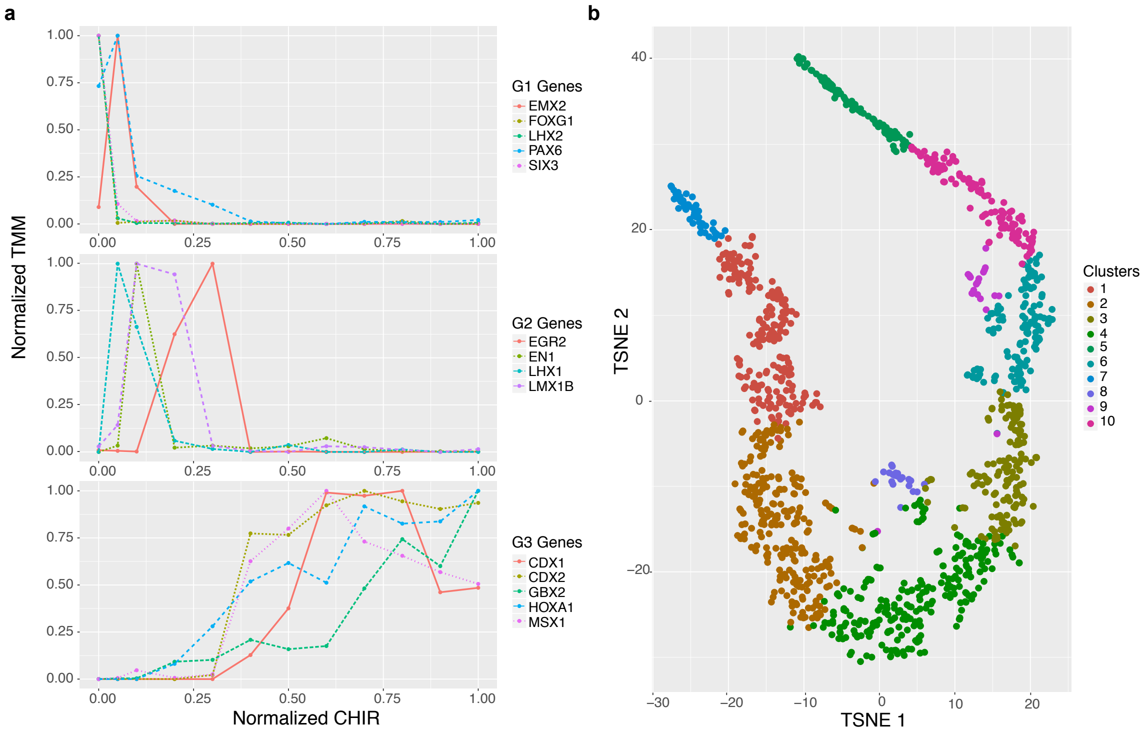

Fig. 34. Dose response of seed genes and clustering results. (**a**). Normalized Trimmed Mean of M-values (TMM) [199] expression under different doses of CHIR. (0, 0.05, 0.1, 0.2, 0.3, 0.4, 0.5, 0.6, 0.7, 0.8, 0.9 and 1.0, the concentrations were normalized with respect to the highest value). (**b**). Clustering results visualized by nonlinear dimensionality reduction method (t-SNE).

TABLE 8: Seed Genes for classifications.

Group Name	Genes and Clustering Results	Functions
G1	FOXG1 (10), PAX6 (2), SIX3 (9), EMX2 (9), LHX2 (9)	Forebrain
G2	EN1 (6), LHX1(10), LMX1B (6), EGR2 (6)	Midbrain
G3	GBX2 (8), CDX2 (8), HOXA1 (8), MSX1 (8), CDX1 (6)	Hindbrain

5.3. Conclusion

Numerous studies have shown that the WNT signaling pathway plays an important role in the differentiation process of neural progenitor cells (NPC). A gradient concentration of endogenous WNT signaling results in the heterogeneity of neurons from forebrain to midbrain, hindbrain and spinal cord. In this study, based on the WNT signaling mechanism that regulates anterior-posterior (A/P) identity, we propose a WNT controlling network model by treating the frizzled receptors, WNT target genes, anterior/posterior (A/P) markers as different modules. Then we apply Boolean based ODE modeling to characterize the dynamics within network, while network enumeration and parameter scanning methods are applied to get a high likelihood of multistability. The analysis reveals that the inhibition interactions from anterior module (“A”) to receptors (“R”) and WNT target module (“W”) and activation interaction from posterior module (“P”) to WNT target module (“W”) are key factors for maintaining multistability. Our model also correctly predicts how the multistability is controlled by the exogenous modulation of WNT signaling. Moreover, we perform clustering on RNA-seq data in related experimental study and identify TFs that may belong to anterior or posterior modules. Our results may shed light on the understanding of the role of WNT signaling mechanism in the regulation of neural progenitor cells.

REFERENCES

[1] A. Lombardi, M. Hörnquist, Controllability analysis of networks. *Phys. Rev. E* **75**, 056110 (2007).

[2] B. Liu, T. Chu, L. Wang, G. Xie, Controllability of a leader-follower dynamic network with switching topology. *IEEE Trans. Automat. Contr.* **53**, 1009-1013 (2008).

[3] A. Rahmani, M. Ji, M. Mesbahi, M. Egerstedt, Controllability of multi-agent systems from a graph-theoretic perspective. *SIAM J. Contr. Optim.* **48**, 162-186 (2009).

[4] Y.-Y. Liu, J.-J. Slotine, A.-L. Barabási, Controllability of complex networks. *Nature (London)* **473**, 167-173 (2011).

[5] W.-X. Wang, X. Ni, Y.-C. Lai, C. Grebogi, Optimizing controllability of complex networks by minimum structural perturbations. *Phys. Rev. E* **85**, 026115 (2012).

[6] J. C. Nacher, T. Akutsu, Dominating scale-free networks with variable scaling exponent: heterogeneous networks are not difficult to control. *New J. Phys.* **14**, 073005 (2012).

[7] G. Yan, J. Ren, Y.-C. Lai, C.-H. Lai, B. Li, Controlling complex networks: How much energy is needed? *Phys. Rev. Lett.* **108**, 218703 (2012).

[8] T. Nepusz, T. Vicsek, Controlling edge dynamics in complex networks. *Nat. Phys.* **8**, 568–573 (2012).

[9] Y.-Y. Liu, J.-J. Slotine, A.-L. Barabási, Observability of complex systems. *Proc. Natl. Acad. Sci. (USA)* **110**, 2460-2465 (2013).

[10] Z.-Z. Yuan, C. Zhao, Z.-R. Di, W.-X. Wang, Y.-C. Lai, Exact controllability of complex networks. *Nat. Commun.* **4**, 2447 (2013).

[11] T. Jia, *et al.*, Emergence of bimodality in controlling complex networks. *Nat. Commun.* **4**, 3002 (2013).

[12] D. Delpini, *et al.*, Evolution of controllability in interbank networks. *Sci. Rep.* **3**, 1626 (2013).

[13] J. C. Nacher, T. Akutsu, Structural controllability of unidirectional bipartite networks. *Sci. Rep.* **3**, 1647 (2013).

[14] G. Menichetti, L. Dall'Asta, G. Bianconi, Network controllability is determined by the density of low in-degree and out-degree nodes. *Phys. Rev. Lett.* **113**, 078701 (2014).

[15] J. Ruths, D. Ruths, Control profiles of complex networks. *Science* **343**, 1373–1376 (2014).

[16] S. Wuchty, Controllability in protein interaction networks. *Proc. Natl. Acad. Sci. (USA)* **111**, 7156-7160 (2014).

[17] Z.-Z. Yuan, C. Zhao, W.-X. Wang, Z.-R. Di, Y.-C. Lai, Exact controllability of multiplex networks. *New J. Phys.* **16**, 103036 (2014).

[18] F. Pasqualetti, S. Zampieri, F. Bullo, Controllability metrics, limitations and algorithms for complex networks. *IEEE Trans. Cont. Net. Syst.* **1**, 40-52 (2014).

[19] Y.-D. Xiao, S.-Y. Lao, L.-L. Hou, L. Bai, Edge orientation for optimizing controllability of complex networks. *Phys. Rev. E* **90**, 042804 (2014).

[20] F. Sorrentino, Effects of the network structural properties on its controllability. *Chaos* **17**, 033101 (2014).

[21] F.-X. Wu, L. Wu, J.-X. Wang, J. Liu, L.-N. Chen, Transittability of complex networks and its applications to regulatory biomolecular networks. *Sci. Rep.* **4**, 4819 (2014).

[22] A. J. Whalen, S. N. Brennan, T. D. Sauer, S. J. Schiff, Observability and controllability of nonlinear networks: The role of symmetry. *Phys. Rev. X* **5**, 011005 (2015).

[23] G. Yan, *et al.*, Spectrum of controlling and observing complex networks. *Nat. Phys.* **11**, 779-786 (2015).

[24] Y.-Z. Chen, L.-Z. Wang, W.-X. Wang, Y.-C. Lai, The paradox of controlling complex networks: control inputs versus energy requirement. *arXiv:1509.03196v1* (2015).

[25] J. C. Nacher, T. Akutsu, Structurally robust control of complex networks. *Phys. Rev. E* **91**, 012826 (2015).

[26] T. H. Summers, F. L. Cortesi, J. Lygeros, On submodularity and controllability in complex dynamical networks. *IEEE Trans. Cont. Net. Syst.* **3**, 91-101 (2015).

[27] Y.-Z. Chen, L.-Z. Wang, W.-X. Wang, Y.-C. Lai, Energy scaling and reduction in controlling complex networks. *Royal Soc. Open Sci.* **3**, 160064 (2016).

[28] Y.-Y. Liu, A.-L. Barabási, Control principles of complex systems. *Rev. Mod. Phys.* **88**, 035006 (2016).

[29] R. E. Kalman, Mathematical description of linear dynamical systems. *J. Soc. Indus. Appl. Math. Ser. A* **1**, 152-192 (1963).

[30] C.-T. Lin, Structural controllability. *IEEE Trans. Automat. Contr.* **19**, 201-208 (1974).

[31] J. E. Hopcroft, R. M. Karp, An nˆ5/2 algorithm for maximum matchings in bipartite graphs. *SIAM J. Comput.* **2**, 225-231 (1973).

[32] H. Zhou, Z.-C. Ou-Yang, Maximum matching on random graphs. *arXiv preprint cond-mat/0309348* (2003).

[33] L. Zdeborová, M. Mézard, The number of matchings in random graphs. *J. Stat. Mech.* **2006**, P05003 (2006).

[34] Y.-Y. Liu, J.-J. Slotine, A. L. Barabási, Control centrality and hierarchical structure in complex networks. *PLoS ONE* **7**, e44459 (2012).

[35] M. L. J. Hautus, *Ned. Akad. Wetenschappen, Proc. Ser. A* (Elsevier, 1969), vol. 72, pp. 443–448.

[36] W. J. Rugh, *Linear Systems Theory* (Prentice-Hall, Inc., 1996).

[37] C. T. Chen, *Linear Systems Theory and Design* (Oxford University Press, Inc., 1984), first edn.

[38] P. Erdős, A. Rényi, On random graphs, i. *Publ. Math.* **6**, 290-297 (1959).

[39] R. Albert, A.-L. Barabási, Statistical mechanics of complex networks. *Rev. Mod. Phys* **74**, 47-97 (2002).

[40] G. Strang, *Linear Algebra and Its Applications* (Academic Press, 1976).

[41] F. Sorrentino, M. di Bernardo, F. Garofalo, G. Chen, Controllability of complex networks via pinning. *Phys. Rev. E* **75**, 046103 (2007).

[42] B. Fiedler, A. Mochizuki, G. Kurosawa, D. Saito, Dynamics and control at feedback vertex sets. i: Informative and determining nodes in regulatory networks. *J. Dyn. Differ. Eqns.* **25**, 563-604 (2013).

[43] A. Mochizuki, B. Fiedler, G. Kurosawa, D. Saito, Dynamics and control at feedback vertex sets. ii: A faithful monitor to determine the diversity of molecular activities in regulatory networks. *J. Theor. Biol.* **335**, 130-146 (2013).

[44] Y.-C. Lai, Controlling complex, nonlinear dynamical networks. *Nat. Sci. Rev.* **1**, 339-341 (2014).

[45] L.-Z. Wang, *et al.*, A geometrical approach to control and controllability of nonlinear dynamical networks. *Nat. Commun.* **7**, 11323 (2016).

[46] J. G. T. Zanudo, G. Yang, R. Albert, Structure-based control of complex networks with nonlinear dynamics. *arXiv:1605.08415* (2016).

[47] W.-X. Wang, X. Ni, Y.-C. Lai, C. Grebogi, Optimizing controllability of complex networks by small structural perturbations. *Phys. Rev. E* **85**, 026115 (2011).

[48] J.-J. E. Slotine, W. Li, *Applied Nonlinear Control*, vol. 199 (Prentice-Hall Englewood Cliffs, NJ, 1991).

[49] U. Feudel, C. Grebogi, Why are chaotic attractors rare in multistable systems? *Phys. Rev. Lett.* **91**, 134102 (2003).

[50] Y.-C. Lai, T. Tél, *Transient Chaos - Complex Dynamics on Finite-Time Scales* (Springer, New York, 2011), first edn.

[51] S. Huang, Genetic and non-genetic instability in tumor progression: link between the fitness landscape and the epigenetic landscape of cancer cells. *Cancer Metastasis Rev.* **32**, 423–448 (2013).

[52] G. M. Süel, J. Garcia-Ojalvo, L. M. Liberman, M. B. Elowitz, An excitable gene regulatory circuit induces transient cellular differentiation. *Nature* **440**, 545–550 (2006).

[53] S. Huang, G. Eichler, Y. Bar-Yam, D. E. Ingber, Cell fates as high-dimensional attractor states of a complex gene regulatory network. *Phys. Rev. Lett.* **94**, 128701 (2005).

[54] C. Furusawa, K. Kaneko, A dynamical-systems view of stem cell biology. *Science* **338**, 215-217 (2012).

[55] X. Li, K. Zhang, J. Wang, Exploring the mechanisms of differentiation, dedifferentiation, reprogramming and transdifferentiation. *PloS one* **9**, e105216 (2014).

[56] G. Yao, C. Tan, M. West, J. Nevins, L. You, Origin of bistability underlying mammalian cell cycle entry. *Mol. Syst. Biol.* **7** (2011).

[57] D. Battogtokh, J. J. Tyson, Bifurcation analysis of a model of the budding yeast cell cycle. *Chaos* **14**, 653–661 (2004).

[58] S. Kauffman, C. Peterson, B. Samuelsson, C. Troein, Genetic networks with canalyzing boolean rules are always stable. *Proc. Natl. Acad. Sci. (USA)* **101**, 17102-17107 (2004).

[59] F. Greil, B. Drossel, Dynamics of critical kauffman networks under asynchronous stochastic update. *Phys. Rev. Lett.* **95**, 048701 (2005).

[60] A. Motter, N. Gulbahce, E. Almaas, A.-L. Barabási, Predicting synthetic rescues in metabolic networks. *Mol. Sys. Biol.* **4** (2008).

[61] W. Ma, A. Trusina, H. El-Samad, W. A. Lim, C. Tang, Defining network topologies that can achieve biochemical adaptation. *Cell* **138**, 760-773 (2009).

[62] P. C. Faucon, *et al.*, Gene networks of fully connected triads with complete auto-activation enable multistability and stepwise stochastic transitions. *PloS one* **9**, e102873 (2014).

[63] T. S. Gardner, C. R. Cantor, J. J. Collins, Construction of a genetic toggle switch in escherichia coli. *Nature* **403**, 339–342 (2000).

[64] M. Wu, *et al.*, Engineering of regulated stochastic cell fate determination. *Proc. Natl. Acad. Sci. (USA)* **110**, 10610-10615 (2013).

[65] J. D. Feala, *et al.*, Systems approaches and algorithms for discovery of combinatorial therapies. *Wiley Interdiscip. Rev. Syst. Biol. Med.* **2**, 181–193 (2010).

[66] J. B. Fitzgerald, B. Schoeberl, U. B. Nielsen, P. K. Sorger, Systems biology and combination therapy in the quest for clinical efficacy. *Nat. Chem. Biol.* **2**, 458–466 (2006).

[67] T. Ellis, X. Wang, J. J. Collins, Diversity-based, model-guided construction of synthetic gene networks with predicted functions. *Nat. Biotechno* **27**, 465-471 (2009).

[68] R. Zhang, *et al.*, Network model of survival signaling in large granular lymphocyte leukemia. *Proc. Natl. Acad. Sci. (USA)* **105**, 16308-16313 (2008).

[69] A. Saadatpour, *et al.*, Dynamical and structural analysis of a t cell survival network identifies novel candidate therapeutic targets for large granular lymphocyte leukemia. *PloS Comp. Biol.* **7**, e1002267 (2011).

[70] D. M. Wittmann, *et al.*, Transforming boolean models to continuous models: methodology and application to t-cell receptor signaling. *BMC Syst. Biol.* **3**, 98 (2009).

[71] J. Krumsiek, S. Pölsterl, D. M. Wittmann, F. J. Theis, Odefy-from discrete to continuous models. *BMC Bioinformatcis* **11**, 233 (2010).

[72] S. P. Cornelius, W. L. Kath, A. E. Motter, Realistic control of network dynamics. *Nat. Comm.* **4**, 1942 (2013).

[73] R. Benzi, A. Sutera, A. Vulpiani, The mechanism of stochastic resonance. *J. Phys. A* **14**, L453-L457 (1981).

[74] P. C. Gailey, A. Neiman, J. J. Collins, F. Moss, Stochastic resonance in ensembles of nondynamical elements: The role of internal noise. *Phys. Rev. Lett.* **79**, 4701-4704 (1997).

[75] A. S. Pikovsky, J. Kurths, Coherence resonance in a noise-driven excitable system. *Phys. Rev. Lett.* **78**, 775-778 (1997).

[76] Z. Liu, Y.-C. Lai, Coherence resonance in coupled chaotic oscillators. *Phys. Rev. Lett.* **86**, 4737-4740 (2001).

[77] D. K. Wells, W. L. Kath, A. E. Motter, Control of stochastic and induced switching in biophysical networks. *Phys. Rev. X* **5**, 031036 (2015).

[78] E. Ott, C. Grebogi, J. A. Yorke, Controlling chaos. *Phys. Rev. Lett.* **64**, 1196-1199 (1990).

[79] S. Boccaletti, C. Grebogi, Y.-C. Lai, H. Mancini, D. Maza, Control of chaos: theory and applications. *Phys. Rep.* **329**, 103-197 (2000).

[80] C. Grebogi, Y.-C. Lai, Controlling chaotic dynamical systems. *Syst. Control Lett.* **31**, 307-312 (1997).

[81] X. Li, X. F. Wang, G. Chen, Pinning a complex dynamical network to its equilibrium. *IEEE Trans. Circ. Syst. I* **51**, 2074-2087 (2004).

[82] E. Ott, *Chaos in Dynamical Systems* (Cambridge University Press, 2002), second edn.

[83] P. J. Menck, J. Heitzig, J. Kurths, H. J. Schellnhuber, How dead ends undermine power grid stability. *Nat. Comm.* **5**, 3969 (2014).

[84] C. Campbell, R. Albert, Stabilization of perturbed boolean network attractors through compensatory interactions. *BMC Syst. Biol.* **8**, 53 (2014).

[85] P. Wang, *et al.*, Epigenetic state network approach for describing cell phenotypic transitions. *Interface Focus* **4**, 20130068 (2014).

[86] A. Dhooge, W. Govaerts, Y. A. Kuznetsov, Matcont: a matlab package for numerical bifurcation analysis of odes. *ACM Transactions on Mathematical Software (TOMS)* **29**, 141–164 (2003).

[87] S. Huang, Y.-P. Guo, G. May, T. Enver, Bifurcation dynamics in lineage-commitment in bipotent progenitor cells. *Developmental Biol.* **305**, 695-713 (2007).

[88] N. Yin, *et al.*, Synergistic and antagonistic drug combinations depend on network topology. *PloS one* **9**, e93960 (2014).

[89] J. Wang, K. Zhang, L. Xu, E. Wang, Quantifying the waddington landscape and biological paths for development and differentiation. *Proc. Natl. Acad. Sci. (USA)* **108**, 8257–8262 (2011).

[90] S. Bhattacharya, Q. Zhang, M. E. Andersen, A deterministic map of waddington's epigenetic landscape for cell fate specification. *BMC Syst. Biol.* **5**, 85 (2011).

[91] J. A. Kromer, L. Schimansky-Geier, R. Toral, Weighted-ensemble brownian dynamics simulation: Sampling of rare events in nonequilibrium systems. *Phys. Rev. E* **87**, 063311 (2013).

[92] C. H. Waddington, *The Strategy of the Genes* (Allen & Unwin, London, 1957).

[93] B. D. MacArthur, A. Maayan, I. R. Lemischka, Systems biology of stem cell fate and cellular reprogramming. *Nat. Rev. Mol. Cell Biol.* **10**, 672-681 (2009).

[94] F. Corson, E. D. Siggia, Geometry, epistasis, and developmental patterning. *Proc. Nat. Acad. Sci. (USA)* **109**, 5568-5575 (2012).

[95] B. McNamara, K. Wiesenfeld, Theory of stochastic resonance. *Phys. Rev. A* **39**, 4854-4869 (1989).

[96] L. Gammaitoni, P. Hänggi, P. Jung, F. Marchesoni, Stochastic resonance. *Rev. Mod. Phys.* **70**, 223-287 (1998).

[97] J. Wang, L. Xu, E. K. Wang, Potential landscape and flux framework of nonequilibrium networks: Robustness, dissipation, and coherence of biochemical oscillations. *Proc. Natl. Acad. Sci. USA* **105**, 12271-12276 (2008).

[98] F. Zhang, L. Xu, K. Zhang, E. K. Wang, J. Wang, The potential and flux landscape theory of evolution. *J. Chem. Phys.* **137**, 065102 (2012).

[99] R. Garham, T. Tél, Existence of a potential for dissipative dynamical systems. *Phys. Rev. Lett.* **52**, 9-12 (1984).

[100] R. Graham, A. Hamm, T. Tél, Nonequilibrium potentials for dynamical systems with fractal attractors and repellers. *Phys. Rev. Lett.* **66**, 3089-3092 (1991).

[101] T. Tél, Y.-C. Lai, Quasipotential approach to critical scaling in noise-induced chaos. *Phys. Rev. E* **81**, 056208 (2010).

[102] J. Shu, *et al.*, Induction of pluripotency in mouse somatic cells with lineage specifiers. *Cell* **153**, 963-975 (2013).

[103] M. I. Freidlin, J. Szücs, A. D. Wentzell, *Random perturbations of dynamical systems*, vol. 260 (Springer Science & Business Media, 2012).

[104] J. Xing, K. S. Kim, Application of the projection operator formalism to non-hamiltonian dynamics. *J. Chem. Phys.* **134**, 044132 (2011).

[105] M. G. Rose, N. Berliner, T-cell large granular lymphocyte leukemia and related disorders. *The Oncologist* **9**, 247–258 (2004).

[106] D. P. OMalley, T-cell large granular leukemia and related proliferations. *American journal of clinical pathology* **127**, 850–859 (2007).

[107] D. T. Gillespie, Exact stochastic simulation of coupled chemical reactions. *J. Phys. Chem.* **81**, 2340-2361 (1970).

[108] K. A. D'Amour, *et al.*, Production of pancreatic hormone–expressing endocrine cells from human embryonic stem cells. *Nat. Biotechnol* **24**, 1392-1401 (2006).

[109] E. Kroon, *et al.*, Pancreatic endoderm derived from human embryonic stem cells generates glucose-responsive insulin-secreting cells in vivo. *Nat. Biotechnol* **26**, 443-452 (2008).

[110] I. Bozic, *et al.*, Evolutionary dynamics of cancer in response to targeted combination therapy. *eLife* **2**, e00747 (2013).

[111] D. Lazer, *et al.*, Life in the network: the coming age of computational social science. *Science* **323**, 721-723 (2009).

[112] P. Holme, M. E. J. Newman, Nonequilibrium phase transition in the coevolution of networks and opinions. *Phys. Rev. E* **74**, 056108 (2006).

[113] H. Kwak, C.-H. Lee, H. Park, S. Moon, *Proceedings of the 19th international conference on World wide web* (ACM, 2010), pp. 591–600.

[114] D. M. Romero, B. Meeder, J. Kleinberg, *Proceedings of the 20th international conference on World wide web* (ACM, 2011), pp. 695–704.

[115] S. Goel, D. J. Watts, D. G. Goldstein, *Proceedings of the 13th ACM Conference on Electronic Commerce* (ACM, 2012), pp. 623–638.

[116] M.-Y. Cha, H. Haddadi, F. Benevenuto, K. Gummadi, P. Krishna, *4th international AAAI conference on weblogs and social media (ICWSM)* (2010), vol. 14, p. 8.

[117] J. Borondo, A. J. Morales, J. C. Losada, R. M. Benito, Characterizing and modeling an electoral campaign in the context of twitter: 2011 spanish presidential election as a case study. *Chaos* **22**, 023138 (2012).

[118] J. Stehlé, A. Barrat, G. Bianconi, Dynamical and bursty interactions in social networks. *Phys. Rev. E* **81**, 035101 (2010).

[119] B. Gonçalves, N. Perra, A. Vespignani, Modeling users' activity on Twitter networks: Validation of dunbar's number. *PloS One* **6**, e22656 (2011).

[120] Q. Gao, F. Abel, G.-J. Houben, Y. Yu, *User Modeling, Adaptation, and Personalization* (Springer, 2012), pp. 88–101.

[121] L. Yu, S. Asur, B. A. Huberman, What trends in chinese social media. *arXiv:1107.3522* (2011).

[122] M. Oka, T. Ikegami, Exploring default mode and information flow on the web. *PloS One* **8**, e60398 (2013).

[123] L. Lü, Y.-C. Zhang, C. H. Yeung, T. Zhou, Leaders in social networks, the delicious case. *PloS One* **6**, e21202 (2011).

[124] D. Mocanu, *et al.*, The twitter of babel: Mapping world languages through microblogging platforms. *PloS One* **8**, e61981 (2013).

[125] D. Boyd, S. Golder, G. Lotan, *System Sciences (HICSS), 2010 43rd Hawaii International Conference on* (IEEE, 2010), pp. 1–10.

[126] Wikipedia, 2011 tōhoku earthquake and tsunami, `http://en.wikipedia.org/wiki/2011Tohokuearthquakeandtsunami` (2011).

[127] L. Burkit, Y. Zhang, S. Oster, Fearing radiation, chinese rush to buy table salt? *Wall St. J.* (2011).

[128] A. Clauset, C. R. Shalizi, M. E. J. Newman, Power-law distributions in empirical data. *SIAM Rev.* **51**, 661-703 (2009).

[129] J. G. Foster, D. V. Foster, P. Grassberger, M. Paczuski, Edge direction and the structure of networks. *Proc. Natl. Acad. Sci. (USA)* **107**, 10815-10820 (2010).

[130] M. Kitsak, *et al.*, Identification of influential spreaders in complex networks. *Nat. Phys.* **6**, 888-893 (2010).

[131] P. Singh, S. Sreenivasan, B. K. Szymanski, G. Korniss, Threshold-limited spreading in social networks with multiple initiators. *Sci. Rep.* **3** (2013).

[132] J.-P. Onnela, F. Reed-Tsochas, Spontaneous emergence of social influence in online systems. *Proc. Natl. Acad. Sci. (USA)* **107**, 18375-18380 (2010).

[133] J. Yang, J. Leskovec, *Proceedings of the fourth ACM international conference on Web search and data mining* (ACM, 2011), pp. 177–186.

[134] L. Weng, A. Flammini, A. Vespignani, F. Menczer, Competition among memes in a world with limited attention. *Sci. Rep.* **2**, 335 (2012).

[135] Z.-D. Zhao, *et al.*, Emergence of scaling in human-interest dynamics. *Sci. Rep.* **3**, 3472 (2013).

[136] L.-Z. Wang, Z.-G. Huang, Z.-H. Rong, X.-F. Wang, Y.-C. Lai, Emergence, evolution and scaling of online social networks. *PloS One* **9** (2014).

[137] J. P. Gleeson, J. A. Ward, K. P. OSullivan, W. T. Lee, Competition-induced criticality in a model of meme popularity. *Phys. Rev. Lett.* **112**, 048701 (2014).

[138] Y.-R. Lin, B. Keegan, D. Margolin, D. Lazer, Rising tides or rising stars?: Dynamics of shared attention on Twitter during media events. *PLoS One* **9**, e94093 (2014).

[139] J. P. Gleeson, D. Cellai, J.-P. Onnela, M. A. Porter, F. Reed-Tsochas, A simple generative model of collective online behavior. *Proc. Natl. Acad. Sci* **111**, 10411–10415 (2014).

[140] K.-K. Kleineberg, M. Boguñá, Digital ecology: coexistence and domination among interacting networks. *Sci. Rep.* **5** (2015).

[141] J. P. Gleeson, K. P. OSullivan, R. A. Baños, Y. Moreno, Effects of network structure, competition and memory time on social spreading phenomena. *Phys. Rev. X* **6**, 021019 (2016).

[142] Z.-K. Zhang, *et al.*, Dynamics of information diffusion and its applications on complex networks. *Phys. Rep.* **651**, 1-34 (2016).

[143] C.-J. Wang, L. Wu, J. Zhang, M. A. Janssen, The collective direction of attention diffusion. *Sci. Rep.* **6** (2016).

[144] X. Qiu, D. F. Oliveira, A. S. Shirazi, A. Flammini, F. Menczer, Limited individual attention and online virality of low-quality information. *Nat. Human Behav.* **1**, 0132 (2017).

[145] S. Luo, F. Morone, C. Sarraute, M. Travizano, H. A. Makse, Inferring personal economic status from social network location. *Nat. Commun.* **8** (2017).

[146] K.-K. Kleineberg, M. Boguná, Evolution of the digital society reveals balance between viral and mass media influence. *Phys. Rev. X* **4**, 031046 (2014).

[147] T. Zaman, E. B. Fox, E. T. Bradlow, *et al.*, A Bayesian approach for predicting the popularity of tweets. *Ann. Appl. Stat.* **8**, 1583–1611 (2014).

[148] A. G. Hawkes, Spectra of some self-exciting and mutually exciting point processes. *Biometrika* **58**, 83–90 (1971).

[149] Q. Zhao, M. A. Erdogdu, H. Y. He, A. Rajaraman, J. Leskovec, *Proceedings of the 21th ACM SIGKDD International Conference on Knowledge Discovery and Data Mining* (ACM, 2015), pp. 1513–1522.

[150] H. von Foerster, Some remarks on changing populations. *Kinet. Cellu. Prolif.* pp. 382–407 (1959).

[151] E. Trucco, Mathematical models for cellular systems the von Foerster equation. part i. *Bull. Math. Biol.* **27**, 285–304 (1965).

[152] E. Trucco, Mathematical models for cellular systems. the von Foerster equation. part ii. *Bull. Math. Biol.* **27**, 449–471 (1965).

[153] T. Lu, D. Volfson, L. Tsimring, J. Hasty, Cellular growth and division in the Gillespie algorithm. *Sys. Biol.* **1**, 121–128 (2004).

[154] Z. Kutalik, M. Razaz, J. Baranyi, Connection between stochastic and deterministic modelling of microbial growth. *J. Theo. Biol.* **232**, 285–299 (2005).

[155] P. Wang, *et al.*, Robust growth of Escherichia coli. *Curr. Biol.* **20**, 1099–1103 (2010).

[156] J. Horowitz, M. D. Normand, M. G. Corradini, M. Peleg, Probabilistic model of microbial cell growth, division, and mortality. *Appl. Envir. Microbiol.* **76**, 230–242 (2010).

[157] E. B. Stukalin, I. Aifuwa, J. S. Kim, D. Wirtz, S. X. Sun, Age-dependent stochastic models for understanding population fluctuations in continuously cultured cells. *J. Roy. Soc. Interface* **10**, 20130325 (2013).

[158] B. Ribeiro, *Proceedings of the 23rd International Conference on World Wide Web* (ACM, 2014), pp. 653–664.

[159] D. Antunes, A. Singh, Quantifying gene expression variability arising from randomness in cell division times. *J. Math. Biol.* **71**, 437–463 (2015).

[160] C. D. Greenman, T. Chou, Kinetic theory of age-structured stochastic birth-death processes. *Phys. Rev. E* **93**, 012112 (2016).

[161] T. Chou, C. D. Greenman, A hierarchical kinetic theory of birth, death and fission in age-structured interacting populations. *J. Stat. Phys.* **164**, 49–76 (2016).

[162] S. Widder, *et al.*, Challenges in microbial ecology: building predictive understanding of community function and dynamics. *ISME J.* **10**, 2557 (2016).

[163] A.-L. Barabási, The origin of bursts and heavy tails in human dynamics. *Nature* **435**, 207–211 (2005).

[164] J. G. Oliveira, A.-L. Barabási, Human dynamics: Darwin and Einstein correspondence patterns. *Nature* **437**, 1251–1251 (2005).

[165] Z. Dezsö, *et al.*, Dynamics of information access on the web. *Phys. Rev. E* **73**, 066132 (2006).

[166] T. Zhou, H. A.-T. Kiet, B. J. Kim, B.-H. Wang, P. Holme, Role of activity in human dynamics. *EPL (Europhys. Lett.)* **82**, 28002 (2008).

[167] B. Gonçalves, J. J. Ramasco, Human dynamics revealed through Web analytics. *Phys. Rev. E* **78**, 026123 (2008).

[168] C. Song, T. Koren, P. Wang, A.-L. Barabási, Modeling the scaling properties of human mobility. *Nat. Phys.* **6**, 818-823 (2010).

[169] M. Szell, R. Sinatra, G. Petri, S. Thurner, V. Latora, Understanding mobility in a social petri dish. *Sci. Rep.* **2** (2012).

[170] F. Wu, B. A. Huberman, Novelty and collective attention. *Proc. Natl. Acad. Sci. (USA)* **104**, 17599–17601 (2007).

[171] M. Ye, T. Sandholm, C. Wang, C. Aperjis, B. A. Huberman, *Proc. 21st Int. Conf. WWW* (ACM, 2012), pp. 1205–1212.

[172] S. Brin, L. Page, The anatomy of a large-scale hypertextual Web search engine. *Comp. Net. ISDN* **30**, 107–117 (1998).

[173] N. Craswell, M. Szummer, *Proc. 30th Annual Int. ACM SIGIR CRDIR* (ACM, 2007), pp. 239–246.

[174] R. Fagin, *et al.*, Random walks with "back buttons". *Ann. Appl. Prob.* pp. 810–862 (2001).

[175] M. R. Meiss, B. Gonçalves, J. J. Ramasco, A. Flammini, F. Menczer, *Proc. 21st ACM CHH* (ACM, 2010), pp. 229–234.

[176] F. Chierichetti, R. Kumar, P. Raghavan, T. Sarlós, *Proc. 21st Int. Conf. WWW* (ACM, 2012), pp. 609–618.

[177] L. Tang, X. Wang, H. Liu, Community detection via heterogeneous interaction analysis. *Data Min. Knowl. Disc.* **25**, 1-33 (2012).

[178] T. Kuhn, M. Perc, D. Helbing, Inheritance patterns in citation networks reveal scientific memes. *Phys. Rev. X* **4**, 041036 (2014).

[179] S. Boccaletti, *et al.*, The structure and dynamics of multilayer networks. *Phys. Rep.* **544**, 1–122 (2014).

[180] C. Sanlı, R. Lambiotte, Local variation of hashtag spike trains and popularity in Twitter. *PloS One* **10**, e0131704 (2015).

[181] H. Zhu, X. Yin, J. Ma, W. Hu, Identifying the main paths of information diffusion in online social networks. *Physica A* **452**, 320–328 (2016).

[182] R. Wetzker, C. Zimmermann, C. Bauckhage, *Proceedings of the ECAI 2008 Mining Social Data Workshop* (2008), pp. 26–30.

[183] Wikipedia, Sina weibo, `https://en.wikipedia.org/wiki/Sina_Weibo` (2015).

[184] M. Ikeya, S. M. Lee, J. E. Johnson, A. P. McMahon, S. Takada, Wnt signalling required for expansion of neural crest and cns progenitors. *Nature* **389**, 966 (1997).

[185] Y. Hirabayashi, *et al.*, The wnt/β-catenin pathway directs neuronal differentiation of cortical neural precursor cells. *Development* **131**, 2791–2801 (2004).

[186] D. D. O'Leary, S.-J. Chou, S. Sahara, Area patterning of the mammalian cortex. *Neuron* **56**, 252–269 (2007).

[187] A. Chenn, Wnt/β-catenin signaling in cerebral cortical development. *Organogenesis* **4**, 76–80 (2008).

[188] K. C. Davidson, *et al.*, Wnt/β-catenin signaling promotes differentiation, not self-renewal, of human embryonic stem cells and is repressed by oct4. *Proceedings of the National Academy of Sciences* **109**, 4485–4490 (2012).

[189] N. Moya, J. Cutts, T. Gaasterland, K. Willert, D. A. Brafman, Endogenous wnt signaling regulates hpsc-derived neural progenitor cell heterogeneity and specifies their regional identity. *Stem cell reports* **3**, 1015–1028 (2014).

[190] N. Bengoa-Vergniory, R. M. Kypta, Canonical and noncanonical wnt signaling in neural stem/progenitor cells. *Cellular and Molecular Life Sciences* **72**, 4157–4172 (2015).

[191] Z. Yao, *et al.*, A single-cell roadmap of lineage bifurcation in human esc models of embryonic brain development. *Cell stem cell* **20**, 120–134 (2017).

[192] C. Kiecker, C. Niehrs, A morphogen gradient of wnt/β-catenin signalling regulates anteroposterior neural patterning in xenopus. *Development* **128**, 4189–4201 (2001).

[193] L. Ciani, P. C. Salinas, Wnts in the vertebrate nervous system: from patterning to neuronal connectivity. *Nature reviews. Neuroscience* **6**, 351 (2005).

[194] J.-P. Saint-Jeannet, Patterning the vertebrate neural plate by wnt signaling (2013).

[195] D. Brafman, K. Willert, Wnt/β-catenin signaling during early vertebrate neural development. *Developmental Neurobiology* (2017).

[196] L. A. Furchtgott, S. Melton, V. Menon, S. Ramanathan, Discovering sparse transcription factor codes for cell states and state transitions during development. *eLife* **6**, e20488 (2017).

[197] J. A. Hartigan, M. A. Wong, Algorithm as 136: A k-means clustering algorithm. *Journal of the Royal Statistical Society. Series C (Applied Statistics)* **28**, 100–108 (1979).

[198] R. Tibshirani, G. Walther, T. Hastie, Estimating the number of clusters in a data set via the gap statistic. *Journal of the Royal Statistical Society: Series B (Statistical Methodology)* **63**, 411–423 (2001).

[199] M. D. Robinson, A. Oshlack, A scaling normalization method for differential expression analysis of rna-seq data. *Genome biology* **11**, R25 (2010).

APPENDIX A

ACHIEVEMENTS DURING PHD STUDIES

Following are the relevant publications on the topics presented in this dissertation

1. **L.-Z. Wang**, Z.-G. Huang, Z.-H. Rong, X.-F. Wang, and Y.-C. Lai, "Emergence, evolution and scaling of online social networks," *PloS One*, **9**, e111013 (2014).
2. **L.-Z. Wang**, F. Wu, K. Flores, Y.-C. Lai, and X. Wang, "Build to understand: synthetic approaches to biology," *Integrative Biology*, **8**, 394 (2016).
3. **L.-Z. Wang**, R.-Q. Su, Z.-G. Huang, X. Wang, W.-X. Wang, C. Grebogi, and Y.-C. Lai, "A geometrical approach to control and controllability of nonlinear dynamical networks," *Nature Communications*, **7**, 11323 (2016).
4. Y.-Z. Chen, **L.-Z. Wang**, W.-X. Wang, and Y.-C. Lai, "Energy scaling and reduction in controlling complex networks," *Royal Society Open Science*, **3**, 160064 (2016).
5. **L.-Z. Wang**, Y.-Z. Chen, W.-X. Wang and Y.-C. Lai, "Physical controllability of complex networks," *Scientific Reports*, **7**, 40198 (2017).